BILINGUAL PUBLISHING GROUP

Volume 5 · Issue 2 · April 2023 ISSN 2810-9384(Online)

Advances in Geological and Geotechnical Engineering Research

Volume 5 Issue 2 • April 2023 • ISSN 2810-9384 (Online)

Advances in Geological and Geotechnical Engineering Research

BILINGUAL PUBLISHING GROUP

BILINGUAL PUBLISHING GROUP

Volume 5 | Issue 2 | April 2023 | Page1-78

Advances in Geological and Geotechnical Engineering Research

Contents

Editorial

Articles

BILINGUAL PUBLISHING GROUP

Advances in Geological and Geotechnical Engineering Research

https://journals.bilpubgroup.com/index.php/agger

ARTICLE

Application of 2-D and 3-D Geo-electrical Resistivity Tomography and Geotechnical Soil Evaluation for Engineering Site Investigation: A Case Study of Okerenkoko Primary School, Warri-Southwest, Delta State, Nigeria

***U. Stanley Eze*[1*], *M. Edirin Okiotor*[2], *J. E. Ighodalo*[3], *B. Jennifer Owonaro*[2], *A. Saleh Saleh*[4], *A. Sikiru Jamiu*[2]**

[1] *Department of Earth Sciences, Federal University of Petroleum Resources, Effurun, 330102, Nigeria*

[2] *Department of Marine Geology, Nigeria Maritime University, Okerenkoko, Warri South, Delta State, 332105, Nigeria*

[3] *Department of Physics (Applied Geophysics program), University of Benin, Benin City, Edo State, 300213, Nigeria*

[4] *Department of Petroleum Engineering and Geosciences, Petroleum Training Institute, Effurun, 330102, Nigeria*

ABSTRACT

In the design of building structures, joint efforts must be decided to resolve the depth of competent layers across the intended site to safeguard the durability of civil engineering structures and to avert the disastrous consequences of structural failure and collapse. In this study, an integrated methodology that employed DC resistivity tomography involving 2-D and 3-D techniques and geotechnical-soil analysis was used to evaluate subsoil conditions for engineering site investigation at Okerenkoko primary school, in the Warri-southwest area of Delta State, to adduce the phenomena responsible for the visible cracks/structural failure observed in the buildings. The results obtained brought to light the geological structure beneath the subsurface, which consists of four geoelectric layers identified as topsoil, dry/lithified upper sandy layer, wet sand (water-saturated) and peat/clay/sandy clayey soil (highly water-saturated). The deeply-seated peat/clay materials ($\rho \leq 20$ Ωm) were delineated in the study area to the depths of 17.1 m and 19.8 m from 2-D and 3-D tomography respectively. 3-D images presented as horizontal depth slices revealed the dominance of very low resistivity materials i.e. peat/clay/sandy clay within the fourth, fifth and sixth layers at depths ranging from 8.68-12.5 m, 12.5-16.9 m and 16.9-21.9 m respectively. The dominance of mechanically unstable peat/clay/sandy clay layers beneath the subsurface, which are highly mobile in response to volumetric changes, is responsible for the noticeable cracks/failure detected on structures within the study site. These observations were validated by a geotechnical test of soil samples in the study area. Atterberg's limits of the samples revealed plasticity indices of zero. Thus, the soil samples within the depth analyzed were representatives of sandy soil that does not possess any plasticity. The methods justifiably provided relevant information on the subsurface geology beneath the study site and should be appropriated as major tools for engineering site assessment/geotechnical projects.

Keywords: 2D and 3D resistivity tomography; Engineering site/structure; Atterberg limits; Orthogonal lines; Radar sounding

*CORRESPONDING AUTHOR:

U. Stanley Eze, Department of Earth Sciences, Federal University of Petroleum Resources, Effurun, 330102, Nigeria; Email: uchechukwueze2014@gmail.com

ARTICLE INFO

Received: 3 January 2023 | Revised: 4 March 2023 | Accepted: 7 March 2023 | Published Online: 22 March 2023

DOI: https://doi.org/10.30564/agger.v5i2.5382

CITATION

Eze, S.U., Okiotor, M.E., J. E. Ighodalo, J.E., et al., 2023. Application of 2-D and 3-D Geo-electrical Resistivity Tomography and Geotechnical Soil Evaluation for Engineering Site Investigation: A Case Study of Okerenkoko Primary School, Warri-Southwest, Delta State, Nigeria. Advances in Geological and Geotechnical Engineering Research. 5(2): 1-23. DOI: https://doi.org/10.30564/agger.v5i2.5382

1. Introduction

An ample evaluation of geologic and geotechnical subsurface conditions in an intended engineering site is critical for the secure design of building structures, to avert the disastrous consequences of structural failure and collapse prevalent of late. In subsoil evaluation, joint efforts must be decided to resolve the depth to competent layers across the intended site, to safeguard the durability of civil engineering structures i.e. buildings, bridges, roads and other infrastructures [1,2]. On the 1st of November 2021, it was reported that a 21-storey building on Gerard Road, Ikoyi, Lagos State collapsed killing many people, due to lack of quality assurance/control, poor management of the project and negligence by agencies responsible for approval and supervision of the building project [3]. Premium Times report [3], also stated that the building's density and impediment on the site displayed gross negligence of the Lagos State building moderations.

Over 50 percent of all building/structural failures in developing countries like Nigeria can be allied to geologic and geotechnical problems, in accordance with the information provided by Chendo and Obi [4]. The geologic and geotechnical problems cover a wide spectrum from foundation defects caused by poor investigation of the nature/type of soils in the area to the subsurface geology. Areas such as coastal environments, swamp belts and flood plains might have experienced differential sedimentation of diverse organic matters and sediments. These domains are inherently overflowing due to the existence of impermeable soil layer-mostly clay, resulting in the habitation of mechanically unstable peat material (moderately decomposed organic substance) may be imminent [5] as cited in Ayolabi et al. [6].

In evaluating subsoil conditions in an engineering site, the electrical resistivity method, plays a decisive role in the detection of subsoil properties for engineering site probing. Two-dimensional (2-D) geoelectrical resistivity tomography (ERT) is a familiar geophysical imaging technique extensively utilized in environmental and civil engineering investigations [6,7]. The 2-D ERT technique fits the image of both lateral and vertical contrast in ground resistivity measured using electrodes implanted on the surface of the earth [8]. The 2-D resistivity model from a 2-D ERT dataset affords an improved approximation of the subsurface model of the earth [9].

Nevertheless, images resulting from 2-D electrical resistivity surveys often produce misleading subsurface features, due to out-of-plane variation in apparent resistivity anomaly in magnitude and location [10] as cited in Eze et al. [9]. These inaccuracies frequently arise because the basic presumption of two dimensions for geological features is only an approximation. In reality, geological features/structures known in environmental/near surface research are intrinsically three-dimensional (3-D) in the attribute. Therefore, these spurious effects oftentimes lead to errors in the interpretation of 2-D ERT data.

In environmental investigations, where the subsurface geology is frequently complex, subtle and multi-scaled, the objections with 2-D ERT in precisely gauging geometrically complex structures notably in a deeply heterogeneous geologic environment without misconception necessitated the demand for 3-D resistivity imaging which is a more accurate model of the subsurface as reported in the literature [11-15].

In three-dimensional (3-D) resistivity imaging the apparent resistivity magnitudes are recognized to fluctuate in all three directions (vertical, lateral and perpendicular). Therefore, 3-D geoelectrical resistivity imaging with a 3-D model of interpretation should in theory accord a superior interpretation as noted by Loke [16].

Another extensive expression of 3-D resistivity tomography is the capability to array a 3-D resistivity model of the subsurface. A 3-D apparent resistivity volume can be realized and shown in horizontal-depth slices and vertical cross-sectional cuts next to volume rendering. Cross-sectional cuts have the improvement that values of the apparent resistivity in each cell are displayed in all directions (*x*-*y*, *y*-*z* and *x*-*z* planes). From the preceding, the dominance of 3-D ERT to 2-D ERT in detailing complex heterogeneous geological environments cannot be overemphasized, and has been validated in the reports [6,9,13].

The study area 'Okerenkoko primary school' located in Okerenkoko community in Gbaramatu Kingdom, Warri-south local government area of Delta State, was reported to be suffering from poor maintenance and negligence over a long period of time which has resulted in visible cracks observed in the classroom walls, failure/subsidence and dilapidated buildings (**Figure 1a-1c**). The degree of damage observed in the school building ranges from moderate to severe risk category according to Boscarding and Cording's [17] building damage classification. If nothing is done in addressing the situation, these are warning signs of instability/structural failure that will result in differential settlement of the dilapidated/failed buildings which causes geoenvironmental hazards. It was this extremity that necessitated the adoption of an integrated methodology that employed DC resistivity tomography involving 2-D, 3-D techniques and 1-D VES soundings supported with geotechnical-soil analysis to evaluate the geologic and geotechnical conditions of the subsurface soil and to adduce the phenomena responsible for the structural failure's observed in the school buildings.

In this paper, an orthogonal set of ten (10) 2-D resistivity imaging data all-inclusive of five (5) parallel and five (5) perpendicular traverses were obtained within the school premises (**Figure 1**). The survey was guided, with the objective of assessing the appropriateness of the site for building construction and defining the subsurface geology characteristics beneath the area.

2. Geological setting of the study area and hydrogeology

Okerenkoko community is based in the Gbaramatu Kingdom in the Warri-south local government area of Delta State (Ijaw-ethnic group). The community is positioned between latitude 05°37'39.22" to 05°37'10.12" N and longitude 005°23'30.64" to 005°23'08.79" E. It is stationed within the coastal creeks between the Benin River and the Escravos River (**Figure 2**) that links Warri and Escravos. Vegetation is defined by mangrove forests and rainforests. The Mangrove swamps are low, generally less than about 5 m above sea level.

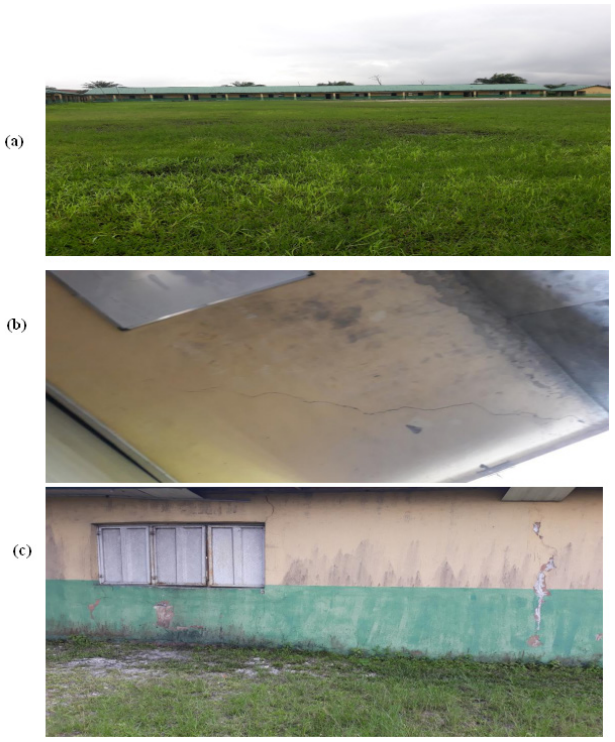

Figure 1(a-c). Physical condition of the study site (Okerenkoko primary school in Okerenkoko community) as at the time of this study showing the survey location, cracks and dilapidated buildings.

The permanent campus of Nigeria Maritime University is based in this community. Warri Southwest local government is home to the Delta State's Itekiri and Ijaw ethnic groups.

The geology of the Warri-South Okerenkoko region is located in the Niger Delta, and the geology of the region has been examined by many scholars such as Asseez [19]; Reyment [20]; Short and Stauble [21]. The stratigraphic layers of the Niger Delta include the Akata, Agbada and Benin Formations. Typical sections of these formations are briefed in other reports such as Short and Stauble [21]; Doust and Omatsola [22]; Kulke [23]. The Akata Formation is principally composed of marine shale with sandy and silty beds laid down in turbidities and continental slope channel fills, about 7000 m in thickness, serves as the source rock [22]. The Upper Agbada Formation is an array of sandstone and shale deposits [24]. It rests mainly on sand in the upper part alongside limited amount of shale, and contains shale predominantly in the lower part. Over 3,700 m thick, Benin`s upper layers are

enclosed in divers' places with thin layers of laterite of varying thickness, still, are also uncovered bordering the coast. The Somebreiro-Warri Deltaic sand is Quaternary to Recent in maturity and precisely underlies the study area. The dominant aquifer entity in the area falls inside the sands of the upper deltaic top lithofacies [25]. The water table in the study area (the first occurrence of groundwater) is estimated to lie between 4 m to 5 m beneath [26].

In general, sedimentary rocks are taken into consideration to be good aquifers due to their excessive porosity and permeability which arbitrates the hydrogeological settings of the rocks relative to its texture and mineralogy.

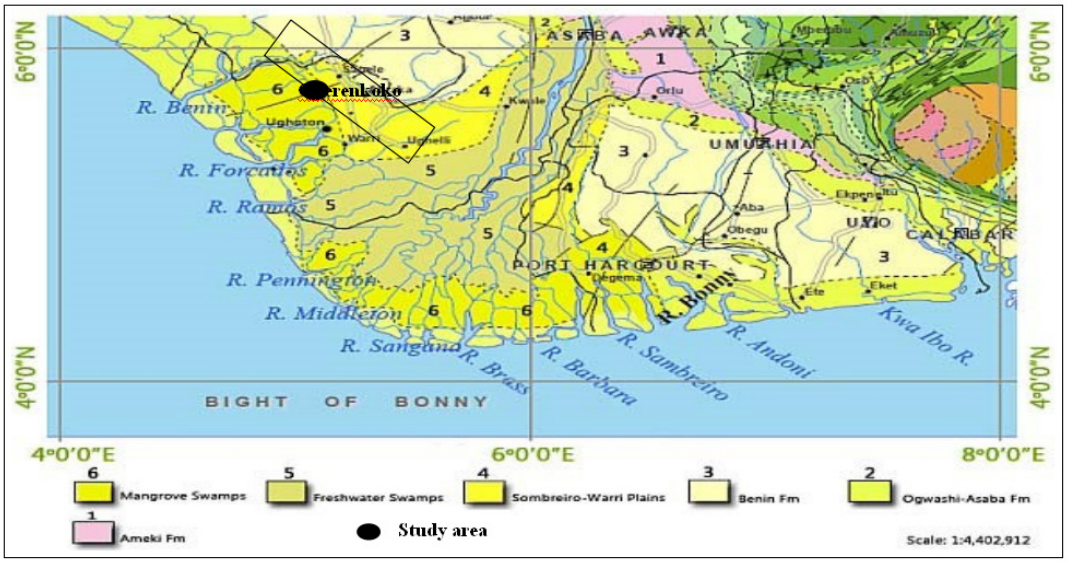

Figure 2. Geological map of the Niger Delta region showing the areal dispersal of mangrove swamps and the Benin Formation.

Source: Adapted from Nigeria Geological Survey Agency, NGSA [18].

3. Methodology

The research methods employed in carrying out this study are geophysical field measurement involving 2-D and 1-D geoelectrical resistivity surveys and geotechnical-soil analysis.

3.1 2-D electrical resistivity tomography (ERT) and 1-D vertical electrical sounding (VES)

In this study, 2-D electrical resistivity tomography data all-inclusive of five (5) parallel and five (5) vertical traverses were measured using a PASI-16GL ground resistivity meter, adopting the conventional Wenner technique (Wenner alpha), on a rectangular grid of 100 × 80 m^2 in the school premises. Thus, a total of ten (10) 2-D resistivity profiles (data density) were acquired in the study site for a reliable subsoil/geotechnical investigation beneath the school premises. In the Y-direction, 2-D profiles, Ly1 to Ly6 were established and in the X-direction, 2-D profiles, Lx1 to Lx5) were also established as shown in the base map in **Figure 3**. Inter-traverse spacing in the *-Y* and *-X* directions is 25 m and 20 m, respectively (**Figure 3**). The 2-D Wenner technique was adopted for this study because it has remarkable depth sensitivity, and because the Wenner array excels at resolving vertical variations in subsurface resistivity (horizontal structures) [8]. The electrode spacing used was 5 m in the -Y and -X directions. In the Y-direction (80 m length) with an electrode spacing of 5 m, a total of 16 electrode positions from 0 to 80 m are occupied by each traverse line, and in the X-direction (100 m length) with an electrode spacing of 5 m, a total of 21 electrode positions from 0 to 100 m are occupied by each traverse line. A total of thirteen (13) vertical electrical soundings were radially run at two positions in the grid adopting the regular Schlumberger method, with half-electrode spacing (AB/2)

varying from 1 m to 200 m. The Vertical Electrical Soundings (VES) involved radial sounding at directions 0°(N-S), 60°(NE-SW), 90°(E-W) and 120°(NW-SE) at positions 1 and position 2 respectively. The vertical electrical soundings (VES 1-13) are acquired to provide subsurface 1-D stratigraphic information to aggregate the 2-D imagery and are performed radially to establish the potential direction of groundwater flow and guide future groundwater practice at the site.

3.2 3-D electrical resistivity tomography (ERT)

To establish a good description of the study site and to minimize the errors arising from the assumption of two-dimensional geometry for geological features, a 3-D resistivity interpretation model that gives the maximum detailed results as opined by Loke [27] was simulated adopting the orthogonal set of measured 2-D apparent resistivity data. The present-day survey cost for 3-D resistivity surveys is equivalently higher than 2-D surveys [27]. Therefore, a comparison of an orthogonal set of 2-D traverse lines was used to generate the three-dimensional (3-D) apparent resistivity data used in this study.

3.3 Geophysical data processing and inversion

The VES data were analyzed by manual curve fitting to establish a resistivity model curve, that was further curve fitted to the standard curve and resulting layer parameters were entered into the Win-Resist computer program [28] and inverted to realize the geoelectric parameters (the layer resistivity, depth and thickness) of the site. In addition, vertical electrical soundings were made radially along different azimuthal angles for a given 'AB/2' interval, so we plotted this to create a polar diagram. For isotropic and uniform strata, this polar diagram is expected to be circular. However, the aberration from the circle to the eclipse indicates an anisotropic nature of the subsurface [29,30] and the possible direction of groundwater flow was inferred from the dominant trend in the polar diagram. The 2-D apparent resistivity data were inverted using the 'Earth Imager 2D program' to generate a 2-D resistivity-depth structure.

To perform 3-D inversion, we assembled the entire orthogonal set of 2-D traverses (that is, in the Y and X directions) into an exclusive 3-D dataset that can be viewed by a standard 3D resistivity inversion software [13,31] using the RES2DINV comparison code. The 3-D apparent resistivity dataset was inverted by applying Earth Imager 3D software and RES3DINV software. Using the Earth Imager 3D software, the entire 3-D dataset was inverted as a block to generate an exclusive three-dimensional resistivity image beneath the subsurface. The RES-3DINV software program uses a process established on smoothing constrained least squares inversion technique [9,32,33] to extract horizontal depth slices in the *x*-*y* plane and vertical slices in the *x*-*z* and *y*-*z* planes from the realized 3-D volume.

3.4 Geotechnical-soil evaluation

A geophysical inversion solution generates a model that should fit the local geology, geophysical field data and be interpretable. However, the principal problem with geophysical inversion is the non-uniqueness problem and one way to minimize this ambiguity is the use of additional data to constrain geophysical inversion solutions [34]. In this study, the accuracy of our geophysical ERT survey was insufficient to completely satisfy the geotechnical exploration requirements; therefore, our geophysical survey was constrained by the results of soil samples collected from three (3) holes on the site (Okerenkoko primary school) as shown on the base map (**Figure 3**). The holes were drilled along traverse 1 (Lx1), traverse 2 (Ly1) and at the center of the grid (**Figure 3**) after the time of this field survey and were confined within the first 8.0 m of each of the three traverses. Soils intended to support engineering structures, pavements, or other loads must be evaluated to predict their behavior under applied loads and variable moisture conditions. In subsoil evaluation, the water content of the soil is very critical to grading its engineering properties. The water content at which soil changes from one state to the other is known as the consistency limit, or Atterberg's limit [35]. The Atterberg limits are an important measure of the critical water content of fine-grained soils: Its shrinkage limit, plastic limit and liquid

limit. Depending on the water content, soil can be in one of four states: Solids, semi-solids, plastics, liquids. Each state has different soil consistency and behavior, and therefore different geotechnical properties [35,36].

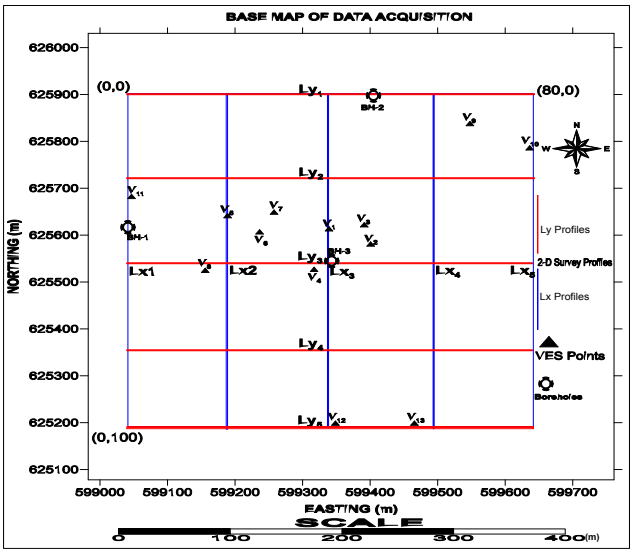

Figure 3. Data acquisition map showing the 2-D resistivity survey grid lines, VES points and Boreholes occupied in the study site (Okerenkoko primary school, Warri-south, Delta State, Nigeria).

The shrinkage limit (SL) is the amount of water above which loss of water does not reduce the sample volume. The plasticity limit (PL) is the amount of water at which a plastic transitions to a semi-solid state, while the liquid limit (LL) is the amount of water at which the soil goes from a plastic state to a liquid state if the soil sample is sufficiently liquid [35,36]. Shrinkage limits are used much less frequently than liquid and plastic limits. The practical importance of the liquid-plastic boundary lies in its ability to reflect the types and amounts of clay minerals present in fine fractions. High values of liquid limit and plasticity index indicate that the soil has high clay and colloidal size of active minerals and that such soil has a poor base for bearing capacity [37].

In this study, soil samples for geotechnical testing were collected in plastic bags and sent to the Soil Research Laboratory at the Department of Earth Sciences, Federal University of Petroleum Resources, Effurun (FUPRE) for analysis. The samples were air-dried and ground into small pieces. The ground sample was then sieved by him through a 4.25 mm aperture. Moisten the sieved soil with a normal concentration of tap water (pH = 7.2), seal the moistened soil in a plastic bag and store for 3 days to meet the British Standard [38].

Fundamental tests performed on soil samples include methods to determine the liquid limit, plastic limit, and plasticity index. These were carried out according to standard practice [38]. The boundary between liquid and plasticity in the soil is called the Atterberg limit.

In each case, the basic requirement is the determination of the water content or moisture content (Wc) of the soil samples at a different number of blows or drops (N).

In each case, the water content (Wc) for each blow was determined using the formula:

$$W_c = \frac{weight\ of\ wet\ soil\ sample}{weight\ of\ dry\ soil\ sample} \times \frac{100}{1} \quad (1)$$

For soil sample-1 collected from the borehole (BH-1) the number of blows/drops used was 6, 14 and 34 blows and water content was determined for each blow respectively. In soil sample-2 collected from the borehole (BH-2) the number of blows/drops used was 13, 23 and 54 blows and water content was determined for each blow while in soil sample-3 collected at borehole (BH-3) the number of blows/drops used was 18, 23 and 30 blows respectively and water content were determined for each blow.

For liquid limit determination we plotted the water content (Wc) values against the corresponding number of drops, N, on a semilogarithmic graph with water content on the arithmetical/linear scale, and the number of drops on the logarithmic scale. A best-fit straight line was drawn through the plotted points. The water content corresponding to the intersection of the line with 25 (N) drops on the logarithmic axis was read as the liquid limit, LL, of the soil in each sample. The plastic limit was also determined using the procedure and data required for plastic limit determination which involves the determination of the water content in the soil sample after oven drying for a number of trials. The plastic limit was taken as the average moisture content for the number of trails. In each case the plasticity index (I_p) of the soil samples

was determined by finding the difference between the liquid and plastic limits as shown below:

$$I_p=LL-PL \quad (2)$$

After determining the liquid limit and plastic limit (Atterberg's limit) of the soil samples, the soil type was classified using the Burmister [39] scheme shown in **Table 1**.

Table 1. Plasticity Indices and Corresponding States of Plasticity (after Burmister [39]).

Soil type	Plastic limit	State of Plastic
1	0	Non-Plastic
2	1-5	Slight
3	5-10	Low
4	10-20	Medium
5	20-40	High
6	>40	Very High

4. Results and discussion

4.1 Vertical electrical sounding (VES)

In a nutshell, the VES model values realized from 1-D resistivity inversion are presented in **Table 2**. The iteration outcome of 1-D inversion for VES 1-6 only shows the sounding curves, inverted layer variables and root mean square (RMS) error depicted in **Figure 4a-4f**. A low RMS error in the order of 6.6%, 2.4%, 2.2%, 2.7%, 3.6%, 2.6%, 3.1%, 2.1%, 2.2%, 2.5%, 2.5%, 2.9%, and 2.8% was actualized in the 1-D inversion of VES 1, 2, 3... to 13 respectively (as shown in **Table 2**). These low RMS errors endorse the accuracy of the VES model resistivity values. Interpretation of VES data brought to light four geoelectric layers within the subsurface classified as topsoil, dry sand, wet sand and peat/clay/sandy clay (**Table 2**). From the layer parameters and inferred lithology shown in **Table 2**, the subsurface is principally sandy in lithology with varying degrees of water saturation. Dry/consolidated sand (ρ between 600 Ωm to ρ ≥ 1000 Ωm) was observed predominantly at the second geoelectric layers from a depth range of 2.9 m to 10.4 m from VES 1 to 13 (**Table 2**). In **Table 2**, it was observed that wet sand (ρ < 200 Ωm), Peat/clay (ρ ≤ 20 Ωm) and Sandy clay (ρ between 20 Ωm to 50 Ωm and below 90 Ωm), were predominant at the third and fourth layers at a depth range of 9.9 m to 27.8 m and beyond 30.0 m respectively. The presence of mechanically weak/unstable Peat/clay/Sandy clay layers at the third and fourth layers at profound depths within the near surface (27.8 m to 30.0 m) apparently shows that the subsurface layers at these depths are weak and not suitable for engineering structures. Although, the dry/consolidated sandy layer observed within the second geoelectric layer is competent as a foundation base for building structures [40], the underlying layers of weak and mechanically unstable peat/clay/sandy clay make it vulnerable to failure. In general, clay soils exhibit unfavorable geotechnical properties (when saturation), due to their low strength, high compressibility and high level of volumetric changes which cause negative defects in engineering structures. This explains the visible cracks/subsidence observed in the buildings at the primary school. The second-layer, third-layer and fourth-layer resistivity maps for VES 1 to 13, are shown in **Figure 5a-5c**. The maps show resistivity variation within the second layers at a depth ranging from 2.90 m to 10.40 m (**Table 2**), third layers at a depth ranging from 9.60 m to 27.80 m (**Table 2**) and fourth layers at a depth beyond 30.0 m. In general, resistivity in sedimentary rocks is influenced by porosity [41], void space, degree of sorting and grain size assessment [42].

For this reason, within each layer, groundwater flows from higher resistivity zones (with low porosity) to lower resistivity zones (with high porosity). This implies that within a layer, areas that are less resistive tend to be more saturated due to high porosity and will have higher water saturation than areas with high resistivity (as indicated in **Figure 5a-5c**). From the second layer resistivity map, it was observed that high water saturation within this layer (depth ranged from 2.9 m to 10.4 m) was predominant in the northeastern and northwestern parts of the site due to low resistivity values (100-700 Ωm) as shown in **Figure 5a**, third layer resistivity map (depth ranged from 9.6 m to 27.8 m) showed high water saturation in the northeastern and western parts of the site, but pre-

dominant in the northeast part with very low resistivity values (40-120 Ωm) as shown in **Figure 5b**. The fourth layer resistivity map showed very high water saturation predominant within this layer (at depth beyond 30 m) as indicated in **Figure 5c**. In **Figure 5a-5c** it was observed that the degree of water saturation in the study site apparently increased with respect to depth, with the fourth geoelectric layer map (**Figure 5c**) showing more zones with a high water saturation than the overlying third and second layers (**Figure 5a-5b**). This observation shows that the subsurface geological structure of the site contains materials with high water content which affects their strength and volumetric properties. These findings reflect the dominance of non-competent materials in the study area. The anisotropy polygon based on the radial VES survey is shown in **Figure 6a-6b**. The dominant resistivity trends (as indicated) show that the flow direction of water is comparable to that depicted in the layer resistivity maps in **Figure 5a-5c**.

4.2 2-D electrical resistivity tomography (ERT)

The outcomes from 2-D ERT for the ten (10) traverses are shown in **Figure 7a-7j**. The 2-D resistivity-depth sections were labeled according to the traverse line directions (***-X*** and ***-Y***) occupied within the 3-D grid as shown in the data acquisition base map (**Figure 3**). In the (***-X***) direction the 2-D lines were 100 m in length and labeled as (Lx1, Lx2, Lx3, Lx4 and Lx5) while in the (***-Y***) direction the 2-D lines were 80 m in length and labeled as (Ly1, Ly2, Ly3, Ly4 and Ly5). In either case, the subsurface resistivity structure was imaged to reasonable depths suitable for precise assessment of its suitability for engineering practice. Correlating the 2-D resistivity interpretation with resistivity values realized from 1-D inversion (VES survey), it is symbolic of sand lithology with alternating degrees in water content. The 2-D resistivity section for line Lx1 (Traverse 1) with resistivity ranging from 3.7-1113 Ωm is shown in **Figure 7a**. A high resistivity structure (267-1113 Ωm) was observed at depth of 0 to 8.2 m within the subsurface at an electrode position of 0-100 m and indicative of a dry sand layer which was interpreted as the zone of better consolidation favorable for the construction of building structures. At depths between 8.6 m to 17.1 m, a very low resistivity variation of 3.7-64 Ωm was observed which is symbolic of peat/clay/sandy clay layers, not suitable for engineering practice (**Figure 7a**). The 2-D resistivity section for line Lx2 (Traverse 5) with resistivity ranging from 1.0-10,000 Ωm is shown in **Figure 7b**. A high resistivity structure (1000-10000 Ωm) was observed at depths of 0 to 8.6 m, 1-8.6 m and 0-10.0 m at electrode positions of 5-25 m, 30-60 m and 65-100 m respectively along this traverse. This resistivity value is symbolic of dry sands with little or no water content, which was interpreted as the zone of better consolidation favorable for engineering practice. At depth between 12.8 m to 17.1 m and 6.0 m to 17.1 m at an electrode position of 15-95 m, a very low resistivity variation of 1.0-10 Ωm was observed, which is symbolic to peat/clay layers, not suitable for engineering practice (**Figure 7b**). Between the consolidated layer and peat/clay layer moderate resistivity structure (100 Ωm) was observed sandwiched between these layers and is indicative of wet sand. The 2-D resistivity section for line Lx3 (Traverse 6) with resistivity ranging from 2.9-10,000 Ωm is shown in **Figure 7c**. A high resistivity structure (1302-10000 Ωm) was observed at depth of 0 to 6.0 m at electrode position of 0-100 m along this traverse. This resistivity value is symbolic of dry sands with little or no water content, which was interpreted as the zone of better consolidation favorable for engineering practice. At depths between 4.3 m to 8.6 m and 8.6 m to 17.1 m, moderate (170 Ωm) and very low (2.9-22.1 Ωm) resistivity structures were observed which are symbolic of wet sand and peat/clay layers, respectively (**Figure 7c**). These layers were assessed to be weak and not suitable for engineering practice. The 2-D resistivity section for line Lx4 (Traverse 7) with resistivity ranging from 1.6-7510 Ωm is shown in **Figure 7d**. A high resistivity structure (909-7510 Ωm) was observed at depth of 0 to 8.6 m at electrode positions of 0-85 m and 90-100 m along this traverse. This resistivity value is symbolic of dry sands with little or no water content, which was interpreted as the zone of better consoli-

dation favorable for engineering practice. At depths between 5.0 m to 6.0 m and 6.0 m to 17.1 m, moderate (110 Ωm) and very low (1.6-13.3 Ωm) resistivity structures were observed which are symbolic of wet sand and peat/clay layers, respectively (**Figure 7d**). These layers were also assessed to be weak and not suitable for engineering practice. The 2-D resistivity section for line Lx5 (Traverse 3) with resistivity ranging from 27.8-1758 Ωm is shown in **Figure 7e**. A high resistivity structure (624-1758 Ωm) was observed at depth of 0 to 9.0 m at an electrode position of 0-100 m along this traverse. This resistivity value is symbolic to dry sands with little or no water content, which was interpreted as the zone of better consolidation favorable for engineering practice. At depths between 9.0 m to 13.0 m and 13.0 m to 17.1 m, moderate (221 Ωm) and very low (27.8-78 Ωm) resistivity structures were observed which are symbolic of wet sand and peat/clay/sandy clay layers, respectively (**Figure 7e**). These layers were also assessed to be weak and not suitable for engineering practice. The 2-D resistivity section for line Ly1 (Traverse 2) with resistivity ranging from 38.9-1584 Ωm is shown in **Figure 7f**. A high resistivity structure (627-1584 Ωm) was observed at depth of 0 to 7.0 m at an electrode position of 0-55 m and a depth of 0 to 6.0 m at electrode position of 68-75 m along this traverse. This resistivity value is symbolic to dry sands with little or no water content, which was interpreted as the zone of better consolidation favorable for engineering practice. At depths between 7.1 m to 8.6 m and 8.6 m to 14.3 m, moderate (248 Ωm) and low (38.9-98.0 Ωm) resistivity structures were observed, which is symbolic of wet sand and peat/clay/sandy clay layers, respectively (**Figure 7f**). These layers were assessed to be weak and not suitable for engineering practice. The 2-D resistivity section for line Ly2 (Traverse 8) with resistivity ranging from 21.5-9716 Ωm is shown in **Figure 7g**. A very high resistivity structure (2106-9716 Ωm) was observed at depths of 0 to 5.0 m, 0-4.8 m and 0-7.1 m at electrode positions of 5-15 m, 30-52 m, 55-65 m and 67-75 m respectively along this traverse. This resistivity value is symbolic of dry sands with little or no water content, which was interpreted as the zone of better consolidation favorable for engineering practice. At depths between 0-7.1 m and 7.1 m to 14.3 m, moderate (457 Ωm) and low (21.5-99.0 Ωm) resistivity structures were observed which is symbolic of wet sand and peat/clay/sandy clay layers, respectively (**Figure 7g**). These layers were also assessed to be weak and not suitable for engineering practice. The 2-D resistivity section for line Ly3 (Traverse 9) with resistivity ranging from 7.9-4871 Ωm is shown in **Figure 7h**. A high resistivity structure (977-4871 Ωm) was observed at depth of 0 to 6.5 m at an electrode position of 5-80 m along this traverse. This resistivity value is indicative of dry sands with little or no water content, which was interpreted as the zone of better consolidation favorable for engineering practice. At depths between 6.5-8.0 m and 8.0 m to 14.3 m, moderate (196 Ωm) and low (7.9-39.3 Ωm) resistivity structures were observed, which is symbolic of wet sand and peat/clay/sandy clay layers, respectively (**Figure 7h**). These layers were also assessed to be weak and not suitable for engineering practice. The 2-D resistivity section for line Ly4 (Traverse 10) with resistivity ranging from 6.1-6442 Ωm is shown in **Figure 7i**. A very high resistivity structure (1130-6442 Ωm) was observed at depth of 0 to 7.1 m of the subsurface at an electrode position of 5-80 m along this traverse. This resistivity value is symbolic of dry sands with little or no water content which was interpreted as the zone of better consolidation favorable for engineering practice. At the near surface (< 5 m) at an electrode position of 0-5 m, a low resistivity structure was observed (**Figure 7i**). At depths between 7.1 m to less than 10 m and 9.0 m to 14.3 m, moderate (198 Ωm) and low (6.1-34.8 Ωm) resistivity structures were observed which are symbolic of wet sand and peat/clay/sandy clay layers, respectively (**Figure 7i**), which are weak and not suitable for engineering practice. The 2-D resistivity section for line Ly5 (Traverse 4) with resistivity ranging from 2.5-9934 Ωm is shown in **Figure 7j**. A high resistivity structure (1249-9934 Ωm) was observed at depth of 0.9 m to 7.1 m at electrode positions of 5-12 m, 0-

6.0 m at electrode positions of 20-25 m, 28-35 m, 37-40 m and 55-75 m respectively along this traverse. This resistivity value is symbolic of dry sands with little or no water content, which was interpreted as the zone of better consolidation favorable for engineering practice. At depths between 7.1 m to 10.7 m and 10.7 m to 14.3 m, moderate (157 Ωm) and low (2.5-19.7 Ωm) resistivity structures were observed which are symbolic of wet sand and peat/clay layers, respectively (**Figure 7j**). These layers were also assessed to be weak and not suitable for engineering practice.

In general, the interpretation of the ten (10) 2-D apparent resistivity-depth sections (**Figure 7a-7j**) showed consistency in their subsurface resistivity structure within the depths imaged in the study area, with a dominance of peat/clay/sandy clay materials with very low resistivity values observed predominantly at varying depths i.e. 8.6-17.1 m in profile Lx1, 12.8-17.1 m in profile Lx2, 8.6-17.1 m in profile Lx3, 6.0-17.1 m in profile Lx4, 13.0-17.1 m in profile Lx5, 8.6-14.3 m in profile Ly1, 7.1-14.3 m in profile Ly2, 8.0-14.3 m in profile Ly3, 9.0-14.3 m in profile Ly4 and 10.7-14.3 m in profile Ly5 (**Figure 7a-7j**). Therefore, the overlain dry sand layers with high resistivity values at the near surface interpreted as the zone of better consolidation will still suffer from subsidence due to the underlying mechanically unstable peat/clay/sandy clay layers which are highly mobile in response to volumetric changes which cause negative defects to build structures and as a deduction, explains the visible cracks/failure/subsidence observed on structures within the study site (**Figure 1a-1c**).

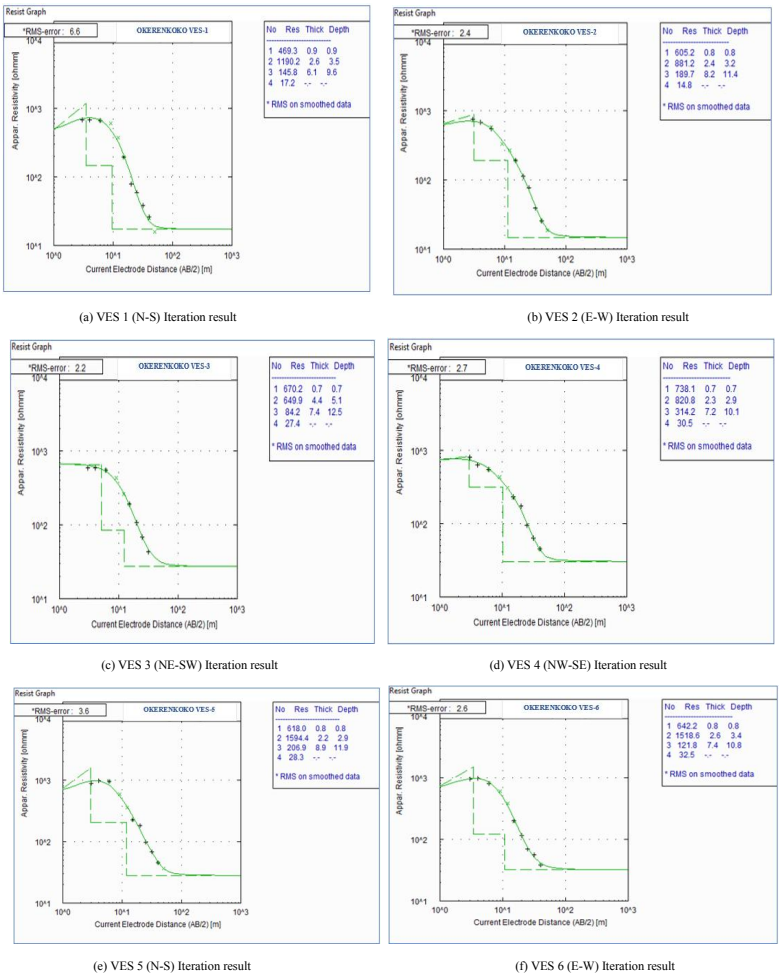

(a) VES 1 (N-S) Iteration result

(b) VES 2 (E-W) Iteration result

(c) VES 3 (NE-SW) Iteration result

(d) VES 4 (NW-SE) Iteration result

(e) VES 5 (N-S) Iteration result

(f) VES 6 (E-W) Iteration result

Figure 4(a-f). Iteration results of 1D resistivity inversion for VES 1 to 4 Location 1 and VES 5 and 6 Location 2, showing the resistivity sounding curves and 1-D resistivity models.

Table 2. Summary of VES results in the study site, showing resistivity values, thicknesses, depths and inferred lithology.

VES-No / RMS-Error	Layers		Resistivity (Ω-m)	Thickness (m)	Depth (m)	Inferred lithology
RADAR SOUNDING-1 (VES 1 to 4)						
VES-1 (N-S) RMS: 6.6	1		469.3	0.9	0.9	Topsoil
	2		1190.2	2.6	3.5	Consolidated Sand
	3		145.8*	6.1	9.6	*Wet Sand
	4		17.2	---	---	**Peat/clay
VES-2 (E-W) RMS: 2.4	1		605.2	0.8	0.8	Topsoil
	2		881.2	2.4	3.2	Sand (Dry)
	3		189.7*	8.2	11.4	*Sand (Wet)
	4		14.8	---	---	**Peat/clay
VES-3 (NE-SW) RMS: 2.2	1		670.2	0.7	0.7	Topsoil
	2		649.9	4.4	5.1	Sand (Dry)
	3		84.2	7.4	12.5	**Sandy Clay
	4		27.4	---	---	**Clay
VES-4 (NW-SE) RMS: 2.7	1		738.1	0.7	0.7	Topsoil
	2		820.8	2.3	2.9	Sand (Dry)
	3		314.2*	7.2	10.1	*Sand
	4		30.5	---	---	**Clay/Sandy clay
RADAR SOUNDING-2 (VES 5 to 8)						
VES-5 (N-S) RMS: 3.6	1		618.0	0.8	0.9	Topsoil
	2		1594.4	2.2	2.9	Consolidated Sand
	3		206.9*	8.9	11.9	*Sand
	4		28.3	---	---	**Clay
VES-6 (E-W) RMS: 2.6	1		642.2	0.8	0.8	Topsoil
	2		1518.6	2.6	3.4	Consolidated Sand
	3		121.8*	7.4	10.8	*Sand (Wet)
	4		32.5	---	---	**Clay/Sandy clay
VES-7 (NE-SW) RMS: 3.1	1		790.6	1.0	1.0	Topsoil
	2		1162.1	2.6	3.6	Consolidated Sand
	3		197.3*	6.8	10.4	*Sand (Wet)
	4		38.9	---	---	**Clay/Sandy clay
VES-8 (NW-SE) RMS: 2.1	1		635.6		0.7	Topsoil
	2		1435.4	2.4	3.1	Consolidated Sand
	3		252.8*	7.2	10.3	*Sand
	4		43.5	---	---	**Sandy Clay
VES-9 RMS:2.2	1		443.7	1.1	1.1	Topsoil
	2		1078.3	3.5	4.6	Consolidated Sand
	3		199.6	21.2	25.8	*Sand
	4		17.8	---	---	**Peat/clay
VES-10 RMS: 2.5	1		1150.3	0.7	0.7	Topsoil
	2		961.2	4.8	5.6	Dry Sand
	3		170.9	14.2	19.7	*Wet Sand
	4		24.1	39.7	59.4	**Clay
	5		82.8	--	--	**Sandy clay

Table 2 continued

VES-No / RMS-Error	Layers		Resistivity (Ω-m)	Thickness (m)	Depth (m)	Inferred lithology
VES-11 RMS: 2.5	1		1867.5	1.3	1.3	Topsoil
	2		467.8	9.1	10.4	Sand (Dry)
	3		63.8	61.1	71.5	**Sandy clay
	4		227.3	--	--	Sand
VES-12 RMS: 2.9	1		645.7	0.8	0.8	Topsoil
	2		864.0	3.4	4.2	Dry Sand
	3		148.9	23.6	27.8	*Wet Sand
	4		20.1	--	--	Peat/clay
VES-13 RMS: 2.8	1		266.4	0.8	0.8	Topsoil
	2		760.7	3.2	4.0	Dry Sand
	3		138.5	14.8	18.8	*Wet Sand
	4		16.5	48.6	67.4	**Peat/clay
	5		140.6	--	--	*Wet Sand

*Sandy layer; **Peat/Clay/Sandy clay layer

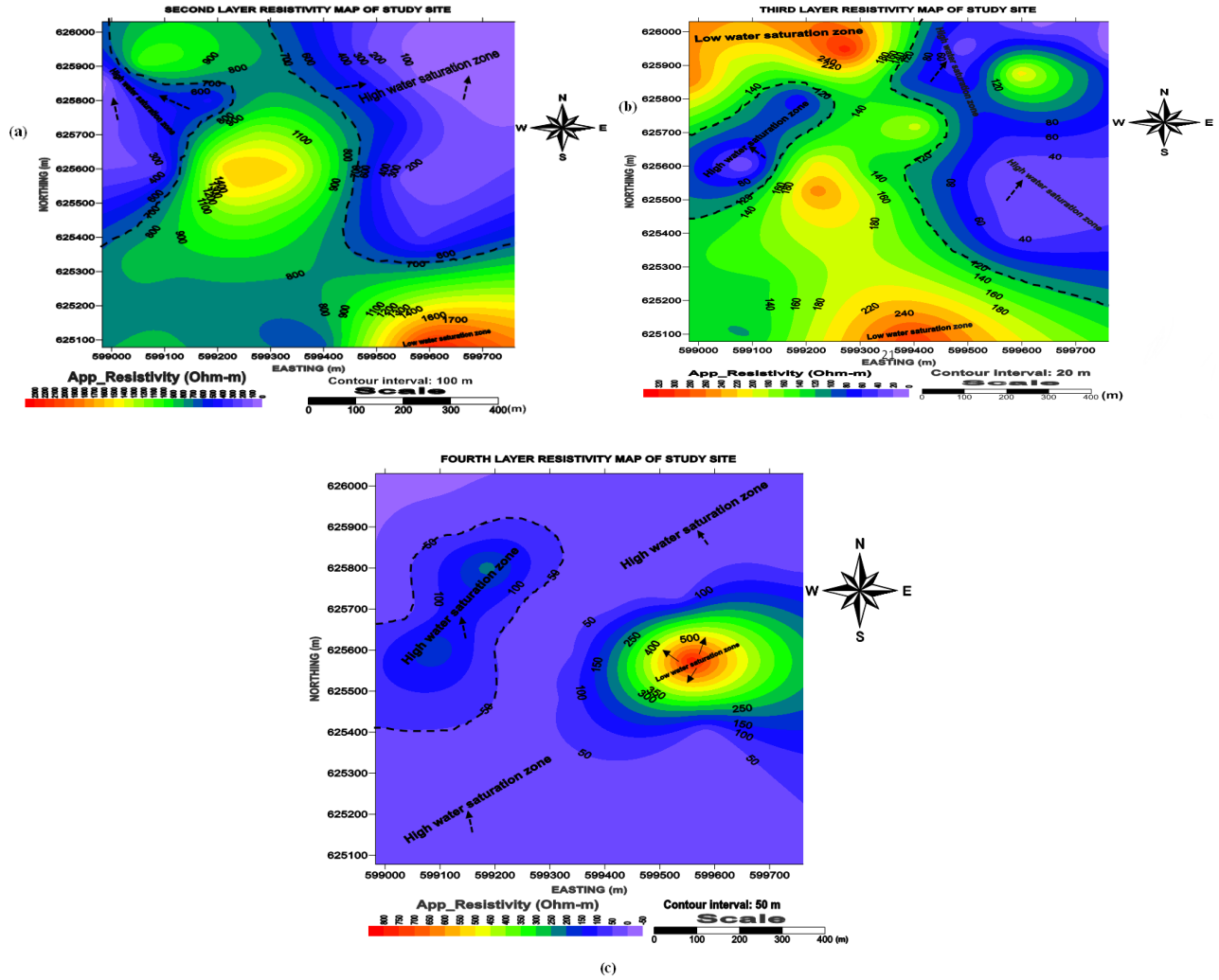

Figure 5. (a) Second geoelectric layer Map VES 1 to 13; (b) Third geoelectric layer Map VES 1 to 13; (c) Fourth geoelectric layer Map VES 1 to 13. From the maps, resistivity is low towards the northeastern part of the site (see black arrows).

Figure 6. Radar sounding plots (a) polar diagram showing the anisotropy polygon of radar sounding for VES 1 to 8; (b) Chart title for VES 1 to 8 radial sounding.

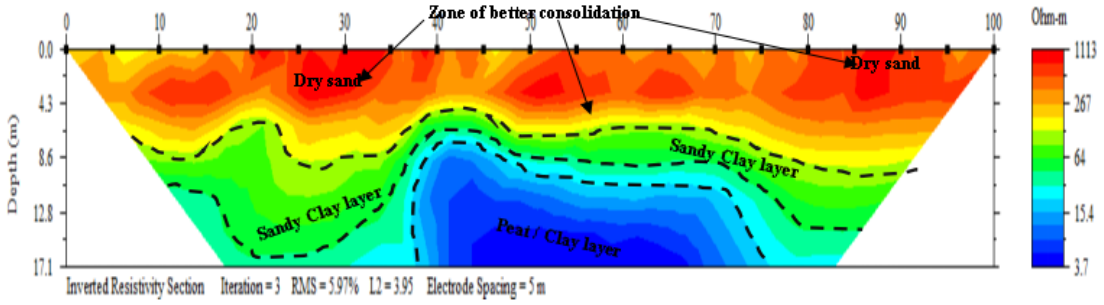

(a) 2D resistivity-depth section for line Lx1 (Traverse 1)

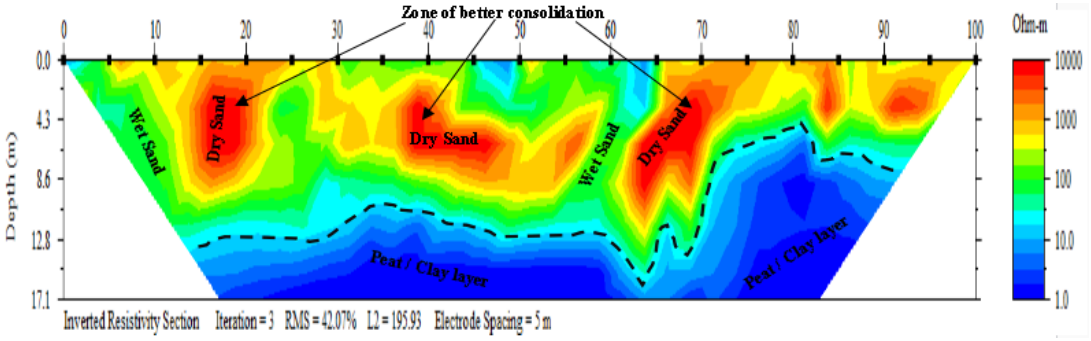

(b) 2D resistivity-depth section for line Lx2 (Traverse 5)

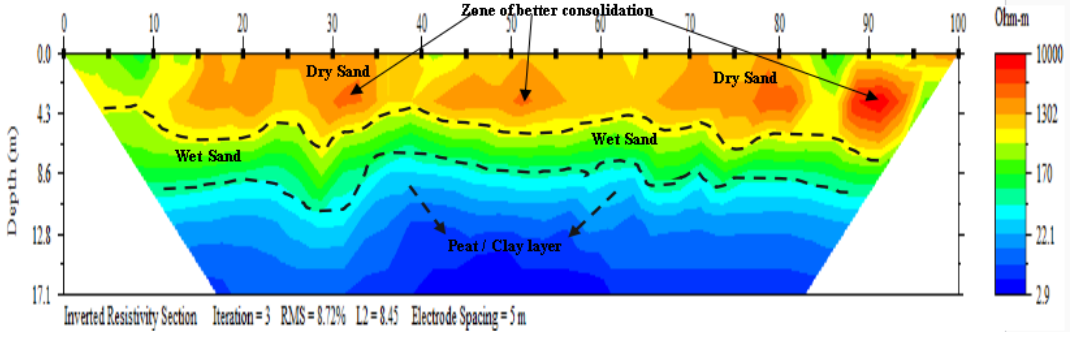

(c) 2D resistivity-depth section for line Lx3 (Traverse 6)

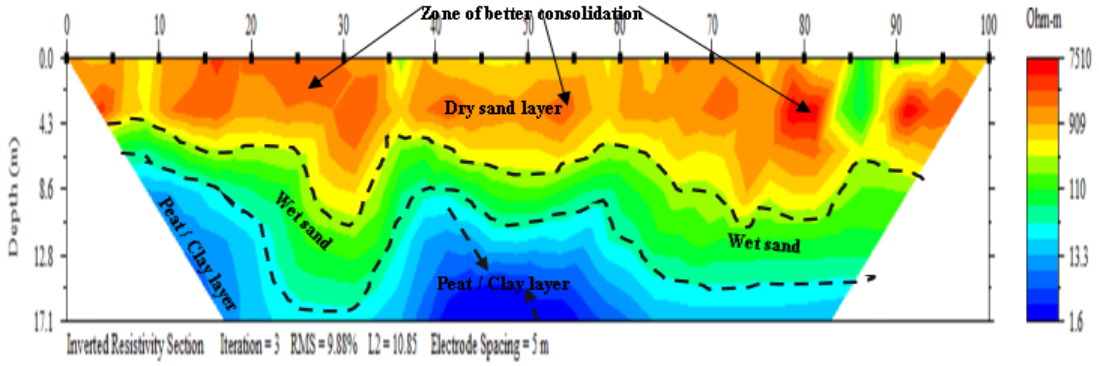

(d) 2D resistivity-depth section for line Lx4 (Traverse 7)

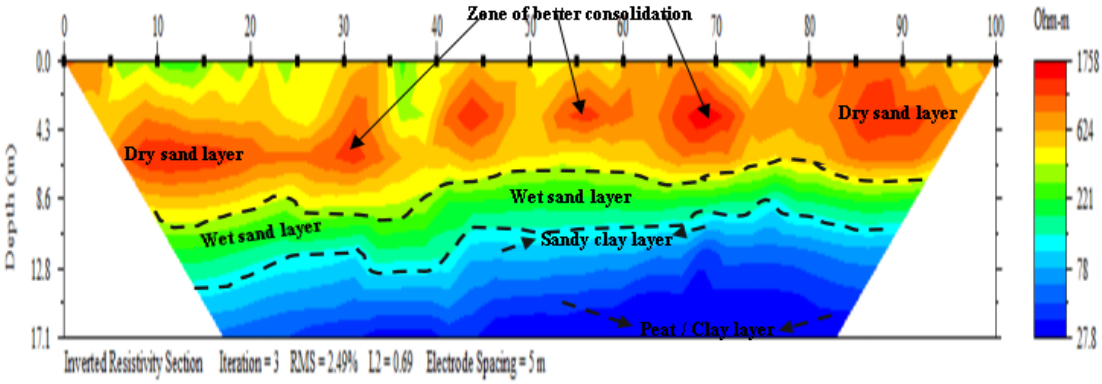

(e) 2D resistivity-depth section for line Lx5 (Traverse 3)

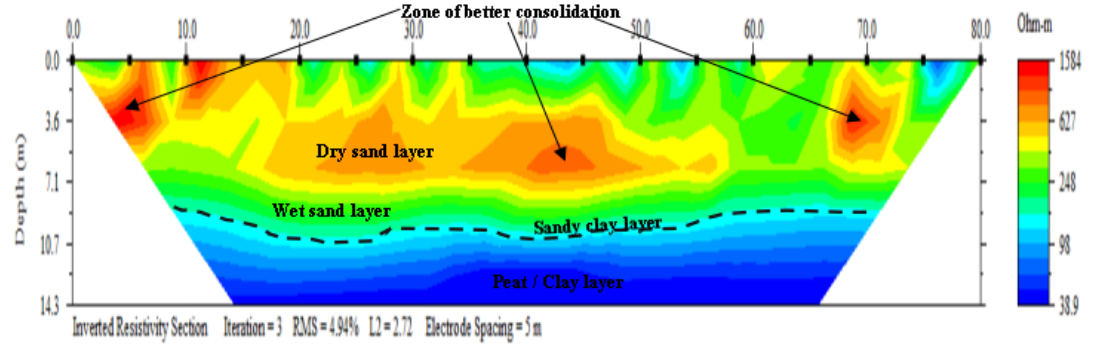

(f) 2D resistivity-depth section for line Ly1 (Traverse 2)

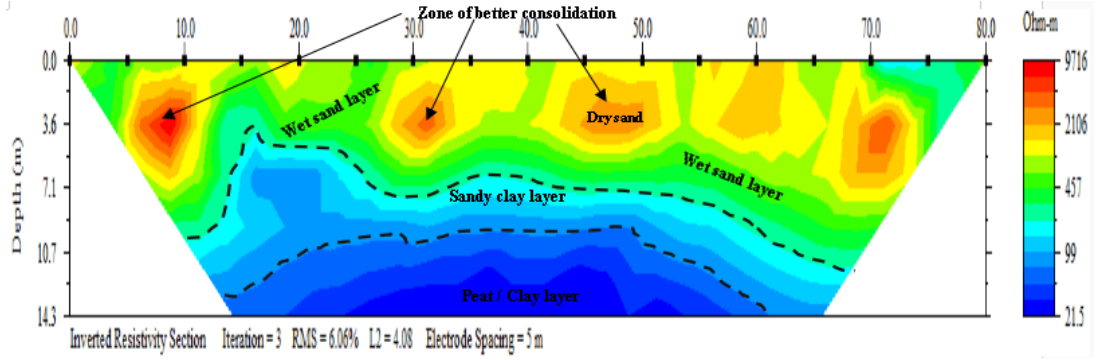

(g) 2D resistivity-depth section for line Ly2 (Traverse 8)

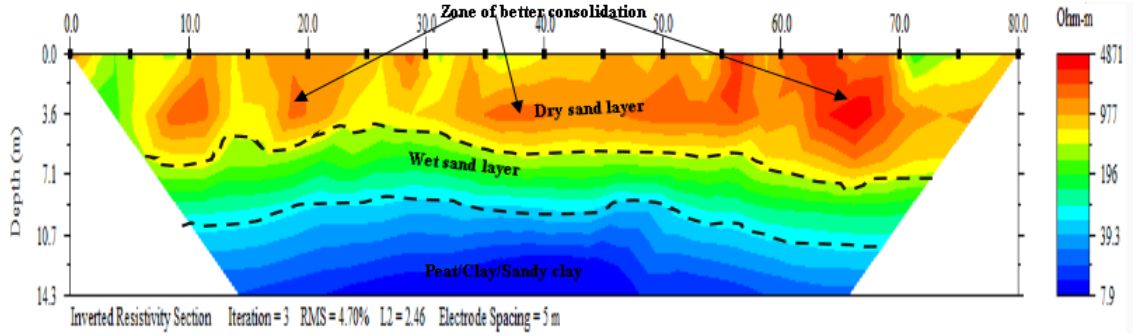

(h) 2D resistivity-depth section for line Ly3 (Traverse 9)

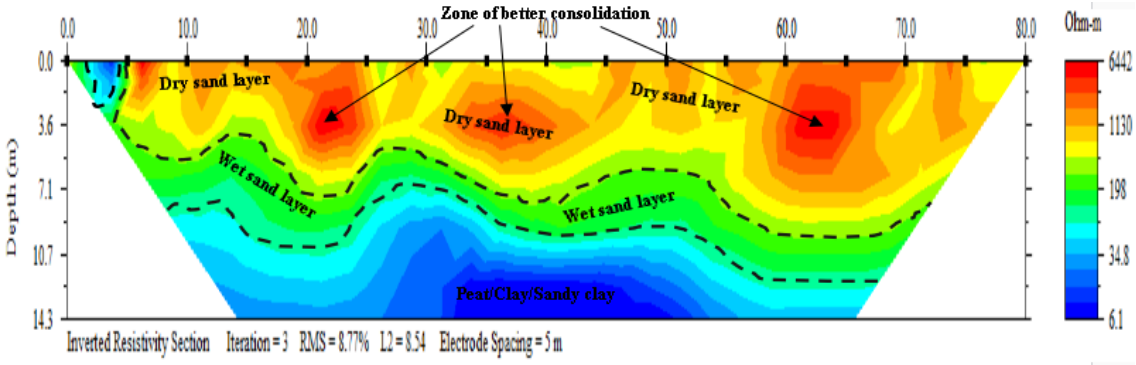

(i) 2D resistivity-depth section for line Ly4 (Traverse 10)

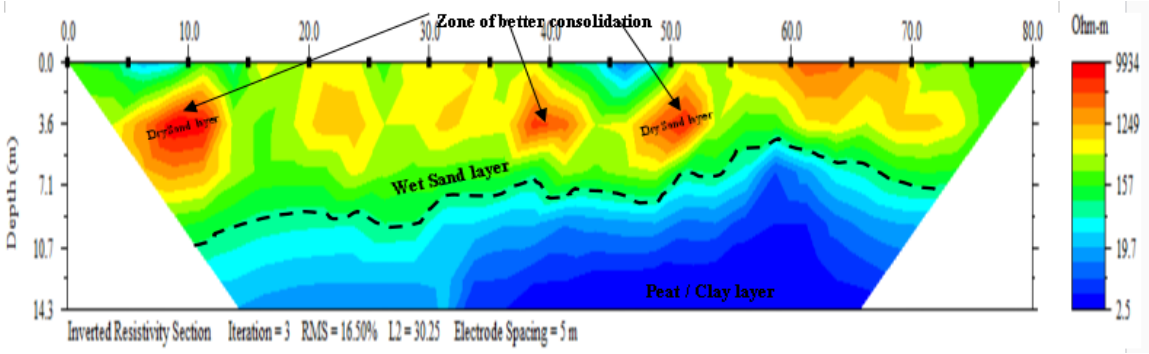

(j) 2D resistivity-depth section for line Ly5 (Traverse 4)

Figure 7(a-j). showing the 2D resistivity-depth structure of the subsurface.

4.3 3-D electrical resistivity tomography (ERT)

The 3-D resistivity volume of the study site simulated from the orthogonal set of 2-D apparent resistivity field data is shown in **Figure 8**. The 3-D resistivity volume displays resistivity changes in the vertical, lateral and perpendicular directions down to a depth of 19.8 m within the subsurface. The 3-D volume reflects the dominance of low resistivity materials (11-69 Ωm) which are symbolic of peat/clay/sandy clay layers (as indicated in **Figure 8**). High resistivity values (2572-15744 Ωm) were also detected at the top, indicative of dry sand. These findings were also observed from the 2-D ERT interpretation shown in **Figure 7a-7j**. Therefore, the low resistivity layers of peat/clay/sandy clay delineated from a depth of 6.6 m to 19.8 m (**Figure 8**) are responsible for the structural failures i.e. cracks/dilapidated structures observed in the buildings (**Figure 1a-1c**) due to mechanical instability and high volumetric changes associated with peat/clay layers, which results in differential settlement over time. This ex-

plains the degree of cracks/damage observed in the school buildings which ranges from moderate to severe risk according to Boscarding and Cording's [17] damage classification.

The 3-D resistivity inversion was also extended by displaying horizontal depth slices and vertical slices from the realized 3-D model volume shown in **Figure 8**. This procedure was actualized using smoothness constrained least-squares inversion process in the RES3DINV program.

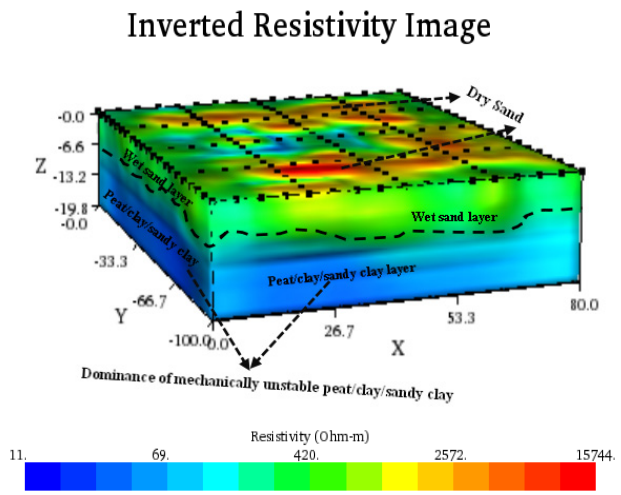

Figure 8. 3-D resistivity tomography volume beneath the study area.

The horizontal-depth slices displayed six layers at depth of 0.00 to 2.50 m in layer 1, 2.50 m to 5.38 m in layer 2, 5.38 m to 8.68 m in layer 3, 8.68 m to 12.5 m in layer 4, 12.5 m to 16.9 m in layer 5 and 16.9 m to 21.9 m in layer 6 (**Figure 9a**). The trend of resistivity variations noted in the 3-D inversion depth slices showed low resistivity materials becoming more evident from the third to the sixth layer. In the first and second layers at depths ranging from 0.00 to 2.50 m and 2.50 m to 5.38 m respectively, high resistivity structures (ρ between 527-1105 Ωm) symbolic of dry sand were observed (**Figure 9a**). In the third layer at a depth ranging from 5.38 m to 8.68 m, a low resistivity structure (ρ between 57.1-120 Ωm) was observed, which is symbolic of sandy clay/wet sand layers (**Figure 9a**). In the fourth, fifth and sixth layers, at a depth ranging from 8.68 m to 12.50 m, 12.5 m to 16.9 m and 16.9 m to 21.9 m respectively, very low resistivity structures (ρ between 6.2-27.2 Ωm) were observed which are symbolic of peat/clay materials within the subsurface (**Figure 9a**). These findings are consistent with the results of 2-D ERT interpretation where the dominance of peat/clay/sandy clay was delineated and observed within a similar depth as imaged in 3-D tomography. Therefore, the subsurface geological structure of the area consists of high-resistivity materials (dry sand) underlain by very low resistivity and mechanically unstable layers of peat/clay/sandy clay which are not favorable for engineering structures within the depths imaged from 2-D and 3-D resistivity tomography. 2-D vertical slices were also extracted from the 3-D depth slices and displayed in the *x-z* and *y-z* plane cells (**Figure 9b-9c**).

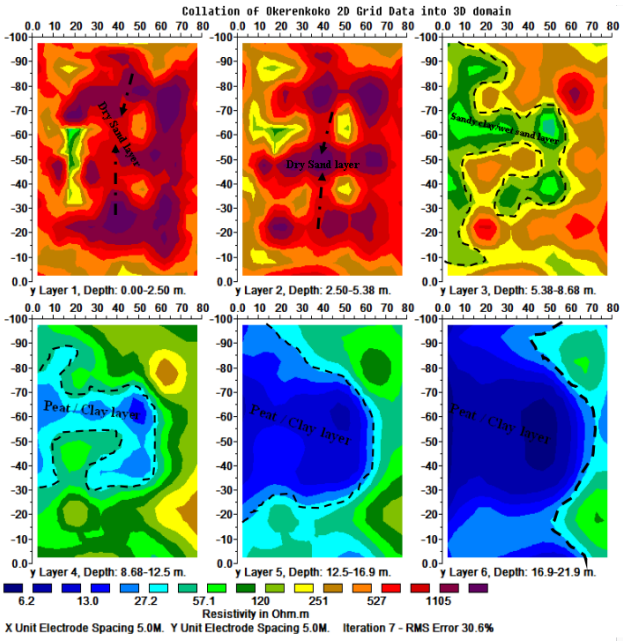

Figure 9a. Six-layer horizontal depth slices obtained from 3-D inversion of orthogonal 2-D profiles using smoothness constrained least-squares inversion.

One of the divergent superiorities of 3-D resistivity inversion over 2-D inversion was checked by matching the 2-D inversion sections in **Figure 7a-7j**, with the 3-D resistivity tomography images and 2-D images extracted from the 3-D inversion models (**Figures 8 and 9**). 3-D resistivity tomography gave continuous variations in apparent resistivity values in all three directions (vertical, lateral and perpendicular) to profound depths of 19.8 m and 21.9 m than in 2-D ERT which imaged the subsurface to a maxi-

mum depth of 17.1 m.

Furthermore, 2-D images extracted from 3-D inversion displayed improved image accuracy and subsurface variation of materials which are based on changes in apparent resistivity values beneath the subsurface in the *x-z* and *y-z* planes within the 3-D grid than in the 2-D inversion sections.

4.4 Geotechnical soil analysis

Geotechnical analysis of soil samples is a necessary requirement for an engineering site characterization program. The water content of the soil samples was evaluated using Equation (1). The results of water content for the three (3) soil samples are presented in **Tables 3-5**.

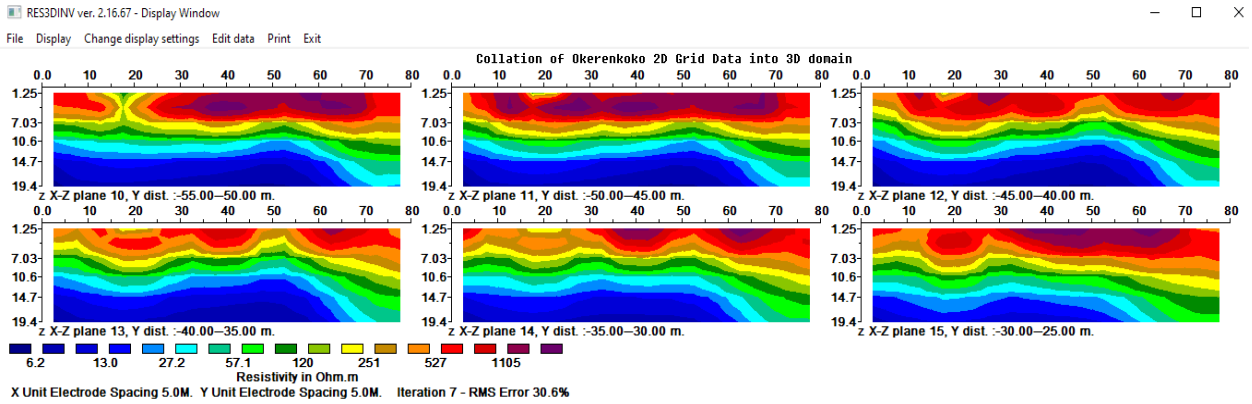

Figure 9b. 2-D vertical slices in the *x-z* plane (10 to 15 plane cells).

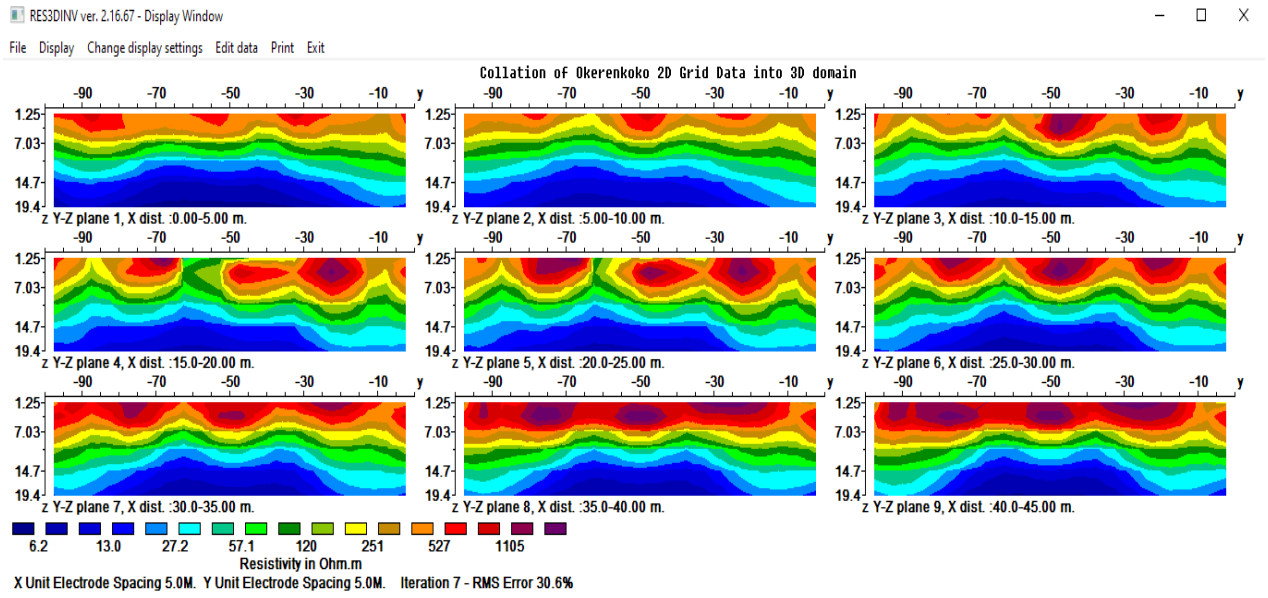

Figure 9c. 2-D vertical slices in the *y-z* plane (1 to 9 plane cells).

Table 3. Summary of number of blows and moisture/water content computed in soil samples-1.

No of Blows	Weight of Wet Sample	Weight of Dry Sample	Water content (%)
6	18.2578	14.8801	22.699
14	21.2831	17.8742	19.072
34	21.7296	19.0331	14.168

From the plot of moisture content against the number of blows for soil sample-1 (**Figure 10**), the moisture content corresponding to 25 blows on the logarithmic axis is the liquid limit, which was read approximately as 13%. Thus, the liquid limit ≈ 13% (**Figure 10**).

The plastic limit was approximated as the average moisture content from **Table 3** which in sample-1 is 18.646.

From the plot of moisture content against the number of blows for soil sample-2 (**Figure 11**), the moisture content corresponding to 25 blows on the logarithmic axis is the liquid limit, which was read approximately 17%. Thus, the liquid limit ≈ 17% (**Figure 11**).

The plastic limit was approximated as the average moisture content from **Table 4** which in sample-2 is 17.130.

From the plot of moisture content against the number of blows for soil sample-3 (**Figure 12**), the moisture content corresponding to 25 blows on the logarithmic axis is the liquid limit, which was read approximately as 13%. Thus, the liquid limit ≈ 13% (**Figure 12**).

The plastic limit was approximated as the average moisture content from **Table 5** which in sample-3 is 13.147.

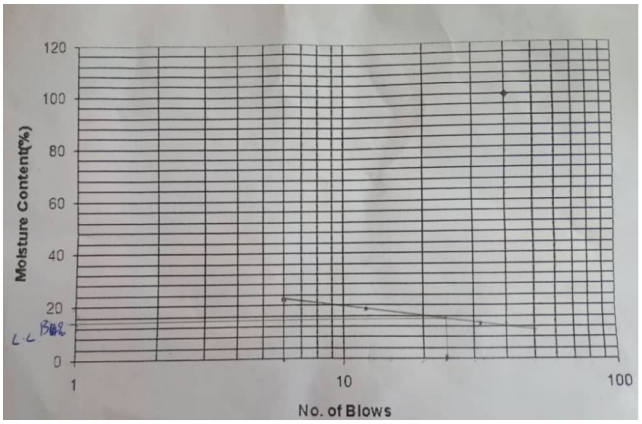

Figure 10. Plot of moisture content (%) against number of blows for liquid limit determination in soil sample-1.

Table 4. Summary of number of blows and moisture/water content computed in soil samples-2.

Weight of Container Wo (g)	No of Blows	Weight of Container + Wet Sample W1 (g)	Weight of Wet Sample (g) W1 – W0	Weight of Container + dry Sample W2 (g)	Weight of dry Sample (g) W2 – W0	Moisture content (%)
49.97	13	71.103	21.133	67.57	17.60	20.07
56.184	23	77.136	20.952	74.11	17.926	16.88
67.54	54	89.605	22.065	86.82	19.28	14.45

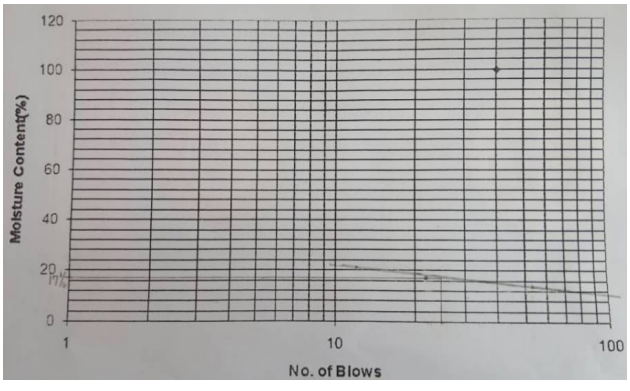

Figure 11. Plot of moisture content (%) against number of blows for liquid limit determination in soil sample-2.

Table 5. Summary of number of blows and moisture/water content computed in soil samples-3.

No of Blows	Weight of Wet Sample	Weight of Dry Sample	Water content (%)
18	15.81	13.597	16.2756
23	26.18	23.07	13.4807
30	23.33	21.27	9.6850

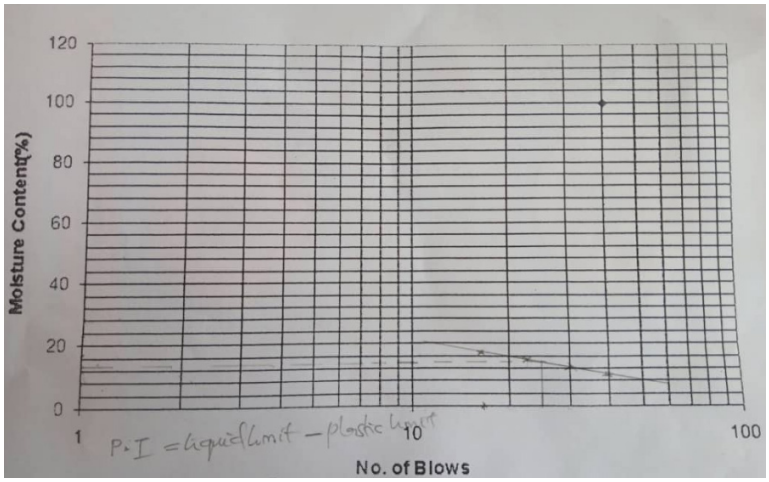

Figure 12. Plot of moisture content (%) against number of blows for liquid limit determination in soil sample-3.

The plasticity index (**Ip**) which is the range of water content over which the soil remains in the plastic state, was evaluated for each sample using the relation in Equation (2) recalled as: I_p=*LL-PL*.

For sample-1: Plasticity index (**Ip**) = 13 – 18.646
= –5.646 ≈ 0 (zero)

For sample-2: Plasticity index (**Ip**) = 17 – 17.13
= –0.130 ≈ 0 (zero)

For sample-3: Plasticity index (**Ip**) = 13 – 13.147
= –0.147 ≈ 0 (zero)

The plasticity index parameter (**Ip**) cannot be negative if the plastic limit, in some exceptions is greater than the liquid limit, as observed in soil samples-1, 2, and 3. In this case, it is considered to be zero and the soil is considered non-plastic (**Table 1**), which is symbolic of sandy soil [43,44]. The plasticity of soil is its tendency to undergo deformation without cracking. It is an important index property of fine-grained soil, especially clayey soils. The adsorbed water bounded in clayey soil leads to the plasticity of the soil [44].

In this study, the soil samples were collected within the first 8.0 m of each borehole. At this depth, the soil samples were predominantly composed of sandy soil as delineated from results of 2-D and 3-D tomography where the subsurface geology from the top-soil to the first 8.0 m consists of sandy soil with varying degrees of saturation i.e. dry sand and wet sand. The clayey soil became more evident from depths beyond 8.0 m in the study area. Therefore, the soil samples analyzed were representatives of sandy soil, and this validates the results of the liquid limit, plastic limit and plasticity index obtained from the soil samples. Sandy soils do not possess any plasticity and their plasticity index is usually assumed to be zero. These findings apparently justify the subsoil conditions defined in the interpretation of the 1-D VES survey and 2-D and 3-D geoelectrical resistivity imaging.

5. Conclusions

2-D and 3-D geoelectrical resistivity imaging supported with geotechnical-soil analysis has been successfully used in evaluating subsoil properties for engineering site investigation at Okerenkoko primary school, in Warri-southwest area of Delta State, to adduce the phenomena responsible for the structural failure observed in the school buildings. The dataset consists of an orthogonal set of ten (10) 2-D geoelec-

trical resistivity lines obtained with the Wenner array and taken as the data density needed for a reliable geophysical-geotechnical exploration study. The dataset was analyzed using the Earth Imager Inversion program and Res3DInv software. The results brought to light the geological structure beneath the subsurface, which consists of four geoelectric layers identified as topsoil, dry/lithified upper sandy layer, wet sand (water-saturated) and peat/clay/sandy clayey soil (highly water-saturated). The profoundly-seated peat/clay materials ($\rho \leq 20$ Ωm) were delineated in the study site to depths of 17.1 m and 19.8 m from 2-D and 3-D tomography respectively. The dominance of mechanically unstable peat/clay/sandy clay layers beneath the subsurface which are highly mobile in response to volumetric changes is responsible for the visible cracks/failure/subsidence observed on structures within the study site. The DC resistivity outcome was validated using the geotechnical study of soil specimens collected from drill holes covering the first 8.0 m on three of the profiles. The consistency limits of the soil samples revealed plasticity indices of zero for all samples. Soil samples within the depth analyzed are therefore representative of sandy soils lacking plasticity and are assumed to have a plasticity index of zero. These findings seem to justify subsurface conditions defined in the interpretation of 2-D and 3-D geoelectric resistivity imaging. In this study, generating a 3D dataset by matching a set of orthogonal or parallel 2D lines improves the speed of field processing, reduces the cost of field logistics and is relevant to obtaining 3D datasets using square or rectangular grid methods. Both 2-D and 3-D resistivity tomography results agreed with each other. 3-D images displayed as horizontal depth slices and the 3-D subsurface volume which were realized in the study, revealed the dominance of very low resistivity materials i.e. peat/clay/sandy clay within the fourth, fifth and sixth layers at depths ranging from 8.68-12.5 m, 12.5-16.9 m and 16.9-21.9 m respectively. Thus, the 3-D inversion model has improved the accuracy level of geoelectrical resistivity imaging, as false elements due to 3-D effects commonly comparable with 2-D inversion images have been reduced in the 3-D inversion images. The research supports near-surface surveys with specific maximum investigation depths of 17.1 m, 19.8 m and 21.9 m for 2-D and 3-D imaging, respectively. The methods employed in this study justifiably provided relevant information on the subsurface geology beneath the study site and its suitability for engineering practice. It is therefore highly recommended to use these methods as important tools for engineering site assessment projects and groundwater inherent investigations.

Conflicts of Interest

We declare that this research work has never been submitted previously by anyone to any journal for peer review and publication; hence it is an original work. All the ethical principles of research in the data collection, preparation, analysis and interpretation were implemented.

Availability of Data and Material

Applicable and available on demand from the corresponding author.

Funding

There was no grant or financial support provided from any agency in the public, commercial and not-for profit organization for this research work.

Acknowledgement

The authors profoundly acknowledge the good people of Okerenkoko community for allowing us carry out the geophysical survey used for this study within the primary school premises, and to the Federal University of Petroleum Resources, Effurun, Nigeria for the use of her laboratory and computing facilities.

References

[1] Igwe, O., Umbugadu, A.A., 2020. Characterization of structural failures founded on soils in Panyam and some parts of Mangu, Central Ni-

geria. Geoenvironmental Disasters. 7(7), 1-26. DOI: https://doi.org/10.1186/s40677-020-0141-9

[2] Caleb, A.T., Gabriel, I.O., 2012. Geopysical and geotechnical investigation of cham failed dam project, in Nigeria. Research Journal of Recent Sciences. 1(2), 1-18.

[3] Premium Times newspaper Journalism Report in Nigeria, 2021 [Internet]. Available from: https://www.premiumtimesng.com/news/505583-ikoyi-building-collapse

[4] Chendo, I.G., Obi, N.I., 2015. Building collapse in Nigeria: The causes, effects, consequences and remedies. International Journal of Civil Engineering, Construction and Estate Management. 3(4), 41-49.

[5] Akintorinwa, O.J., Adesoji, J.I., 2009. Application of geophysical and geotechnical investigations in engineering site evaluation. International Journal of Physical Sciences. 4(8), 443-454.

[6] Ayolabi, E.A., Enoh, I.J.E., Folorunso, A.F., 2013. Engineering site characterisation using 2-D and 3-D electrical resistivity tomography. Earth Science Research. 2(1). DOI: https://doi.org/10.5539/esr.v2n1p133

[7] Ozegin, K.O., Oseghale, A.O., Audu A.L., et al., 2013. An application of the 2-D D.C. Resistivity method in building site investigation—A case study: Southsouth Nigeria. Journal of Environment and Earth Science (JEES). 3(2).

[8] Loke, M., Chambers, J., Rucker, D., et al., 2013. Recent developments in the direct-current geoelectrical imaging method. Journal of Applied Geophysics. 95, 135-156. DOI: https://doi.org/10.1016/j.jappgeo.2013.02.017

[9] Eze, S.U., Abolarin, M.O., Ozegin, K.O., et al., 2021. Numerical modeling of 2-D and 3-D geoelectrical resistivity data for engineering site investigation and groundwater flow direction study in a sedimentary terrain. Modeling Earth Systems and Environment. 8(1). DOI: https://doi.org/10.1007/s40808-021-01325-y

[10] Aizebeokhai, A.P., Olayinka, A.I., Singh, V.S., 2010. Application of 2D and 3D geoelectrical resistivity imaging for engineering site investigation in a crystalline basement terrain, southwestern Nigeria. Environmental Earth Sciences. 61(7), 1481-1492.

[11] Chambers, J.E., Ogilvy, R.D., Kuras, O., et al., 2002. 3D electrical imaging of known targets at a controlled environmental test site. Environmental Geology. 41(6), 690-704. DOI: https://doi.org/10.1007/s00254-001-0452-4

[12] Bentley, L.R., Gharibi, M., 2004. Two- and three-dimensional electrical resistivity imaging at a heterogeneous remediation site. Geophysics. 69(3), 674-680. DOI: https://doi.org/10.1190/1.1759453

[13] Aizebeokhai, A.P., 2010. 2D and 3D geoelectrical resistivity imaging: Theory and field design. Scientific Research & Essays. 5(23), 3592-3605.

[14] Fargier, Y., Lopes, S.P., Fauchard, C., et al., 2014. DC electricaresistivity imaging for embankment dike investigation: A 3d extended normalization approach. Journal of Applied Geophysics. 103, 245-256. DOI: https://doi.org/10.1016/j.jappgeo.2014.02.007

[15] Hung, Y.C., Lin, C.P., Lee, C.T., et al., 2019. 3D and boundary effects on 2D electrical resistivity tomography. Applied Sciences. 9, 2963. DOI: https://doi.org/10.3390/app915296

[16] Loke, M.H., 2000. Electrical imaging surveys for environmental and engineering studies: A practical guide to 2D and 3D surveys. Technical Reports. 59.

[17] Boscardin, M.D., Cording, E.J., 1989. Building response to excavation-induced settlement. Journal of Geotechnical Engineering, ASCE. 115(1), 1-21.

[18] Nigeria Geological Survey Agency, 2004. "The Geological Map of Nigeria", A Publication of Nigeria Geological Survey Agency, Abuja.

[19] Asseez, O.L., 1989. Review of the stratigraphy,

sedimentation and structure of the Niger Delta. Geology of Nigeria. Rock View (Nigeria) Ltd., Jos: Nigeria. pp. 311-324.

[20] Reyment, R.A., 1965. Aspects of the geology of Nigeria. University of Ibadan Press: Ibadan. pp. 132.

[21] Short, K.C., Stauble, A.J., 1967. Outline of the geology of Niger Delta. AAPG Bulletin. 51, 761-779.

[22] Doust, H., Omatsola, E., 1990. Divergent/passive margin basins. American Association of Petroleum Geologists: Tulsa. pp. 239-248.

[23] Kulke, H., 1995. Regional petroleum geology of the World, Part II, Africa, America, Australia and Antarctica. Gebruder Borntraeger: Berlin. pp. 143-172.

[24] Merki, P.J., 1970. Structural geology of the Cenozoic Niger Delta. University of Ibadan Press: Ibadan. pp. 251-268.

[25] Akuijeze, C.N., Ohaji, S.M.O., 1989. Iron in Borehole water in Bendel State, Nigeria Association of Hydrogeologist. p. 4011. No.2.

[26] Uchegbulam, O., Ayolabi, E.A., 2014. Application of electrical resistivity imaging in investigating groundwater pollution in Sapele area, Nigeria. Journal of Water Resource and Protection. 6, 1369-1379.

[27] Loke, M.H., 2001. Electrical Imaging Surveys for Environmental and Engineering Studies: A practical guide to 2D and 3D surveys. 62 [Internet]. Available from: http://www.geoelectrical.com

[28] Vander Velpen, B.P.A., 2004. WinRESIST Version 1.0. resistivity sounding interpretation software. M.Sc. Research Project, ITC, Limited: Netherland.

[29] Patra, H.P., Nath, S.K., 1999. Schlumberger geoelectric sounding in groundwater (principle, interpretation and application). M/s A.A Balkema, Rotterdam: Netherlands.

[30] Bankole, S.A., Olasehinde, P.I., Ologe, O., et al., 2014. Geological and electrical resistivity sounding of olokonla area in north-central Nigeria. Nigerian Journal of Technological Development. 11(1).

[31] Loke, M.H., Baker, R.D., 1996. Practical techniques for 3D resistivity surveys and data inversion. Geophysical Prospecting. 44, 499-523.

[32] Sasaki, Y., 1992. Resolution of resistivity tomography inferred from numerical simulation. Geophysical Prospecting. 40, 453-464.

[33] Eze, S.U., Orji, O.M., Onoriode, A.E., et al., 2022. Integrated geoelectrical resistivity method for environmental assessment of landfill leachate pollution and aquifer vulnerability studies. Journal of Geoscience and Environment Protection. 10, 1-26.
DOI: https://doi.org/10.4236/gep.2022.109001

[34] Sudha, K., Israil, M., Mittal, S., et al., 2009. Soil characterization using electrical resistivity tomography and geotechnical investigations. Journal of Applied Geophysics. 67, 74-79.
DOI: https://doi.org/10.1016/j.jappgeo.2008.09.012

[35] Jamal, H., 2020. Atterberg Limits Soil Classification—Liquid Limit, Plastic Limit, Shrinkage [Internet] [cited 2022 Dec 26]. Available from: www.aboutcivil.org

[36] Seed, H.B., Woodward, R.J., Lundgren, R., 1967. Fundamental aspects of the atterberg limits. Journal of Soil Mechanics and Foundations Division. 92(SM4), 63-64.
DOI: https://doi.org/10.1061/JSFEAQ.0000685

[37] Skempton, A.W., 1953. The colloidal activity of clay. Proceedings of the Third International Conference of Soil Mechanics and Foundation Engineering. 1, 57-61.

[38] British Standard (BS) 1377., 1990. Method of testing soil for civil engineering purposes. British Standard Institute: London.

[39] Burmister, S.V., 1997. Advanced soil mechanics (2nd edition). Wiley and Sons: New York.

[40] Nwankwoala, H.O., Amadi, A.N., Ushie, F.A., et al., 2014. Determination of subsurface geo-

technical properties for foundation design and construction in Akenfa Community, Bayelsa State, Nigeria. American Journal of Civil Engineering and Architecture. 2(4), 130-135.
DOI: https://doi.org/10.12691/ajcea-2-4-2

[41] Archie, G.E., 1942. The electrical resistivity log as an aid to determining some reservoir characteristics. Transaction of American Institute of Mining, Metallurgical, and Petroleum Engineers. 146(1), 389-409.

[42] Reynolds, J.M., 1997. An introduction to applied and environmental geophysics. John Wiley and Sons Ltd: Chichester. p. 778.

[43] Sowers, N., 1979. Introductory soil mechanics and foundations: Geotechnical engineering (4th Ed). Macmillan: New York.

[44] Das, B.M., 2006. Principles of geotechnical engineering. Thomson Learning College: Stamford.

BILINGUAL PUBLISHING GROUP

Advances in Geological and Geotechnical Engineering Research

https://journals.bilpubgroup.com/index.php/agger

ARTICLE

Petrology and Geochemical Features of Crystalline Rocks in Ora-Ekiti, Southwestern Nigeria

O.A. OlaOlorun**, *O.O. Akinola*, *A.O. Oyinloye

Department of Geology, Ekiti State University, P.M.B. 5363, Ado-Ekiti, Nigeria

ABSTRACT

This research investigates and reports on the petrology and geochemical characteristics of crystalline basement rocks in Ora-Ekiti, Southwestern Nigeria. Exhaustive geological investigation reveals migmatite, banded gneiss, granite gneiss and biotite gneiss underlie the area. In reducing order of abundance, petrographic examination reveals that migmatite contains quartz, muscovite and opaque minerals. Banded geniuses contain quartz, biotite, plagioclase, and opaque minerals. Granite geniuses contain quartz, plagioclase, biotite, microcline and opaque; while biotite geniuses contain biotite, plagioclase, opaque minerals, and quartz. Silica contents in migmatite (69.50%-72.66%; ca. 71.23%), banded gneiss (71.66%-77.1%; ca. 75.23%), biotite gneiss (72.32%-76.18%; ca. 73.83%) and granite gneiss (69.82%-73.15%; ca. 71.95%) indicate the rocks are siliceous. High alumina contents in migmatite (12.18%), banded gneiss (10.28%), biotite gneiss (11.46%) and granite gneiss (9.97%) are comparable to similar rocks in the basement complex. All the rocks show Ba, Sr and Rb enrichment. Harker diagrams of Al_2O_3 versus SiO_2 and CaO versus SiO_2 show negative trends while Na_2O versus SiO_2, K_2O versus SiO_2 and TiO_2 versus SiO_2 plots showed positive trends. This variation probably depicts extensive crystal fractionation in the magmatic systems that produced the rocks prior to metamorphism or partial melting of the precursor rock. SiO_2 versus ($Na_2O + K_2O$) classifies the rocks as granite to granodiorite. The rocks are high K-calc-alkaline and calc-alkalic on SiO_2-K_2O plot. This shows the rocks are potassic meaning that they are formed from a potassium-rich source. The plot of $Al_2O_3/(Na_2O + K_2O)$ versus $Al_2O_3/(CaO + Na_2O + K_2O)$ reveals the crystalline rocks are orogenic and originated from granitoid with meta luminous affinity. The rocks consist of gneisses of no economic minerals, but the petrology reveals them as common rocks typical of metamorphic terrains and geochemical features of the rocks reveal they are felsic and of granitic composition.

Keywords: Ora-Ekiti; Crystalline basement rocks; Petrology; Metaluminous affinity

*CORRESPONDING AUTHOR:

O.A. OlaOlorun, Department of Geology, Ekiti State University, P.M.B. 5363, Ado-Ekiti, Nigeria; Email: olusola.ola-olorun@eksu.edu.ng

ARTICLE INFO

Received: 22 November 2022 | Revised: 11 March 2023 | Accepted: 16 March 2023 | Published Online: 6 April 2023

DOI: https://doi.org/10.30564/agger.v5i2.5243

CITATION

OlaOlorun, O.A., Akinola, O.O., Oyinloye, A.O., 2023. Petrology and Geochemical Features of Crystalline Rocks in Ora-Ekiti, Southwestern Nigeria. Advances in Geological and Geotechnical Engineering Research. 5(2): 24-37. DOI: https://doi.org/10.30564/agger.v5i2.5243

1. Introduction

The study area lies within the basement complex of southwestern Nigeria (**Figure 1**) and its regional geology has been described in segments by different authors. Rahaman [1] noted that southwestern Nigeria as part of the extensive basement terrain contains crystalline rocks of heterogeneous lithologies and complex structural features. The segment of this basement that falls within Ekiti State contains the migmatite gneiss complex, the Schist belts, and Pan-African granites. Researchers [2,3] confirmed that on a regional scale, older tectonic imprints associated with the rocks in this domain are grossly overprinted by newer ones. The study area consists of rocks that are typical of Precambrian terrain in Nigeria. The main lithologic units in Ora-Ekiti have been generally categorized as undifferentiated migmatite basements by the Geological Survey of Nigeria [4]. However, in the current study, detailed geological mapping revealed four main lithologies. These are migmatite, banded gneiss, biotite gneiss and granite gneiss (**Figure 2**).

1.1 Migmatite

Migmatite covers the northern part of the study area and extends towards the west underlining most of the newly developing areas of the town along Ido-Ekiti Road. This rock unit has been described as similar to those in and Ado-Ekiti [5]. Migmatite in the study area consists of gneissic (mafic) and granitic (felsic) components (**Figure 3a**). It is a coarse-grained composite rock comprising granitic components (dominantly quartz + feldspar ± muscovite) (leucosome) and gneissic components (biotite + hornblende ± magnetite) which constitute the melanosome. In many parts of Nigeria's basement, migmatite forms the country rock. The structural attribute of Ora-Ekiti migmatite includes strong axial plane foliations and folds which show copious evidence of shearing. Structures such as joints, foliations, lineation, folds, quartz veins, pegmatitic, aplitic and dolerite dykes were also observed on many outcrops. This rock is poorly banded which makes it structurally distinct.

1.2 Banded gneiss

This gneiss is unique for its conspicuous bands which form lenses of varying mineralogical composition. Banded gneiss outcrops in Ora-Ekiti occur as residual hills with elevation which ranges between 535-575 m. A typical example occurs around Eliju where the rock has fine grain texture. Some of these bands (or lenses) contain granular minerals that are bound together in interlocking textures. The most distinct feature of the rock is compositional banding which depends largely on the interlaying of minerals having various colors. Dark and light bands alternate due to the segregation of mafic and felsic minerals (**Figure 3b**). Banding also arises from sorting differing grain sizes of the same minerals. Sometimes, the bands are distributed into beadlike structures resembling pinch and swell or boudins.

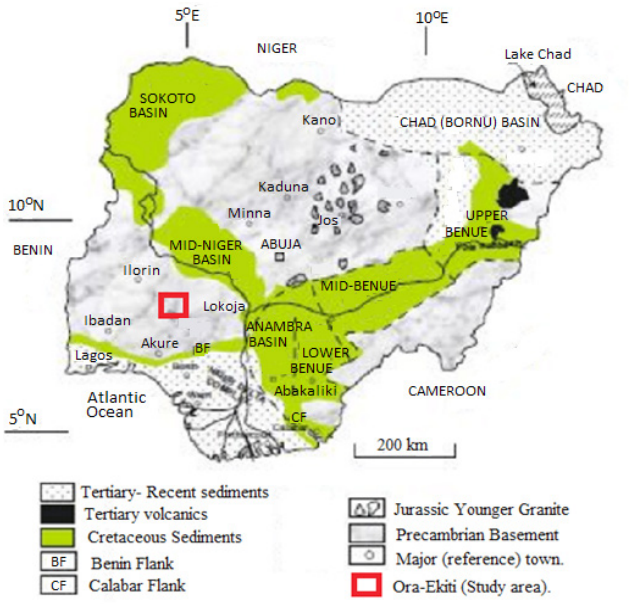

Figure 1. Geological map of Nigeria showing location of the study area within the Precambrian Basement of Southwestern Nigeria (Modified after [6])

1.3 Biotite gneiss

Biotite gneiss in Ora-Ekiti occupies the southern segment of the study area. It is highly foliated with darkish tints imposed by biotite impregnations

alongside felsic minerals including quartz and feldspar. Biotite gneiss occupies both sides of Aye-Ora Road. It is medium to coarse-grained foliated with a preponderance of biotite blades and acicular chlorite minerals (**Figure 3c**). The outcrops contain overwhelming evidence of pegmatite dykes and secondary structures like fold, joints, quartz veins, which sometimes crosscut each other in some locations, and exfoliations. Biotite-gneiss in Ora-Ekiti occurs as a rock with low altitude masses.

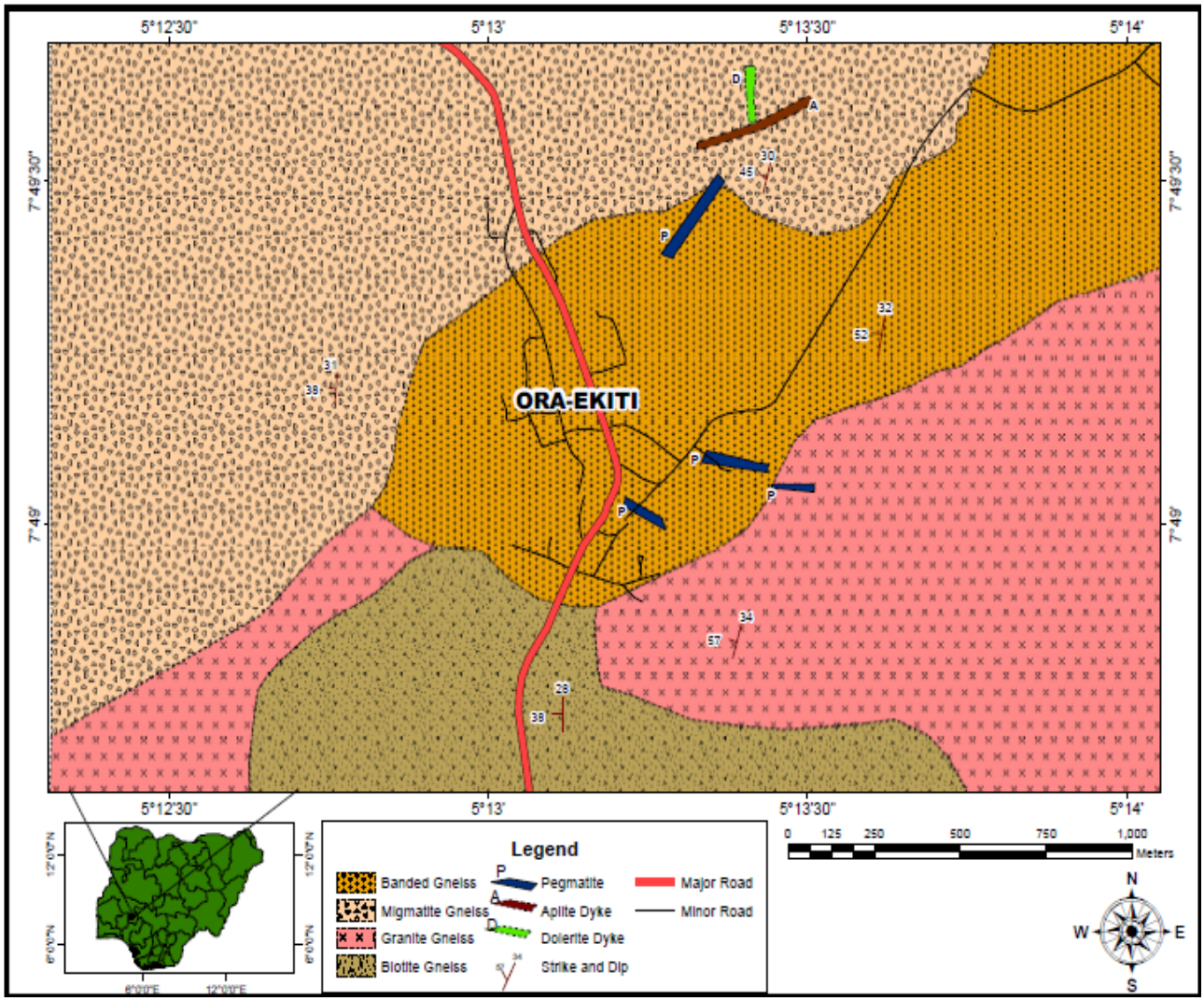

Figure 2. Geological map of Ora-Ekiti.

1.4 Granite gneiss

Granite gneiss in the study area occupies the eastern and southwestern corners of the study area. It is a felsic rock (granitic) that has suffered metamorphism, the rock has changed in mineralogy and texture through the action of intense heat and pressure but still retains its granitic nature. Granitic gneiss has a mineralogical composition similar to that of granite except that it now shows evidence of metamorphic recrystallization such as translational fabrics and decussate textures. Some outcrops exhibit tortuous veins and ptygmatic folds (**Figure 3d**). Granite gneiss in the study area is a coarse-grained rock composed mostly of quartz, alkali feldspar and plagioclase and a few phyllosilicate minerals largely represented by biotite. Granite gneiss outcrops in Ora-Ekiti are extensive but of average height. Typical of this unit is an outcrop behind the King's palace in Ora-Ekiti. The grain size of granite gneiss is finer

than the migmatite.

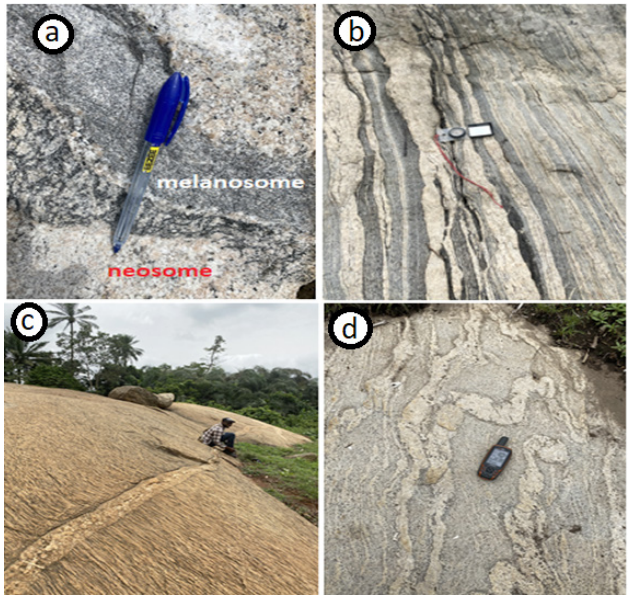

Figure 3. (a) Migmatite from Oke-Iyila area of Ora-Ekiti exhibiting melanosome (dark) and neosome (light) portions. (b) Banded-gneiss from Ora-Ekiti with mineralogical banding. Mafic (ferromagnesian) and light-colored (quartzo-feldspartic) minerals components are parallel to each other (c) Biotite-gneiss outcrop intruded by a pegmatite dyke at Ori Oke-Aanu along Aaye road, Ora-Ekiti, (d) Granite-gneiss from Ora-Ekiti showing quartz veins that are distorted and folded.

2. Geological setting

Ekiti State, which is one of the six states that constitute southwestern Nigeria, is entirely underlain by crystalline rocks of igneous and metamorphic origin. A literature search reveals geological investigation on Ora-Ekiti and the environment is very scanty. However, a few geological investigations have been undertaken around Ado-Ekiti and Ijero-Ekiti which lies 25 km SE and 25 km northwest of Ora-Ekiti respectively. The entire region represents the reactivated domain that resulted from the collision between a passive continental margin of the West African craton and the active Pharusian continental margin [7,8]. The basement has been reworked by cycles of orogeneses resulting in widespread deformation, metamorphism and remobilization during the Liberian (2,700 Ma), the Eburnean (2000 Ma), the Kibarian (1,100 Ma), and Pan-African (600 Ma). The last episode was characterized by widespread deformation, regional metamorphism, migmatisation, granitization and gneissification processes which produce syn-tectonic granites and gneisses [9]. The emplacement of late tectonic granites, granodiorites and dykes represent the final stages of the Pan-African orogeny. The end of the orogenic phase was marked by faulting and fracturing [10,11]. Migmatite is the most extensive unit in the basement of Ekiti State. It is an aggregation of migmatite, nebulitic and stromatolitic migmatite, orthogneisses, paragneiss and other varieties such as augen gneiss and calc-gneiss. The Pan-African tectonic-thermal activities were largely responsible for the recrystallization and reworking of the basement rocks. Migmatite unit belongs to upper amphibolite facies metamorphism and has ages ranging from Archean to Proterozoic in Nigeria [1,8]. The unit constitutes about 75% of the surface area of Ekiti State and about 30% of the total, some of surface area of Nigeria. Migmatite covers a substantial part of the eastern segment of Ekiti State. Quartzite unit occurs towards the western corner of the state covering Effon-Alaye, Okemesi and Ogotun area. In literature, this lithologic unit has been referred to as Effon Psammite [12]. Even though some quartzite units occur around Ado-Ekiti, they are not mappable at the scale of the geologic map.

The schist belts are Proterozoic supra crustal rocks that have been in-folded into the migmatite gneiss-quartzite complex. It contains coarse to fine-grained clastic rocks, pelitic schist, phyllite, banded iron formation, carbonate rocks (marble/dolomite) and meta-igneous rocks (amphibolite). Other authors believed the schist belts are fragments of ocean floor material from small back-arc basins. The Ife-Ilesha schist belt extends into the northwestern corner of Ekiti State (**Figure 4**) covering Ijero, Odo-Owa and Ipoti-Ekiti. Falconer [13], distinguished a group of concordant/semi-concordant deeply rooted granite within the basement complex which he called Older Granite. This granite type is distinct from the high-level, discordant, tin-bearing granites of Northern Nigeria which he referred to as Younger Granite. The Older granites are pre-tectonic, syn-tectonic and post-tectonic rocks that intruded both the migmatite gneiss complex and schist belts. The granite range between 750-450 Ma in age and some authors referred to them as Pan-African gran-

ite. The rock unit varies in composition from tonalite to granodiorite to adamellite and true granites, and it represents the magmatic cycle of the Pan-African orogeny. Charnockite forms an important rock group emplaced during this period and is anatectic in origin [14]. The use of the term Pan African Granitoid for the older granites not only on the merit of age and not being available at the time they were named older granites is contended [8], but opined that it should be used because it covers several important petrologic groups formed at the same time. Older granite occurs together with charnockite along a narrow strip around Ikere-Ekiti and Ado Ekiti while a few outcrops dotted Ilupeju and Ayede areas in the north-central part of the state.

3. Materials and methods

The methodological approach adopted includes systematic geologic mapping and sampling of rocks. The method includes fieldwork, sampling, and laboratory procedures.

3.1 Fieldwork and sampling

The fieldwork essentially entails geologic mapping, identification, and description of outcrop exposures. It also involves describing their structural features. A thorough and careful traversing of the study area was done on foot with a hand-held Global Positioning System (GPS) following the major roads, minor roads, and bush paths. Traverses are made to outcrops that are not assessable through these roads. The area is divided into grids, each of which is mapped separately, and grid-controlled sampling was adopted. Useful information about the names of localities where good outcrops were found was made possible by people in the host communities.

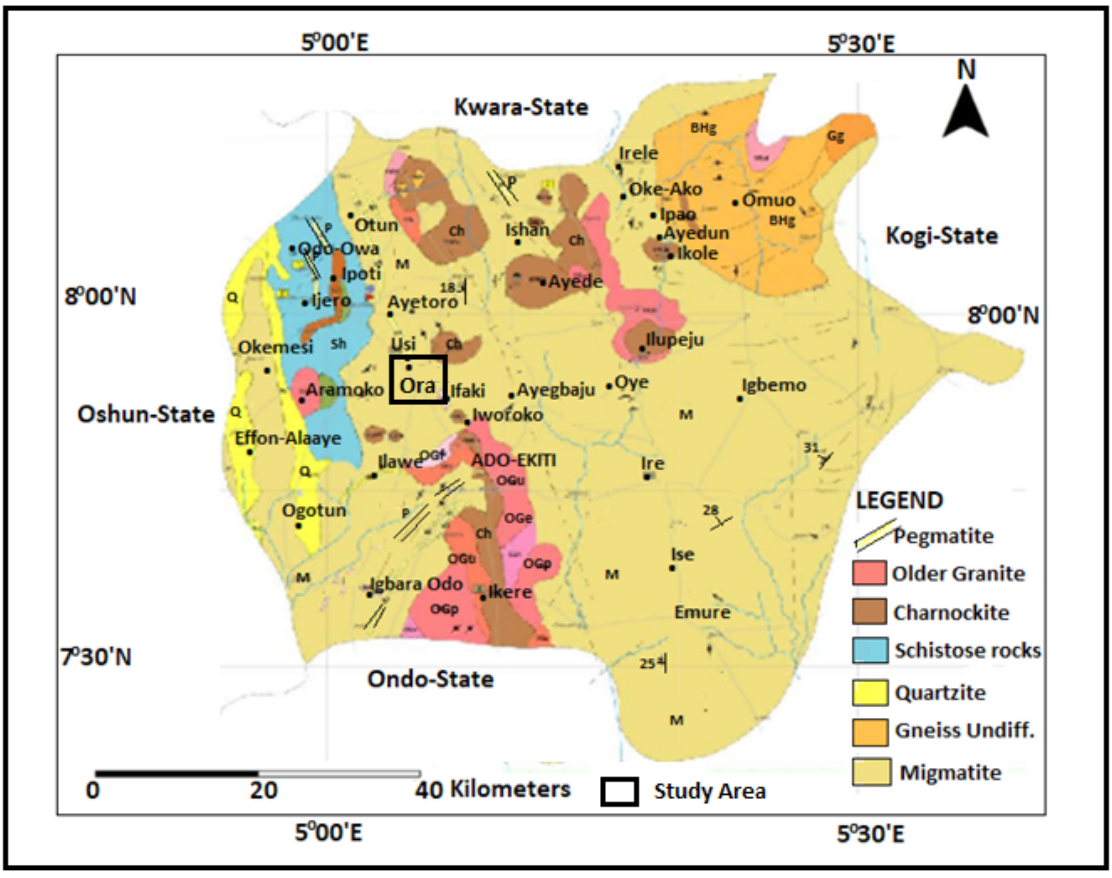

Figure 4. Geological map of Ekiti State and the location of the study area (after NGSA [14]).

In this study, only fresh samples are considered for analysis and are safely put in sample bags. It was observed during the field exercise that the lithological boundaries do not have clear-cut demarcations but grade into each other. Photographs of the rocks *in situ* positions were captured using a (Nikkon Coolpix L80) digital camera. Twenty samples of each of the four rock types were collected during fieldwork. Fresh samples with sizes ranging between 4-5 kg were hewed from rock exposures using a sledgehammer. The rock samples are kept in sample bags and labeled. The points where the samples were obtained in the field were translated into the corresponding positions on the topographic base map. This procedure was repeated at each location, strike and dip values were indicated as appropriate. The sample locations are Oke-Iyila, Olokowu, Oke-IIekan and opposite Ora Community High School among others.

3.2 Laboratory procedures

Samples collected are subjected to laboratory procedures to determine the petrology of the basement rocks, the mineralogical composition and microstructures which help to confirm the rock's name as well as the metamorphic grade are noted. In addition to outcrop examinations, the petrographic study was based on a visual examination of thin sections.

Preparation of thin section

After reducing the samples to the desired size (2 cm × 1 cm × 0.5 cm) using a cutting machine, the smooth surface of the rocks was glued to a glass slide and ground down on the lapping machine. Silicon carbide was put on the lapping glass which was placed on the lapping table with some water and the equipment was activated and observed until the surface becomes very smooth. After lapping, the rock specimen was washed with water and mounted on a thermo plate switched to 120 °C for an hour to remove excess water from the specimen. This baking process is important as it prevents excess bubbles from appearing on the slide. Thereafter, the specimen was removed from the hot plate and allowed to cool down to room temperature. The specimen was later mounted into a prepared glass slide by using araldite and taken to the cutting machine for size reduction. The reduced specimen was taken to the lapping machine via lapping jig for final reduction to the required thickness of 0.5 mm which is the standard thin section thickness. Once the thickness is achieved the specimen is then removed and washed properly to remove excess slurry around it. After washing, the specimen is allowed to dry and then covered with glass slips using Canada balsam and washed with methylated spirit (or acetone) and detergent. The specimen was then rinsed with water and allowed to dry in the air and then labeled accordingly for microscopic analysis.

Petrography

For petrographic investigation, thin sections of the rock samples were prepared. The slides were examined under petrological microscopes.

Analytical procedure

Twelve fresh samples selected from those obtained from outcrop exposures during geological mapping were subjected to analytical procedures. Major elements (SiO_2, $A1_2O_3$, Fe_2O_3, MnO, MgO, CaO, K_2O, Na_2O, P_2O_5, and TiO_2) and trace elements (Nb, V, Cu, Ba, Ni, Rb, Sr and Zr, Mo, Ag, Ta, Pb and Th) analyses were conducted on X-ray Fluorescence equipment (Phillips PW 1404/10) and ICP-MS respectively. The analytical procedures were undertaken at the Bureau Veritas Laboratories, Vancouver, Canada. The accuracy of trace element analyses is within ± 5 parts per million (ppm) and major elements ± 0.5%. (Analytical procedure for the research followed [15]. Analytical results are presented in **Tables 1** and **2**.

4. Results

The results of this research are presented in the order: Petrography and geochemistry.

4.1 Petrography

Migmatite

Petrographic examination reveals Ora-Ekiti migmatite (in reducing order) contains quartz, muscovite, and opaque minerals (**Figure 5a**). Quartz being

the most abundant mineral reflects the siliceous nature of Ora-Ekiti migmatite. Quartz grains occur as a discretely clear mineral with a well-defined outline. It is well-distributed within the rock while in some slides it forms clustered aggregate. The preponderance of quartz in the rock may be attributed to remobilization during metamorphic recrystallization or high silica content attributable to late-stage magmatic crystallization in the precursor rock. Under plane-polarized light, muscovite has whitish colour but with a diagnostic bird-view appearance. It forms tabular crystals usually six-sided or is sometimes irregular in outline. Some plates form six-sided prisms elongated parallel to the c-axis. Opaque minerals are mainly iron oxide of irregular shapes.

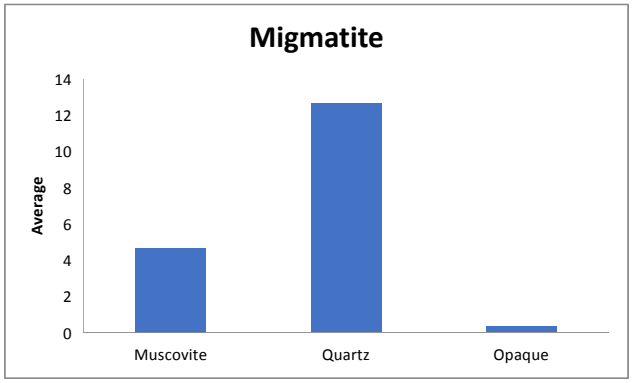

Figure 5a. A chart showing the average composition of the migmatite in the study area.

Banded gneiss

Petrological investigation reveals banded gneiss from the study area in order of reducing abundances contains quartz, biotite, plagioclase feldspar and opaque minerals (**Figure 5b**). That quartz is the most abundant mineral in all the slides is a reflection of the high degree of stability of the mineral and this may indicate that the rock is of acidic antecedent. The mineral quartz is colorless under the plane-polarized light, biotite shows grey to brown coloration with characteristic bird view structure and bladed appearance. Crystals of plagioclase are colorless in plane polarized light exhibiting first order grey color under cross polars.

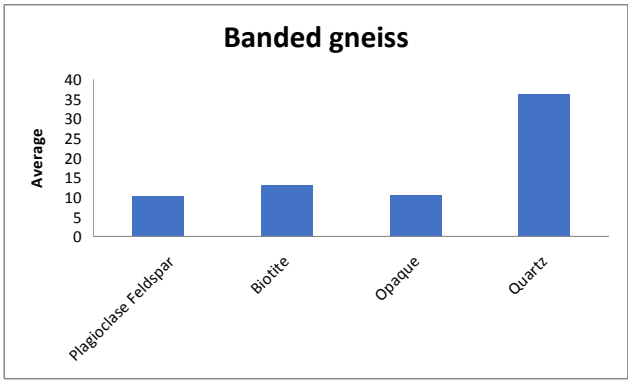

Figure 5b. A chart showing the average composition of banded gneiss in the study area.

Granite gneiss

Optical microscopy reveals Granite gneiss contains quartz, plagioclase feldspar, biotite, opaque minerals and microcline (**Figure 5c**). Quartz is the most abundant mineral in all the slides. Quartz is colorless under the plane-polarized light and subangular. Biotite shows a red to brown color with subhedral to anhedral habit. The crystals of plagioclase are colorless in plane-polarized light with weak birefringence. It can be distinguished from other types of feldspar by its polysynthetic twinning. Opaque minerals occur in subordinate amounts and are mainly magnetite.

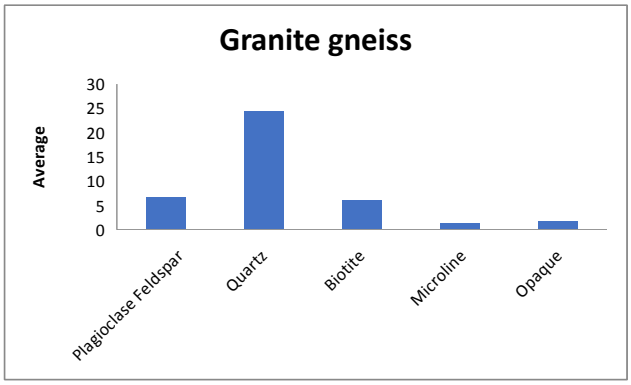

Figure 5c. A chart showing average composition of Granite gneiss.

Biotite gneiss

Biotite gneiss in Ora-Ekiti in the same order, contains biotite, plagioclase feldspar, opaque minerals and quartz (**Figure 5d**). Quartz occurs as clear mineral grains, few are however cloudy and fractured. Quartz is the least abundant mineral; it is made of

grains that have no cleavage or plane of weakness. Its presence in all the rocks may be consequent on quartz being one of the most stable minerals in siliceous igneous rocks. Many siliceous rocks when subjected to metamorphic transformation have abundant quartz. Biotite shows grey to brown coloration with subhedral to anhedral habits. The crystals of plagioclase are colorless in plane-polarized light but exhibit first-order grey color under cross polars.

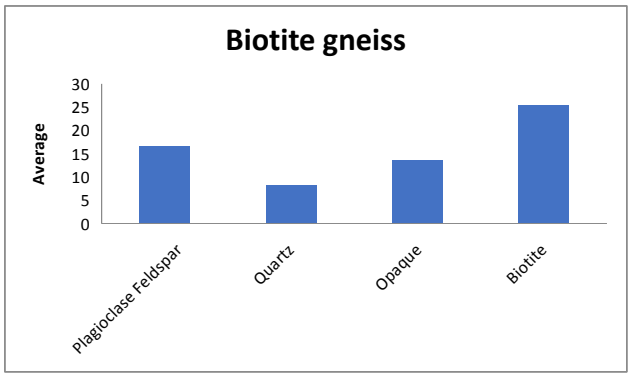

Figure 5d. A chart showing average mineralogical composition of Biotite gneiss in the study area.

4.2 Geochemistry

Results of the major chemical composition of rocks from Ora-Ekiti are presented (**Table 1**). From the analytical results, SiO_2 contents in migmatite range from 69.50%-72.66% with an average of 71.23%. Similarly, SiO_2 contents in banded gneiss (range: 71.66%-77.1%; ca. 75.23%), biotite gneiss (range: 72.32%-76.18%; ca. 73.83%) and granite gneiss (range: 69.82%-73.15%; ca. 71.95%) clearly indicate the crystalline rocks in Ora-Ekiti are siliceous. Average alumina contents in migmatite (12.18%), banded gneiss (10.28%), biotite gneiss (11.46%) and granite gneiss (9.97%) are high. The mean Fe_2O_3 contents in these rocks are 4.86%, 3.56%, 3.55% and 4.08% respectively. Average K_2O and Na_2O contents in migmatite (2.99%, 3.10%), banded gneiss (3.94%, 3.44%), biotite gneiss (4.09%, 3.28%) and granite gneiss (4.46%, 3.46%) falls within acceptable limits for this kind of rocks and makes them similar to granitoid. A number of schemes based on chemical composition have been applied in the classification and determination of the evolutionary trends and geotectonic setting of rocks in Ora-Ekiti. Harker variation plot of major oxides against SiO_2 and its correlation is useful for the prediction of post-magmatic phenomena that may be related to the rock's protolith. Binary plots of Al_2O_3 versus SiO_2 (**Figure 6a**) and, CaO versus SiO_2 (**Figure 6b**) reveal negative trends with increasing SiO_2. However, Na_2O *versus* SiO_2 (**Figure 6c**) and K_2O versus SiO_2 (**Figure 6d**) show positive trends with SiO_2 which indicates an increase in K_2O produces a corresponding increase in SiO_2 contents. Positive trends in K_2O and Na_2O may indicate albitization processes in the protolith prior to metamorphism or metasomatic alteration during metamorphic remobilization. The plot of TiO_2 versus SiO_2 (**Figure 6e**) also demonstrates a positive trend with SiO_2. Harker diagram of MgO versus SiO_2 (**Figure 6f**) reveals a negative trend symbolizing that as the major elements (anions) are taken from silicate melts, their quantities reduce with time. High alumina contents in the rocks might have resulted from a preponderance of aluminosilicates which forms the principal component of most rock-forming minerals like plagioclase, hornblende, and mica. These values are comparable to similar migmatite gneiss rocks in other parts of Nigeria. Substantial amounts of these oxides might have been contributed by ferromagnesian minerals like biotite, and hornblende and opaque minerals like magnetite. This range of value is comparable to those recorded for granitoid; this may equally indicate the rocks probably have granitic antecedents.

However, the positive correlation as indicated on K_2O versus SiO_2 and Na_2O versus SiO_2 (Harker diagrams, **Figure 6c** and **6d**), may imply the crystalline basement rocks may have the same progenitor (source materials) or similar pattern of mobility during metamorphism of the parent rock. The variation may also be indicative of extensive crystal fractionation or partial melting in the magma systems that produced the rocks. This is suggestive that the rocks emanated from the same parent magma. On the SiO_2 versus (Na_2O + K_2O) classification scheme of Middlemost [16] (**Figure 7**), the rocks plots are granitic

to granodioritic in composition. The AFM diagram (**Figure 8**, after Irvine and Baragar [17]) classified the rocks of Ora-Ekiti in *Calc-alkaline series*. Further chemical consideration on SiO_2-K_2O diagram (**Figure 9**, after Peccerillo and Taylor [18]), discriminate the rocks into *High-K Calcic-alkali* field.

The plots suggest the rocks are rich in potassium and may equally mean they are formed from potassium-rich rocks that are oxidized. The binary plot of the molecular ratio of alumina to alkalis of Al_2O_3/(Na_2O + K_2O) versus Al_2O_3/(CaO + Na_2O + K_2O) [i.e., A/NK versus A/CNK], of the crystalline rocks from Ora-Ekiti, (**Figure 10**, after Shands [19]) shows the rocks might have originated from a granite having peralkaline chemistry formed during the orogenic activity.

Trace element data (**Table 2**) shows enrichment in Ba, Sr, Rb and Zr while there is depletion in Cu, Nb, V, Ag and Th. With average Ba content of 1238 ppm in migmatite, 2087 ppm in banded gneiss, 2042 ppm in biotite gneiss and 1948 ppm in granite gneiss, these rocks are comparable to similar rocks in the basement complex areas of other parts of Nigeria. The anomalous enrichment in Ba, Sr, Rb and Zr is expected like in granites, and they are mostly concentrated in the upper continental crust of the earth. Low values recorded for Nb, Mo, Ag, Cd, and Pb are related to the geochemical behaviors of the elements as many of them are incompatible with lithophile elements. Hence they are of low concentration in crustal rocks.

Table 1. Analytical result of the basement rocks in Ora-Ekiti.

Oxides	**Migmatite**			**Banded gneiss**			**Biotite gneiss**			**Granite gneiss**		
	1	2	3	4	5	6	7	8	9	10	11	12
SiO_2	71.53	69.5	72.66	71.66	77.1	76.95	73.00	76.18	72.32	72.9	69.82	73.15
Al_2O_3	11.96	12.94	11.58	11.43	9.65	9.71	12.91	9.24	11.80	10.45	9.51	11.03
CaO	3.32	4.55	3.43	4.05	1.50	1.37	2.29	1.98	3.45	2.24	2.36	2.50
Fe_2O_3	5.09	5.36	4.13	4.45	3.2	3.04	2.66	4.19	3.8	5.42	3.61	3.22
K_2O	3.04	2.65	3.25	2.69	4.55	4.51	5.08	3.8	3.61	4.31	4.46	4.36
Na_2O	3.23	3.10	3.24	3.92	3.19	3.34	3.08	3.55	3.22	3.18	3.24	4.18
MgO	1.08	1.08	0.98	1.13	0.52	0.35	0.46	0.58	1.2	0.45	0.51	0.84
MnO	0.06	0.08	0.06	0.05	0.05	0.04	0.02	0.06	0.05	0.06	0.04	0.05
P_2O_5	0.07	0.07	0.06	0.14	0	0.03	0	0	0.06	0.16	0.04	0.07
TiO_2	0.61	0.63	0.34	0.56	0.24	0.43	0.23	0.35	0.44	0.61	0.46	0.38
Total	99.99	99.96	99.84	99.68	99.99	99.84	99.91	99.93	99.84	99.78	99.97	99.84

Table 2. Trace elements composition of the basement rocks in Ora-Ekiti.

Trace	**Migmatite**			**Banded gneiss**			**Biotite gneiss**			**Granite gneiss**		
	1	2	3	4	5	6	7	8	9	10	11	12
Nb	13	17	13	17	23	30	41	43	12	41	25	18
V	79	62	58	73	25	63	33	61	67	65	43	56
Cu	8	24	0	11	28	7	0	17	33	11	9	21
Rb	333	202	250	234	256	347	241	303	246	282	251	327
Sr	634	468	389	490	430	266	507	496	522	308	311	289
Zr	86	264	50	87	331	376	391	393	113	241	261	203

Table 2 continued

Trace	Migmatite			Banded gneiss			Biotite gneiss			Granite gneiss		
Mo	28	24	14	17	20	26	19	32	17	173	62	29
Ag	51	49	20	43	15	23	28	27	25	20	32	19
Ba	1647	1063	1005	1254	2663	2344	2426	2382	1318	2477	1863	1504
Ta	0	0	67	0	83	80	135	0	0	88	51	25
Pb	19	14	21	16	28	19	13	19	19	24	8	16
Th	43	0	0	0	40	0	47	0	29	26	38	49

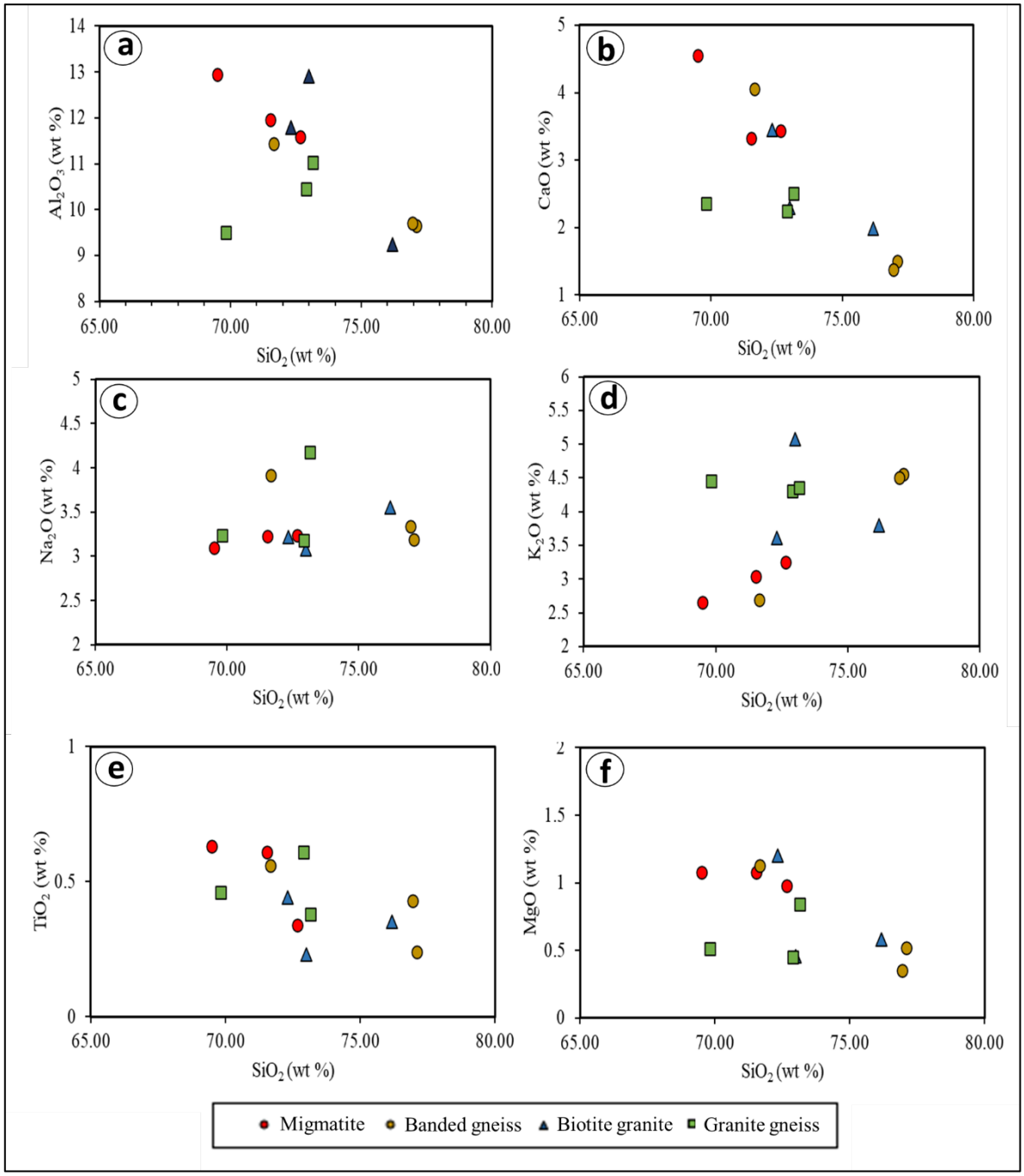

Figure 6. Harker variation diagram of (a) Al_2O_3 versus SiO_2, (b) CaO versus SiO_2, (c) Na_2O versus SiO_2, (d) K_2O versus SiO_2 (e) TiO_2 versus SiO_2 and (f) MgO versus SiO_2. (Symbols as in Figure 7).

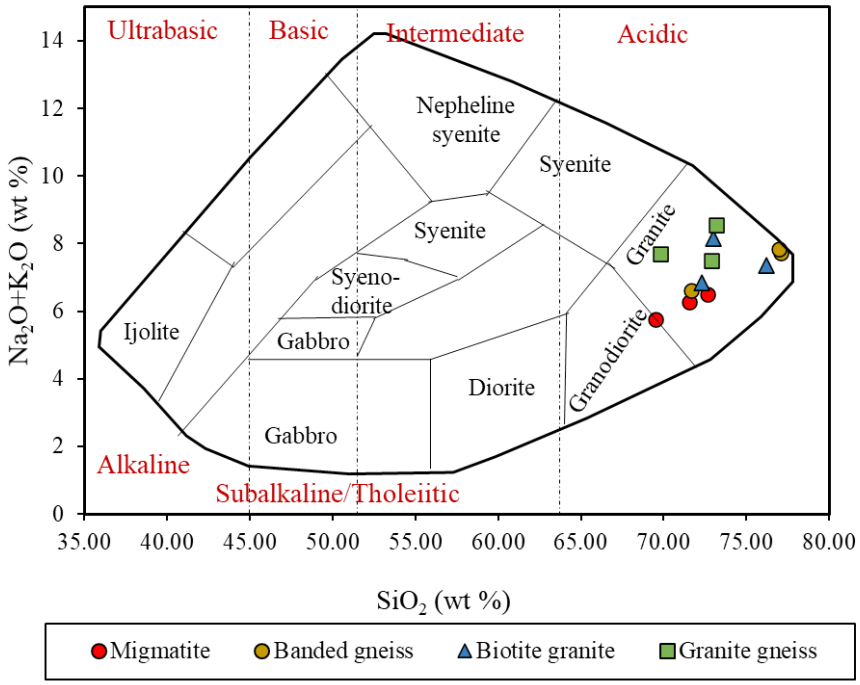

Figure 7. ($Na_2O + K_2O$) versus SiO_2 plot of the crystalline rocks in Ora-Ekiti (after Middlemost [16]).

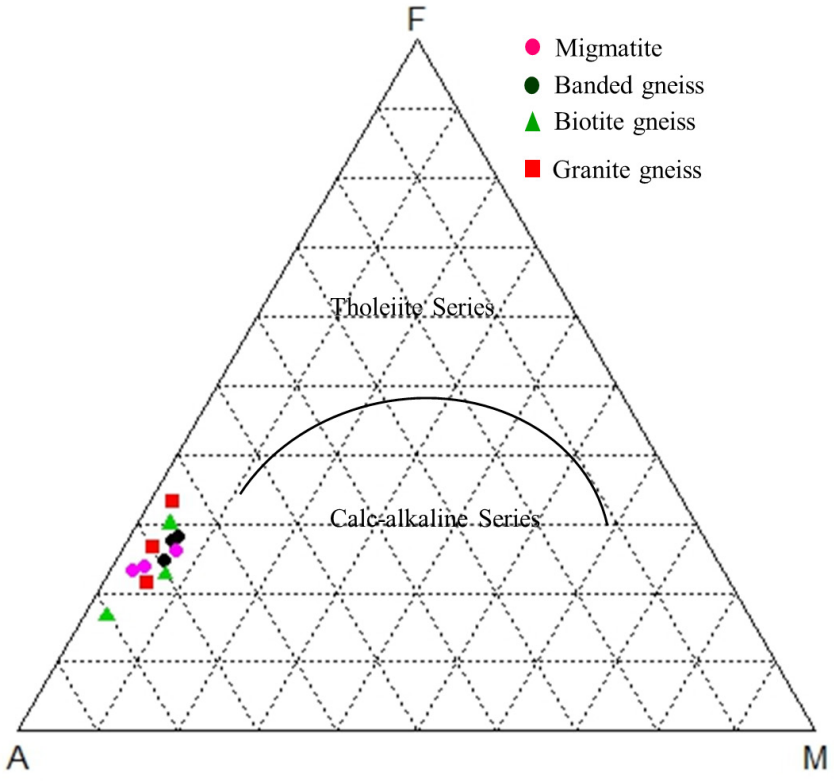

Figure 8. AFM diagram of the rocks in the study area (after Irvine and Baragar [17]).

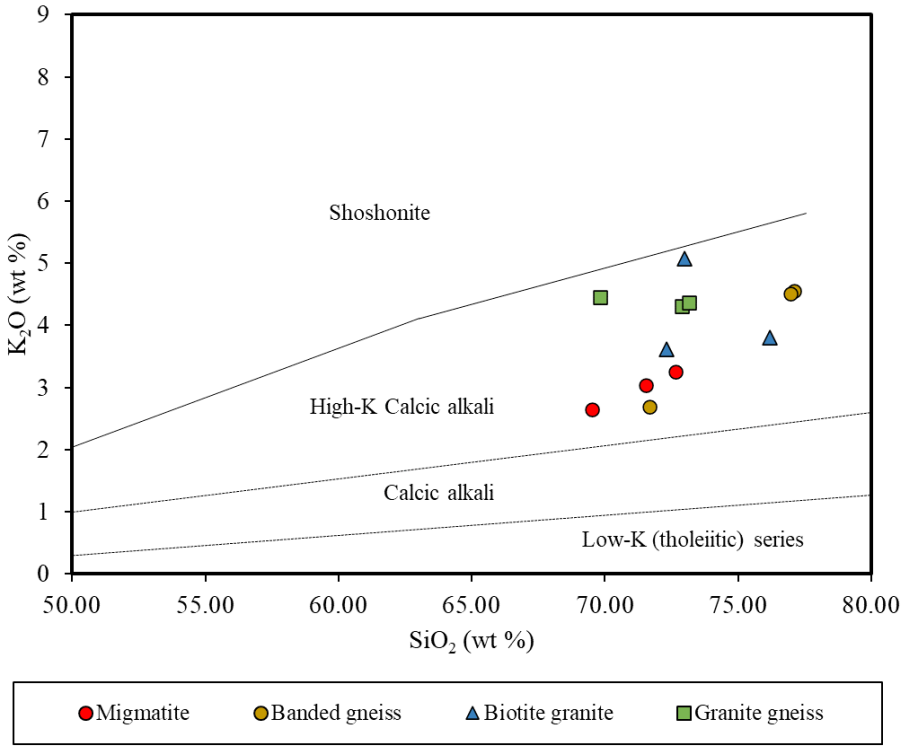

Figure 9. SiO_2 versus K_2O plot showing the geochemical character of the rock samples (after Peccerillo and Taylor [18]).

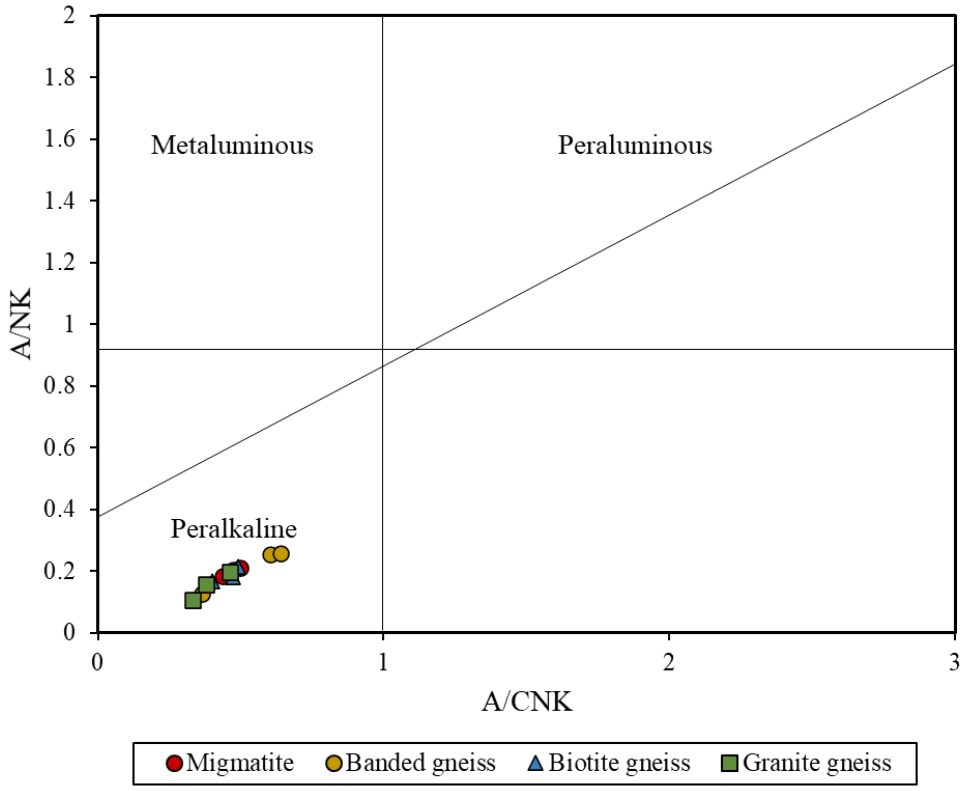

Figure 10. Binary plot of A/NK versus A/CNK (after Shand [19]) for the crystalline rocks in Ora-Ekiti.

5. Summary and conclusions

Exhaustive geological investigation reveals the study area is underlain by migmatite, banded gneiss, granite gneiss and biotite gneiss. Migmatite occupies western and northern parts, banded gneiss underlies Ora-Ekiti town and extends towards the northeast. Granite gneiss underlies the eastern and southwestern corners of the area while biotite gneiss occurs towards the south.

Petrographic examination indicates the rocks are principally dominated by quartz, plagioclase, biotite and opaque each contributing slightly varying percentages to the modal composition.

The rocks have high alumina content with pronounced enrichment in Ba, Sr and Rb. The rocks are dominantly peralkaline in nature. The rocks experienced either crystal fractionation before metamorphic remobilization or partial melting in the precursor rocks. The chemical composition of the rocks depicts they are metaluminous granitoids of calc-alkaline affinity.

Conflict of Interest

There is no conflict of interest.

Acknowledgement

The authors wish to acknowledge Prof. (Dr). Ghani, A. A. of the Department of Geology, University of Malaya for the link for geochemical analysis. The students who assisted during the fieldwork are gratefully acknowledged.

References

[1] Rahaman, M.A., 1988. Recent advances in study of the basement complex of Nigeria Precambrian geology of Nigeria. Precambrian Geology of Nigeria. Geological Survey of Nigeria Publication, Kaduna. p. 11-43.

[2] Oluyide, P.O., Nwajide, C.S., Oni, A.O., 1998. The geology of the Ilorin area. Bulletin, GSN. 42, 84.

[3] Okonkwo, C.T., 1992. Structural geology of basement rocks of Jebba area, Nigeria. Journal of Mining and Geology. 35(1), 9-21.

[4] GSN, 1966. Geological Survey of Nigeria, Geological map of Akure, Sheet 61, 1:250,000.

[5] Oyinloye, A.O., Obasi, R.A., 2006. Geology, geochemistry and geotectonic setting of the Pan-African granites and charnockite around Ado-Ekiti, Southwestern Nigeria. Pakistan Journal of Science and Industrial Research. 49(5), 299-308.

[6] Obaje, N.G., 2009. Geology and mineral resources of Nigeria. Lecture notes in Earth Sciences. Springer: Berlin. pp. 72-97.

[7] Burke, K.C., Dewey, J.F., 1972. Orogeny in Africa. Africa geology. University of Ibadan Press: Ibadan. pp. 583-608.

[8] Dada, S.S., 2006. Proterozoic evolution of Nigeria. The basement complex of Nigeria and its mineral resources. Petrochemical. Services Limited Ibadan: Nigeria. pp. 29-45.

[9] Abaa, S.I., 1983. The structure and petrography of alkaline rocks of the Mada Younger Granite. Journal of African Earth Sciences. 3(1-2), 107-113.

[10] Gandu, A.H., Ojo, S.B., Ajakaiye, D.E., 1986. A gravity study of the Precambrian rocks in the Malumfashi area of Kaduna State, Nigeria. Tectonophysics. 126, 181-194.

[11] Olayinka, A.I., 1992. Geophysical siting of boreholes in crystalline basement areas of Africa. Journal of Africa Earth Science. 14, 197-207.

[12] de Swardt, A.M.J., 1953. The geology of the country around Ilesha. Bulletin of Geological Survey of Nigeria. 23, 54.

[13] Falconer, J.D., Woods, S., 1911. The geology and geography of Northern Nigeria. Macmillan and Company, limited: UK. pp.458-459.

[14] NGSA, 2006. Nigeria Geological Survey Agency Map of Ekiti State [Internet]. Available from: https://ngsa.gov.ng/

[15] Roselee, M.H., Ghani, A.A., Umor, M.R., 2016. Petrology and geochemistry of igneous rocks from southern Tioman Island, Pahang, Peninsular Malaysia. Bulletin of the Geological Society

of Malaysia. 62, 79-89.

[16] Middlemost, E.A., 1994. Naming materials in the magma/igneous rock system. Earth Science Reviews. 37(3-4), 215-224.

[17] Irvine, T.N., Baragar, W.R.A., 1971. A guide to the classification of common volcanic rocks. Canadian Journal Earth Science. 8, 523-548.

[18] Peccerillo, A., Taylor, S.R., 1976. Geochemistry of Eocene calc-alkaline volcanic rocks from the Kastamona area, northern Turkey. Contribution to Mineralogy and Petrology. 58, 63-81.

[19] Shand, S.J., 1943. Eruptive rocks: Eruptive rocks, their genesis, composition, and classification, with a chapter on meteorites. Science. 99(2562), 101-102.

BILINGUAL PUBLISHING GROUP

Advances in Geological and Geotechnical Engineering Research

https://journals.bilpubgroup.com/index.php/agger

ARTICLE

Toxicity of Radon-222 in Groundwater across Keana in Nasarawa, Nigeria

Abubakar Saidu Bako[1], Usman Rilwan[2*], Ibrahim Umar[1], Samson Dauda Yusuf[1], Idris Muhammad Mustapha[1], Abdullahi Abubakar Mundi[1], Ibrahim Maina[3]

[1] *Department of Physics, Nasarawa State University, PMB 1022 Keffi, Nasarawa State, Nigeria*

[2] *Department of Physics, Nigerian Army University, PMB 1500 Biu, Borno State, Nigeria*

[3] *Department of Physics, Abubakar Tafawa Balewa University, PMB 0248 Bauchi, Bauchi State, Nigeria*

ABSTRACT

The most common supply of freshwater for drinking, irrigation, and other domestic uses is groundwater; however, because of increased radon concentrations brought on by mining activities, its quality is still a severe concern. Using a liquid scintillation detector, this study investigated the radon content, its related toxicity, and its risk to human health in the groundwater of the Keana in Nasarawa, Nigeria. Ten (10) borehole samples and five (5) well samples totaling fifteen (15) groundwater samples were taken. The results showed that the average radon concentration in water samples from Keana was 2.25 Bq/L. The mean annual effective dosage (ingestion) for adults and children in Keana was 0.016 mSv/y and 0.027 mSv/y, respectively. In Keana, the additional lifetime cancer risk per adult was 5.65×10^{-5}, and per child, it was 8.79×10^{-5}. The study's radon concentration was lower than the benchmark of 11.1 Bq/L established in 1991 by the Nigerian Standard Organization and the US Environmental Protection Agency. The results of this study indicate that the level of radon is safe; as a result, people can continue farming and other activities. To reduce the risk of cancer, however, more research could be done in the area. Further research should be done by looking at additional sources in the study area in order to cover the entire zone. Further investigation should be carried out both during the dry and wet seasons because radon concentrations in groundwater alter over time due to dilution by recharge from rainfall.

Keywords: Ingestion; Inhalation; Irrigation; Radon; Yearly effective dose; Excess lifetime cancer risk

*CORRESPONDING AUTHOR:

Usman Rilwan, Department of Physics, Nigerian Army University, PMB 1500 Biu, Borno State, Nigeria, 603108, Nigeria; Email: rilwan.usman@naub.edu.ng

ARTICLE INFO

Received: 31 March 2023 | Revised: 19 April 2023 | Accepted: 21 April 2023 | Published Online: 28 April 2023

DOI: https://doi.org/10.30564/agger.v5i2.5632

CITATION

Bako, A.S., Rilwan, U., Umar, I., et al., 2023. Toxicity of Radon-222 in Groundwater across Keana in Nasarawa, Nigeria. Advances in Geological and Geotechnical Engineering Research. 5(2): 38-49. DOI: https://doi.org/10.30564/agger.v5i2.5632

1. Introduction

Water is one of the most plentiful materials on earth and is a crucial component of all living things, according to a 2010 report by Darko et al. It is utilized in many facets of daily life, including domestic work, agriculture, and the production of power. Water must be free of chemical, microbiological, and radioactive contaminants as a result [1].

In the disintegration chain of Uranium-238 is the radioactive gas radon, which is colorless and odorless [2].

The above-described radon is a naturally occurring element that leads to radioactive contamination of drinking water and poses a health risk, according to reports by Farai and Sanni in 1992 [3] and Darko et al. in 2010 [4]. It has been acknowledged as a health issue since the late 1980s. When uranium or radium decays, a radioactive gas known as radon is created. It seeps into the environment or into human habitations after evaporating from the earth's crust through bedrock fractures and crevices and dissolving in ground water [1,4].

According to a 2010 assessment by Darko et al., as reported by Rilwan et al. in 2022 [4,5] the people of Nasarawa only use untreated groundwater (from wells and boreholes) and surface water sources. This is due to the limited number of pipe-borne water sources that are available and the fact that they are frequently inoperable. A naturally occurring radioactive inert gas with a half-life of 3.82 days, Radon-222 is soluble in water and belongs to the uranium decay series. The majority of the radiation from all-natural sources comes from it [5].

According to studies, the amount of Radon-222 (^{222}Rn) and its offspring that makes up the total effective dosage equivalent from natural sources is roughly 50% [5,6]. Water contains a high amount of ^{222}Rn due to the decay of Radium-226 found in rocks and soil [5,7]. Radon gas permeates rocks and soil before dissolving in water [5,8]. Drinking water from sources of groundwater typically contains more radon than surface water [5,9].

Long-term exposure to high levels of radon and its offspring can have serious health consequences for a community, including lung cancer and altered respiratory function [5,10]. Moreover, stomach and gastrointestinal tract cancer can result from very high radon levels in drinking water [5,11].

In Nasarawa, finding access to potable water sources has remained one of the major challenges. As a result, the majority of people and animals depend on untreated surface and groundwater sources for consumption. The radon level in drinking water, which in high concentration can cause a significant risk of stomach and gastrointestinal tract cancer [11], among others, needs to be investigated. The geology of Nasarawa revealed that it is highly enriched in clay, loamy, and sandy soil, and studies have shown that high activity concentrations of Radon-222 are always associated with areas rich in clay soil [11]. This is more so because our understanding of its amount of availability could be of tremendous use in resource planning [12].

Due to their strong ionization strength, alpha rays pose a greater risk than beta and gamma rays when it comes to internal exposure [13]. Because Radon-222 is very soluble, eliminating the radon can be accomplished by adjusting the water's temperature [14]. According to reports that have been published, the concentration of Radon-222 in groundwater sources can be estimated to be two- to three-times higher than that of other radioactive elements [14-18].

The radiological effects brought on by consuming dissolved radon in drinking water are described using the population's effective radiation dosage during ordinary water consumption. The average annual water consumption rates (ACR) for the general population were used to calculate the doses from drinking water intake for children and teens [19]. However, a number of 2 liters per day (730 liters per year) for adults was used here in order to be consistent with the bulk of global drinking water guidelines [20]. The International Commission on Radiological Protection (ICRP) age categories and related ACRs are listed in **Table 1**.

Table 1. International Commission on Radiological Protection (ICRP) age groups and their Annual Water Consumption Rate (ACR).

Age Group	Age Range (Years)	Water Consumption (L/day)	Water Consumption (L/years)	Reference
3 Months	0 to 1	0.55	200	[12,20]
1 Year	1 to 2	0.71	260	[12,20]
5 Years	2 to 7	0.82	300	[12,20]
10 Years	7 to 12	0.96	350	[12,20]
15 years	12 to 17	1.64	600	[12,20]
Adults	Greater than 17	2.00	730	[12,20]

Measurement of radon content in water sources near the Ririwai Artisanal Tin Mine was the focus of Zakari et al.'s (2015) research [21] who did their research in Kano State, Nigeria. In their research, the amount of ^{222}Rn in three water sources near the Ririwai Artisanal Tin Mine was determined using liquid scintillation analysis. The annual effective dosage caused by the concentration of ^{222}Rn in domestic and surface water sources was also calculated. After their analysis, they concluded that the mean ^{222}Rn concentration found in this study was less than the 10 Bq/L levels that WHO and UNSCEAR recommend. Additionally, the study's annual effective dose was less than the UNSCEAR-recommended upper limit of 0.1 mSv/year. Also, Garba et al. (2013) [22] started a project called Radon Assessment of Groundwater (wells and boreholes). In their research, samples were taken from different parts of Zaria and its surroundings, including Sabongari, Tudunwada, Danmagaji, Samaru, and Bomo. In accordance with the findings of their study, the ^{222}Rn content in borehole sources is higher than that in well water sources, and both were above the USEPA-set MCL of 11.1 Bq/L. In another research, the estimation of indoor radon and its progeny in dwellings of Akoko Area, Ondo State, Southern Nigeria, was undertaken by Adeola and Isaac in 2017 [23]. Accustar alpha-track long-term passive test devices with CR-39 solid-state nuclear track detector foil were used for the test. In the Akoko region of Nigeria's Ondo state, radon levels were tested in a few residences constructed from various types of materials. The detectors were out in the elements for six months. The detectors were electrochemically etched after removal, and a computer-aided image analysis system was used to count them. The study demonstrates that radon concentrations in these places are significantly influenced by the local soil composition.

Despite the fact that Nasarawa's geology revealed that it has a high concentration of clay soil, there is no reliable information on the concentration of radon in the area from a review of the literature. As a result, this study aims to determine the potential health risk posed by radon in Nasarawa's water sources as well as the annual dose of radon consumed through drinking water. The results must be contrasted with industry standards and the results of other studies.

2. Materials and methods

2.1 Materials

The equipment and its specifications are listed in **Table 2**, and **Plate 1** shows the liquid scintillation counter that was used to gauge the radon levels in Keana's groundwater.

Table 2. Materials and their specifications.

S/N	Materials	Specifications
1	Water sample	100 mL
2	Plastic sample collection bottles	50 mL
3	Liquid Scintillation Counter (manufactured by Packard Tri-carb LSA 1000TR)	1
4	Disposable hypodemic syringe (20 mL, 10 mL and 2 mL) capacity with 38 mm hypodermic needle	8
5	distilled water	1 litre
6	Scintillation vial-20 mL with cap	Plastic
7	Surgical globe	1 pack
8	Indelible ink and masking tape	1
9	Mineral oil (insta-gel)	1

2.2 Method

Study population

The population of the study includes all of the boreholes and wells that are situated within the Keana Local Governments of Nasarawa State, which are Ewagu, Oleye, Emir Palace, Oki, Market, Aloshi, GGSS Keana, Jimini, Kachiya, Kalachi, Obne, and Madaki.

Study area

The Nasarawa South senatorial district is located in northern Nigeria's Guinea Savannah and is a part of the low plains of Benue origin. A number of weathered volcanic cones, mostly made of sandstone, surround the salt mining community of Keana. These detached synclinal areas were created by localized folding. **Table 3** displays Keana's sample codes and GPS coordinates. **Figure 1** shows a map of the research area.

Table 3. Sample codes and GPS locations of Keana.

S/N	Sampled Water	Location	Sample Code	Latitude (°) N	Longitude (°) E
1	Borehole	Ewagu	KEB1	8.1504	8.7901
2	Borehole	Oleye	KEB2	8.1305	8.6311
3	Borehole	Emir Palace	KEB3	8.1202	8.7023
4	Borehole	Oki	KEB4	8.1513	8.8012
5	Borehole	Market	KEB5	8.1234	8.7601
6	Borehole	Aloshi	KEB6	8.1340	8.8103
7	Borehole	GGSS Keana	KEB7	8.1241	8.6201
8	Borehole	Jimini	KEB8	8.1321	8.6420
9	Borehole	Kachiya	KEB9	8.1622	8.8210
10	Borehole	Kalachi	KEB10	8.1524	8.7204
11	Well	Emir Palace	KEW1	8.1140	8.6622
12	Well	Obne	KEW2	8.1441	8.6734
13	Well	Ewagu	KEW3	8.1401	8.7904
14	Well	Oleye	KEW4	8.1503	8.8010
15	Well	Madaki	KEW5	8.1310	8.7521

KEB = Borehole Water Sample; KEW = Well Water Sample.

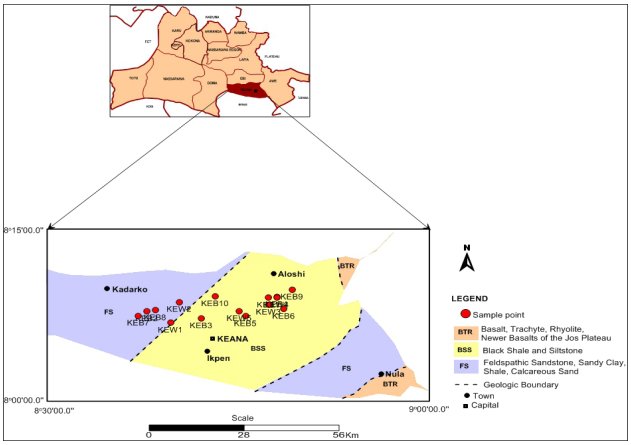

Figure 1. Map of the area showing the sample locations.

Technique used to collect samples

In plastic containers with coverings, five (5) water samples and fifteen (15) groundwater samples (from wells and boreholes) were gathered. The plastic containers were first cleaned and rinsed with distilled water to avoid radon in the samples from becoming contaminated. Water samples were held with 20 mL of concentrated HNO_3 per liter of water in order to reduce radon absorption on container walls.

The water samples were only collected after the boreholes had been operational for at least four minutes in order to ensure that new samples were obtained.

The containers were quickly sealed to prevent loss of radon during transport to the lab and were then completely filled with the water sample without any headspace. This was done to avoid CO_2 being trapped and dissolved in water, which could change the chemistry, such as pH, at each location.

The samples were sent for examination as soon as they were obtained and for no more than three days at maximum in order to minimize the effects of radioactive decay. This is done to guarantee complete accuracy without altering its composition.

Technique for preparing samples

Each sample of water was divided into 10 mL pieces, added to a 20 mL glass scintillation vial with 10 mL of an insta-gel scintillation cocktail, and shaken. The vials were tightly closed, shaken for more than two minutes, and then Radon-222 in the aqueous phase was extracted into the organic scintillate. The samples were then gathered, and for 60 minutes, they were tallied in a liquid scintillation counter em-

ploying energy discrimination for alpha particles.

Technique for analyzing samples

The samples were evaluated at Ahmadu Bello University's Centre for Energy Research and Training in Zaria, Nigeria, using a liquid scintillation counter (Tri-Carb LSA 1000TR type).

The liquid scintillation counter (LSC) was used to measure the concentration of ^{222}Rn in water. The approach was comparable to that created by the American Society for Testing and Materials (ASTM). An LSC vial containing an LSC cocktail that is incompatible with water is mixed with a water sample. When radon has reached a state of equilibrium with its short-lived decay products, shaking is utilized to shift it into the organic phase and count it. Some radionuclides are unaffected by this technique. With low-background counting equipment and a 1-hour counting period, a sensitivity of around 0.5 Bq/L could be attained [17,24].

In liquid scintillation counting devices, the main detector is an organic phosphor called Cocktail. It is uniformly disseminated after being dissolved in the proper solvent (this is commonly referred to as the cocktail). The liquid scintillation cocktail also contains a second organic phosphor that alters wavelengths. After adding the sample, this mixture creates the test source [17,24].

The solvent, primary, and secondary scintillators make up the liquid scintillation cocktail. The shelf life of the organic components utilized to make the scintillators is limited [17,24].

The liquid scintillation counter (Tri-Carb LSA 1000TR) type is shown in **Plate 1** and was used to assess the level of radon in the groundwater in Nasarawa South, Nigeria. It is located at Ahmadu Bello University in Zaria, Nigeria's Center for Energy Research and Training (CERT).

Plate 1. Showing liquid scintillation counter (Tri-Carb LSA 1000TR) model.

Approach to data analysis

The analysis for this study is divided into four (4) sections, including the determination of the concentration in Bq/L, the annual effective dose for adults and children, the excess lifetime cancer risk, and a comparison of the results with previous studies and industry standards. Tables are used to present the analysis's findings.

a. Estimation of Radon-222 concentration in Bq/L

According to Rilwan et al. (2022) and USEPA (2019) [5,25], Equation (1) was used to determine the Radon-222 concentration in Bq/L as follows:

$$Rn(BqL^{-1}) = \frac{100ml(CS - CB)}{10ml \times 1.0L(CF \times D)} \quad (1)$$

Rn is the radon level in Bq/L, and the variables are CS = sample count/second, CB = background count/second, CF = conversion factor, and D = decay constant.

b. Effective dose by ingestion per year

It is vital to translate radon concentration into a dose because of the harmful effects of radon on the human body. The radon levels for the research region were used to compute the annual effective dosage equivalent. The United Nations Scientific Committee on the Effects of Atomic Radiation recommended the following equation to calculate the annual effective dose of ^{222}Rn from drinking water [21,22,25]:

$$E = K \times G \times C \times T \times 1000 \quad (2)$$

where T is the amount of time (365 days) during which water is consumed, C is the concentration of ^{222}Rn (Bq/L), G is the amount of water consumed each day (4 L/d), E is the annual effective dose (mSv/y), D is the concentration of ^{222}Rn that results from converting Sv to mSv (7×10^{-8} Sv/Bq), and 1000 is the conversion coefficient.

c. Annual effective dose by inhalation

Adeola and Isaac (2017) and USEPA (2019) [23,25] used the following equation to get the annual effective dose of ^{222}Rn when inhaled:

$$He = C \times F \times R \times D \quad (3)$$

He equals the yearly effective dose (mSv/y), C the radon concentration (Bq/L), F the equilibrium factor (0.4), T the time of indoor occupancy (7000 h/y), and D

the dose conversion factor (7×10^{-8} mSv/h/Bq/L).

d. Estimating the excess lifetime cancer risk

Garba et al. (2013) and USEPA (2019) [22,25] computed the increased lifetime cancer risk using Equation (4) as follows:

$$ELCR = AEDE \times DL \times RF \times 10^{-3} \quad (4)$$

where ELCR is for excess lifetime cancer risk, AEDE is for annual effective dose equivalent, DL is for average life expectancy (about 70 years), and RF is for risk factor (Sv^{-1}), which refers to the risk of dying from cancer according to Sievert. The ICRP adopts RF as 0.05 for public stochastic effects.

3. Results

The concentration of Radon-222 in Bq/L, the annual effective dose for adults and children, the excess lifetime cancer risk, and other outcomes from this study were all examined. These findings were compared to norms and those of other studies. **Tables 4-7** present the findings of the analysis.

Table 4 presented the analysis for concentration in Bq/L; **Tables 5 and 6** presented the analysis for annual effective doses by ingestion and inhalation for adults and children; **Table 7** presented the analysis for excess lifetime cancer risk; and **Table 8** presented a comparison of the findings with those of other researchers and industry standards.

3.1 Radon-222 concentration

Table 4 provides the results for the Rn-222 concentrations in Bq/L of water samples from Keana.

According to **Table 4**, the Rn-222 concentration in Bq/L values for both borehole and well water samples from Keana ranged from 2.0 Bq/L for the lowest concentration level for sample point KEB8 to 3.20 Bq/L for the highest con-centration level for sample point KEB3, while for well water samples they ranged from 2.06 Bq/L for the lowest concentration level for sample point KEW4 to 2.22 Bq/L for the highest concentration level for sample point KEW1 Keana's mean radon concentration was discovered to be 2.25 Bq/L.

Table 4. Rn-222 concentrations in Bq/L of water samples from Keana.

S/N	Sample ID	Radon Concentration (Bq/L)
1	KEB1	2.10
2	KEB2	2.21
3	KEB3	3.20
4	KEB4	2.41
5	KEB5	2.03
6	KEB6	2.18
7	KEB7	1.91
8	KEB8	2.00
9	KEB9	2.18
10	KEB10	2.96
11	KEW1	2.22
12	KEW2	2.12
13	KEW3	2.13
14	KEW4	2.06
15	KEW5	2.12
	Mean	**2.25**

KEB = Borehole Water Sample; KEW = Well Water Sample.

3.2 3Annual effective dose by ingestion

Equation (2) was used to compute the annual effective dosage from **Table 4**, and the results are shown in **Table 5**.

Keana's annual effective dose by ingestion was calculated from **Table 5** using the corresponding measured radon concentrations. It was found that for adults the annual effective dose by ingestion for borehole water samples varies from 0.009 mSv/y for sample point KEB7 as the lowest value to 0.023 mSv/y for sample points KEB3 as the highest value while for well water samples were 0.015 mSv/y for sample points KEW2, KEW4 and KEW5 as the lowest values to 0.016 mSv/y for sample point KEW1 and KEW3 as the highest values. Ingestion of the mean effective dosage of Radon-222 for humans from borehole and well water samples is 0.016 mSv/y.

The annual effective dose by ingestion for children was determined to be 0.025 mSv/y for sample points KEW2, KEW4, and KEW5, with sample point KEW11 having the highest value. For borehole water samples, the annual effective dose by ingestion

ranged from 0.023 mSv/y for sample point KEB7 as the lowest value to 0.038 mSv/y for sample point KEB3. Both borehole and well water samples have a mean effective dosage via consumption of Radon-222 for children of 0.027 mSv/y.

Table 5. Annual effective dose by ingestion of water samples from Keana.

S/N	Sample ID	Annual Effective Dose by Ingestion for Adults ($mSvy^{-1}$)	Annual Effective Dose by Ingestion for Children ($mSvy^{-1}$)
1	KEB1	0.015	0.024
2	KEB2	0.016	0.026
3	KEB3	0.023	0.038
4	KEB4	0.018	0.029
5	KEB5	0.015	0.024
6	KEB6	0.016	0.026
7	KEB7	0.009	0.023
8	KEB8	0.015	0.024
9	KEB9	0.022	0.035
10	KEB10	0.016	0.026
11	KEW1	0.016	0.027
12	KEW2	0.015	0.025
13	KEW3	0.016	0.026
14	KEW4	0.015	0.025
15	KEW5	0.015	0.025
	Mean	**0.016**	**0.027**

KEB = Borehole Water Sample; KEW = Well Water Sample.

3.3 Annual effective dose by inhalation

Equation (3) was used to compute the annual effective dosage by inhalation from **Table 4**, and the results are shown in **Table 6**.

Keana's annual effective dosage from the matching measured radon concentrations was computed using data from **Table 6**. The annual effective dose by inhalation for adults was found to range from 0.048 mSv/y for sample point KEB7 to 0.075 mSv/y for sample point KEB10, while for well water samples, the annual effective dose ranged from 0.052 mSv/y for sample point KEW4 to 0.056 mSv/y for sample point KEW1 as the highest values. Both borehole and well water samples have a mean effective dosage by inhalation owing to Radon-222 of 0.055 mSv/y.

Table 6. Annual effective dose by inhalation of water samples from Keana.

S/N	Sample ID	Annual Effective Dose by Inhalation ($mSvy^{-1}$)
1	KEB1	0.053
2	KEB2	0.056
3	KEB3	0.055
4	KEB4	0.061
5	KEB5	0.051
6	KEB6	0.055
7	KEB7	0.048
8	KEB8	0.050
9	KEB9	0.055
10	KEB10	0.075
11	KEW1	0.056
12	KEW2	0.053
13	KEW3	0.054
14	KEW4	0.052
15	KEW5	0.053
	Mean	**0.055**

KEB = Borehole Water Sample; KEW = Well Water Sample.

3.4 Excess lifetime cancer risk

Equation (4) was used to compute the increased lifetime cancer risk, and the findings are shown in **Table 7**.

Keana's extra lifetime cancer risk was calculated using data from **Table 7** and the matching determined annual effective dosage. Adults' excess lifetime cancer risk from borehole water samples ranges from 3.15×10^{-5} for sample point KEB7 to 8.05×10^{-5} for sample point KEB3, while the excess lifetime cancer risk from well water samples ranges from 5.25×10^{-5} for sample points KEW2, KEW4, and KEW5 to 5.60×10^{-5} for sample points KEW1 and KE3. Both borehole and well water samples have a mean extra lifetime cancer risk for adults ow-

ing to Radon-222 of 5.65×10^{-5}.

The excess lifetime cancer risk for children in borehole water samples ranges from 8.05×10^{-5} for sample point KEB7 to 1.33×10^{-4} for sample point KEB3, while the excess lifetime cancer risk in well water samples was found to be 8.75×10^{-5} for sample points KEW2, KEW4, and KEW5 as the lowest value to 9.45×10^{-5} for sample point KEW1. Both borehole and well water samples have a mean extra lifetime cancer risk for children owing to Radon-222 of 8.57×10^{-5}.

Table 7. Excess lifetime cancer risk of water samples from Keana.

S/N	Sample ID	Excess Lifetime Cancer Risk for Adults ($\times 10^{-5}$)	Excess Lifetime Cancer Risk for Children ($\times 10^{-5}$)
1	KEB1	5.25	8.40
2	KEB2	5.60	9.10
3	KEB3	8.05	13.30
4	KEB4	6.30	1.02
5	KEB5	5.25	8.40
6	KEB6	5.60	9.10
7	KEB7	3.15	8.05
8	KEB8	5.25	8.40
9	KEB9	7.70	12.25
10	KEB10	5.60	9.10
11	KEW1	5.60	9.45
12	KEW2	5.25	8.75
13	KEW3	5.60	9.10
14	KEW4	5.25	8.75
15	KEW5	5.25	8.75
	Mean	**5.65**	**8.79**

KEB = Borehole Water Sample; KEW=Well Water Sample.

3.5 Comparison with standard and other researchers

As shown in **Table 8** (**Figure 2**), **Table 9** (**Figure 3**) and **Table 10** (**Figure 4**), the findings from this study were compared to safety requirements, works from other researchers in Nigeria, and works from other researchers worldwide.

Table 8. Comparison of radon concentration from present study with standards.

S/N	Standard	Radon Concentration (Bq/L)	Reference
1	United Nation Scientific Committee on Effect of Atomic Radiation (UNSCEAR)	4.0-40.0	[21,26]
2	United States Environmental Protection Agency (USEPA)	11.1	[21,26]
3	European Commission for Drinking Water Purposes	100	[21,25]
4	World Average	10	[22]
5	Standard Organization of Nigeria (SON)	11.1	[21]
6	Keana	2.25	Present Study (2023)

Table 9. Comparison of radon concentration from present study with other places in Nigeria.

S/N	Location	Radon Concentration (Bq/L)	Reference
1	Kano State	2.29	[21,25]
2	Kaduna State	12.29	[22,25]
3	Ondo State	35.54	[23,25]
5	Keana	2.25	Present Study (2023)

According to **Table 8** (**Figure 2**), Keana's radon levels were within the acceptable limits recommended by the United Nations Scientific Committee on the Effect of Atomic Radiation (UNSCEAR), the European Commission for drinking purposes, the USEPA's maximum contamination level, and the global average.

According to **Table 9** (**Figure 3**), the radon concentration of groundwater samples from Keana is lower than that of Ado-Ekiti in the state of Ekiti, Gadau in the state of Bauchi, Idah in the state of Kogi, and Zaria in the state of Kaduna.

Table 10. Comparison of radon concentration of groundwater samples from present study with other parts of the world.

S/N	Location	Radon Concentration (Bq/L)	Reference
1	India	2.63	[23,25]
2	Turkey	9.28	[23,25]
3	Romania	15.40	[23,25]
4	Jordan (many locations)	2.8-116	[23,25]
5	Lebanon (many locations)	11.30	[23,25]
6	Tassili, South-east Algeria	0.67-21.25	[23,25]
7	Eastern Doon Valley, outer Himalayas	20-95	[23,25]
8	Northern Venezuela	0.1-5.76	[23,25]
9	Finland	63.0	[23,25]
10	United States of America	5.20	[23,25]
11	Keana, Nigeria	2.25	Present Study (2023)

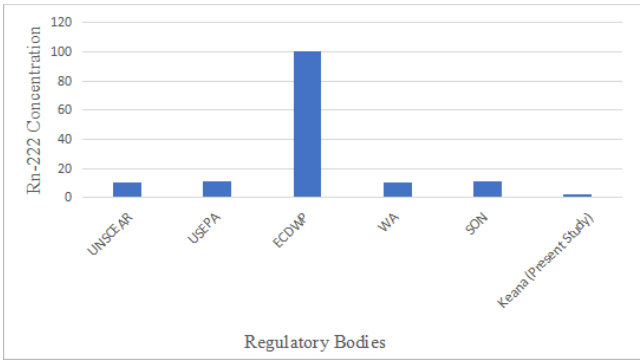

Figure 2. Comparison of radon concentration from present study with standards.

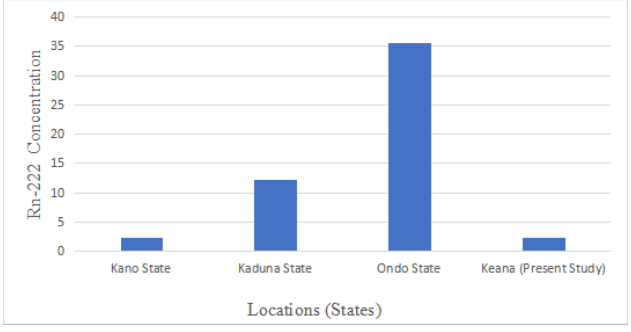

Figure 3. Comparison of radon concentration from present study with other places in Nigeria.

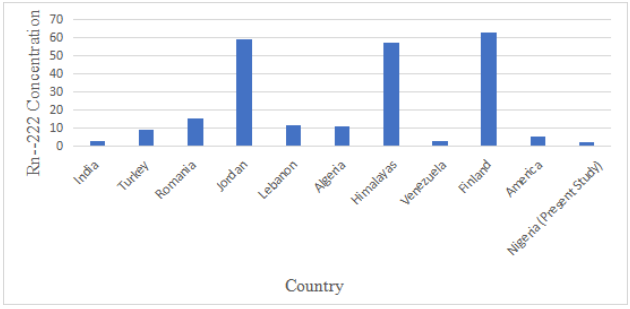

Figure 4. Comparison of radon concentration of groundwater samples from present study with other parts of the world.

According to **Table 10** (**Figure 4**), groundwater samples from Keana have radon concentrations that are lower than those from countries like India, Romania, Jordan, the outer Himalayas, Finland, Turkey, Lebanon, and the United States, but higher than those from some regions of Algeria and some regions of Northern Venezuela.

4. Discussion

The results of this study showed that Keana's mean radon concentration was 2.25 Bq/L. This value was lower than the global average of 10 Bq/L, the Standard Organization of Nigeria's (SON) 11.1 Bq/L, the European Union Commission's 100 Bq/L, the United Nations Scientific Committee on Atomic Radiation's (UNSCEAR) 4.0-40.0 Bq/L, and the United States Environmental Protection Agency's (11.1 Bq/L) (USEPA). The results of Zakari et al. [21], who discovered a mean radon concentration of 2.29 Bq/L is within the same range, are consistent with our discovery.

This result differs from that of Garba et al. (2013) [22], who discovered that the mean radon concentration was 12.29 Bq/L. The results of Adeola and Isaac (2017) [23], who discovered that the mean radon concentration was 35.54 Bq/L, are also out of sync.

The corresponding measured radon concentrations in the borehole water samples from Keana were 0.017 mSv/y for adults and 0.028 mSv/y for children, whereas the corresponding measured radon concentrations in the well water samples were 0.015 mSv/y for adults and 0.026 mSv/y for children.

The Standard Organization of Nigeria (SON) approved the WHO's recommended reference level of 0.1 mSv/y for intake of radionuclides in water and the ICRP's recommended intervention level of 3-10 mSv/y for radionuclide intake.

The radon concentrations in the borehole water samples from Keana that corresponded to the mean annual effective dosage by inhalation were 0.056 mSv/y and 0.054 mSv/y, respectively.

All annual effective dosage by ingestion readings fell below the 1 mSv/y threshold that is advised for the general public.

For well water samples, the excess lifetime cancer risk was 5.39×10^{-5} for adults and 8.96×10^{-5} for children, whereas the excess lifetime cancer risk from the same annual effective dose of borehole water samples from Keana was 5.79×10^{-5} for adults and 8.71×10^{-5} for children.

According to the global average of 2.9×10^{-4} as reported by Ibikunle et al. in 2018, the extra lifetime cancer risk of water samples from the Keana Local Governments was found to be lower.

5. Conclusions

According to the findings, the radon levels in the groundwater samples from Keana are safe for home use and human consumption because they are below the maximum limit of 11.1 Bq/L established by the USEPA and adopted by the Standard Organization of Nigeria (SON). Since this work pioneered the determination of radon in groundwater in the study area, the data in this study might be utilized as a reference for the study location. In order to cover the entire zone, more borehole and well investigations inside the study region should be conducted. Because radon concentrations in groundwater change over time due to dilution by recharge from rainfall, research should be done both during the dry and wet seasons. Most importantly, government officials at all levels should raise awareness of the dangers of radon exposure for people. In order to establish a comprehensive reference database for radon levels in groundwater in Nasarawa State, it is also advised that future researchers expand this study to other senatorial zones of the State. Also, future researchers should determine the levels of radon in both surface water and groundwater.

Author Contributions

Idris Muhammad Mustapha, Abdullahi Abubakar Mundi and Ibrahim Maina created all the figures in the work, while Abubakar Saidu Bako, Usman Rilwan, Samson Dauda Yusuf and Ibrahim Umaru wrote the majority of the manuscript. The work was examined by all writers.

Conflict of Interest

The corresponding authors affirm that they have no known financial or interpersonal conflicts that would have appeared to have an impact on the research presented in this study.

Funding

No funding was sought for this work because the authors are not associated with any company that has a direct or indirect financial interest in the topic covered in the manuscript.

Acknowledgment

The corresponding authors express gratitude to the remaining authors for their positive criticism and review, which makes the work contributive and worthy of publication.

References

[1] Aruwa, A., Gyuk, P.M., Dogara, M.A., et al., 2017. Determination of Radon-222 concentrations and effective dose by ingestion in ground and surface water sources from Idah and Environs, Nigeria. International Journal of Research—Granthaalayah. 5(9), 15-25.

[2] Farai, I.P., Sanni, A.O., 1992. Yearly variability of ^{222}Rn in a groundwater system in Nigeria. Journal of African Earth Sciences. 15(314), 399-403.

[3] Galan, L.M., Martin, S.A., Gomez, E.V., 2004. Application of ultralow level liquid scintillation to the determination of ^{222}Rn in groundwater. Journal of Radioanalytical and Nuclear Chemistry. 261(3), 631-636.

[4] Darko, E.O., Adukpo, O.K., Fletcher, J.J., 2010. Preliminary studies on ^{222}Rn concentration in groundwater from selected areas of the Accra metropolis in Ghana. Journal of Radioanalytical and Nuclear Chemistry. 283(1), 507-512.

[5] Rilwan, U., Yahaya, I., Musa, M., et al., 2022. Investigation of Radon-222 in water from Loko Town in Nasarawa, Nasarawa State, Nigeria. Journal of Oncology and Cancer Screening. 4(2), 1-7.

[6] Hussein, A.S., 2014. Radon measurements in water samples from western desert of Egypt using nuclear track detectors and estimation of corresponding doses. Radiation Protection and Environment. 37(3), 165-174.

[7] United Nations, 2003 Water for People Water for Life—The United Nations World Water Development Report Executive Summary [Internet]. Available from: https://sustainabledevelopment.un.org/content/documents/WWDR_english_129556e.pdf

[8] International Commission on Radiation Protection, 2005. Annals of ICRP. 60(1), 411-440.

[9] Kumar, A., Kaur, M., Sharma, S., et al., 2016. Radiation dose due to radon and heavy metal analysis in drinking water samples of Jammu district, Jammu & Kashmir, India. Radiation Protection Dosimetry. 71(2), 217-222.

[10] Taskin, H., Karavus, M., Ay, P., et al., 2009. Radionuclide concentrations in soil and life time cancer risk due to gamma radioactivity in Kirklareli, Turkey. Journal of Environmental Radioactivity. 35(1), 53.

[11] Mustapha, A.O., Patel, J.P., Rathore, I.V.S., 2002. Preliminary report on Radon concentration in drinking water and indoor air in Kenya. Environmental Geochemistry and Health. 24(1), 387-396.

[12] WHO, 2011. The guidelines for drinking-water quality, 4th edition. WHO: Geneva.

[13] Hamanaka, S., Shizuma, K., Wen, X.Q., et al., 1998. Radon concentration measurement in water by means of α liquid-scintillation spectrometry with a PERALS spectrometer. Nuclear Instruments and Methods in Physics Research Section A: Accelerators, Spectrometers, Detectors and Associated Equipment. 410(2), 314-318.

[14] Kam, E., Bozkurt, A., 2007. Environmental radioactivity measurements in Kastamonu region of northern Turkey. Applied Radiation and Isotope. 65, 440-444.

[15] Akawwi, E., 2014. Radon-222 concentrations in the groundwater along Eastern Jordan Rift. Journal of Applied Sciences. 14, 309-316.

[16] Ali, N., Khan, E., Akhter, P., et al., 2010. Estimation of mean annual effective dose through radon concentration in the water and indoor air of Islamabad and Murree. Radiation Protection Dosimetry. 141, 183-191.

[17] Forte, M., Rusconi, R., Cazzaniga, M., et al., 2017. The measurement of radioactivity in Italian drinking waters. Microchemical Journal. 85(1), 98-102.

[18] Rangel, J.D., Del-Río, H.L., García, F.M., et al., 2002. Radioactivity in bottled waters sold in Mexico. Applied Radiation and Isotope. 56, 931-936.

[19] Ravikumar, P., Somashekar, R.K., 2014. Determination of the radiation dose due to radon ingestion and inhalation. International Journal of Environmental Science and Technology. 11(1), 489-508.

[20] Cevik, U., Damla, N., Karahan, G., et al., 2006. Natural radioactivity in tap waters of eastern black sea region of Turkey. Radiation Protection Dosimetry. 118(1), 88-92.

[21] Zakari, Y.I., Nasiru, R., Ahmed, Y.A., et al., 2015. Measurement of Radon concentration in water sources around Ririwai Artisanal Tin Mine Kano State, Nigeria. Journal of Natural Sciences Research. 5(24), 49-55.

[22] Garba, N.N., Rabi'u, N., Dewu, B.B.M., et al.,

2013. Radon assessment in ground water sources from Zaria and environs, Nigeria. International Journal of Physical Sciences. 8(42), 1983-1987.

[23] Adeola, M.A., Isaac, R.A., 2017. Estimation of indoor Radon and its progeny in dwellings of Akoko Region, Ondo State, Southwestern Nigeria. Journal of Scientific Research & Reports. 14(3), 1-7.

[24] Jacek, P., Anna, P., Andrzej, Z., et al., 1997. Commissioning of a Quant ulus 1220™ liquid scintillation beta spectrometer for measuring ^{14}C and ^{3}H at natural abundance levels. Radiocarbon. 40(1), 201-209.

[25] United State Environmental Protection Agency, 2019. National primary drinking water regulations on Radon-222. Federal Register. 64(211), 59245-59294.

[26] UNSCEAR, 2017. 2017 Report to General Assembly, Annex A [Internet]. Available from: https://www.unscear.org/docs/publications/2017/UNSCEAR_2017_Report.pdf

BILINGUAL PUBLISHING GROUP

Advances in Geological and Geotechnical Engineering Research
https://journals.bilpubgroup.com/index.php/agger

ARTICLE

Correlation of Ground Penetrating Radar Data with Geotechnical Prospect Profiles: Reduto Case Study, Belém-PA, Brazil

***Danusa Mayara de Souza*[1*], *Lyvio Luiz Clávio de Alcântara Júnior*[2]**

[1] *Geophysics Graduate Program (CPGf), Geosciences Institute, Federal University of Pará (UFPA), Belém, Pará, 66075-110, Brazil*

[2] *Cosmopolita College, Civil Engineer, Belém, Pará, 66615-005, Brazil*

ABSTRACT

The study presented in this manuscript aimed to relate the sedimentary strata imaged by the ground penetrating radar (GPR) method through numerical modeling with the mapping of sedimentary strata acquired through geotechnical surveys. The study aimed to expose how obtaining subsoil information through noninvasive/destructive electromagnetic waves is beneficial, as they are reliable and less costly than drilling holes beyond what is necessary to have a subsurface mapping. In this sense, physical-geological modeling was carried out. The information on the type of sediments, acquired through simple recognition surveys carried out in the city of Belém-PA, helped to create a model of a sedimentary package with its respective intrinsic physical properties. The result shows that the GPR recovered with good vertical and horizontal resolution at the beginning and end of the layers of the sedimentary package studied, proving to be very effective for locating geotechnical sounding points and safely reducing costs.

Keywords: Geotechnical prospecting; Ground penetrating radar; Numerical modeling

1. Introduction

The historical advance of the occupation of urban space promoted a great wave of verticalization of buildings, which became increasingly natural and every day to contain the large population contingent, increasingly growing in the city of Belém-PA [1].

The stage of designing and constructing foun-

*CORRESPONDING AUTHOR:
Danusa Mayara de Souza, Geophysics Graduate Program (CPGf), Geosciences Institute, Federal University of Pará (UFPA), Belém, Pará, 66075-110, Brazil; Email: danusa@ufpa.br

ARTICLE INFO
Received: 21 March 2023 | Revised: 22 April 2023 | Accepted: 25 April 2023 | Published Online: 30 April 2023
DOI: https://doi.org/10.30564/agger.v5i2.5579

CITATION
Souza, D.M., Alcântara Júnior, L.L.C., 2023. Correlation of Ground Penetrating Radar Data with Geotechnical Prospect Profiles: Reduto Case Study, Belém-PA, Brazil. Advances in Geological and Geotechnical Engineering Research. 5(2): 50-63. DOI: https://doi.org/10.30564/agger.v5i2.5579

dation structures is paramount among the stages of civil construction, as the total load dissipation of the structure will depend on it, especially in densely occupied residential buildings [2].

Considering this scenario, obtaining information from the subsoil, such as that obtained from geophysical measurements, which use electromagnetic waves and electrical resistivity data from the soil, is critical, primarily because it provides essential information about the geological environment at the study site. Geophysical methods are widely used for soil and subsurface investigations. These methods involve the use of the physical properties of the subsurface materials to infer their composition and structure. Some commonly used geophysical methods for soil and subsurface investigations include ground penetrating radar, seismic refraction surveys, electrical resistivity imaging, and slingram.

The Ground Penetrating Radar (GPR) method involves using a radar antenna that emits high-frequency electromagnetic waves, typically 10 to 1000 MHz, propagating through the subsurface materials. The waves reflect the surface when they encounter a boundary between materials with different dielectric properties. By analyzing the amplitude, phase, and time delay of the reflected waves, it is possible to infer the subsurface materials and objects' depth, location, and properties. The GPR method can also create two- or three-dimensional images of the subsurface materials and objects.

The seismic refraction method uses a seismic source, such as a sledgehammer or a small explosive, to generate seismic waves propagating through the subsurface materials. The waves are detected by a series of geophones placed along a line on the surface. By analyzing the travel time and velocity of the seismic waves, it is possible to infer the depth and composition of the subsurface materials. The seismic waves refract or bend at the interfaces between materials with different seismic velocities, allowing the determination of the depth and thickness of each layer.

The electrical resistivity imaging (ERI) method involves using a series of electrodes placed on the ground surface and an electrical current source that injects a current into the ground through the electrodes. The resulting electrical potential is measured by a series of receiver electrodes, which are also placed on the ground surface. Analyzing the voltage and current data makes it possible to infer the electrical resistivity of the subsurface materials. The resistivity data can then be used to create two- or three-dimensional images of the subsurface materials, showing variations in their resistivity properties.

The Slingram method involves the use of a transmitting coil and a receiving coil. The transmitting coil generates an electromagnetic field that penetrates the subsurface materials. If there is a conductive object in the subsurface, it will affect the electromagnetic field and induce a secondary electromagnetic field that is detected by the receiving coil. For more details about geophysics methods [3-7].

The delimitation of layers and information about the beginning and end of different lithologies and soil strata through the response to electromagnetic stimuli is a great advantage, especially because geophysical methodologies are nondestructive and noninvasive and can be carried out quickly and often free of charge (under an agreement with the university to provide service to the community).

At the discretion of compliance, standardization, and mainly technical responsibility, the engineer carries out at least one survey of simple soil recognition for building foundations every 200 m^2 of the projected area in the plan before executing any building up to 1200 m^2 of area, see ABNT NBR 8036 [8]. However, in small works and even to reduce costs, it is common for some professional engineers to choose to minimize costly steps, such as geotechnical investigation, which, in turn, can result in unnecessary expenses with foundations or with the recovery of structures and settlements beyond those foreseen [9,10].

The use of GPR in engineering studies can be considered advantageous in the application of geophysics, as it allows the execution of continuous and high-resolution profiles, presents ease of data acquisition, performs measurements with different frequencies, and has the versatility of the equipment

in the field, allowing its application even in urban areas and inside buildings. Compared to other investigation techniques, this method has a low cost-benefit ratio combined with the speed of execution. GPR numerical modeling is well established, with several works and studies published [11], which bring the state of the art of methodology to various fields of knowledge, including engineering.

Considering the previous events, the present work seeks to elucidate how and to what extent geophysical methodologies, particularly GPR and numerical modeling, can assist engineering in identifying geological features and bedding in the subsurface. The lack of prior knowledge about the typology of underground sediments in areas where it is intended to build buildings, mainly vertical ones, before carrying out direct studies such as the standard penetration test (SPT), combined with insufficient information about subsurface geology, can generate mistakes in the location of underground studies. It generates a lack of essential data for the designer, which, in turn, can lead to errors in the dimensioning of foundations, generating oversizing (in the case of the insertion of safety margins beyond the necessary ones), settlements (from insufficient sizing), and pathologies (from different origins). For more information about subsurface anomalies and their detection [12,13]. The present study aims to obtain information on the subsurface from indirect and nondestructive measurements, which use electromagnetic waves and information on electrical soil resistivity, to correlate the strata described by geophysical methodologies with the strata mapped by SPT soundings.

2. Materials and methods

2.1 Standard penetration test

The ABNT NBR 6122 [14] establishes that any building must undergo preliminary geotechnical investigations of at least percussion soundings. The Standard Penetration Test (SPT) provides information on the stratigraphy and lithological classification of soils, groundwater level, and measurements of penetration resistance indices according to ABNT NBR 6484 [15] and soil classification according to ABNT NBR 6502 [16]. The ABNT NBR 6484 [15] defines the SPT drilling procedure as follows: The drilling and dynamic driving of a standard sampler every meter result in the determination of the type of soil and a resistance index, as well as the observation of the water level inside the borehole. For the definition of these results, this standard incorporates two test systems: The manual system and the mechanized system. The two systems will give different resistance index results.

As a rule, the process is divided into stages, the first being the collection of the soil sample (zero level). Then, the excavation stage begins, in which a manual auger is usually used to remove the soil sample (zero level). Then, the excavation stage begins, in which a manual auger is usually used. Then, the insertion of the sampling rod is initiated using a manual or mechanical hammer. The descent of the rod occurs in three stretches of 15 cm, totaling 45 cm. The initial 15 cm is discarded for measurement purposes, and only the final 30 cm of soil penetration is considered ABNT NBR 6484 [15].

The SPT is performed (manual test method) using a trephine (rod with a bevel at the end) that promotes the perforation and deterioration of the soil layers and removes debris removed through water circulation. When the depth to be analyzed is reached, the sampler is inserted at the end of the rod in place of the trepan, and a typical weight (65 kg) is used as a hammer. The number of blows required to reach 45 cm (15 cm initial and 30 cm final) must be counted to calculate the Nspt. **Figure 1** shows a schematic drawing of how a manual SPT probe is performed.

According to the ABNT NBR 6484 [15] standard, as the sampler is introduced, in addition to providing Nspt, soil samples are collected and stored for later geological classification. At this stage, the depth of the water level and the thickness of each sediment layer (beginning and end) are also measured. In Belém, manual geotechnical surveys are the most common [18,19]. **Figure 2** depicts a photographic record of the manual execution of an SPT sounding in a city lot.

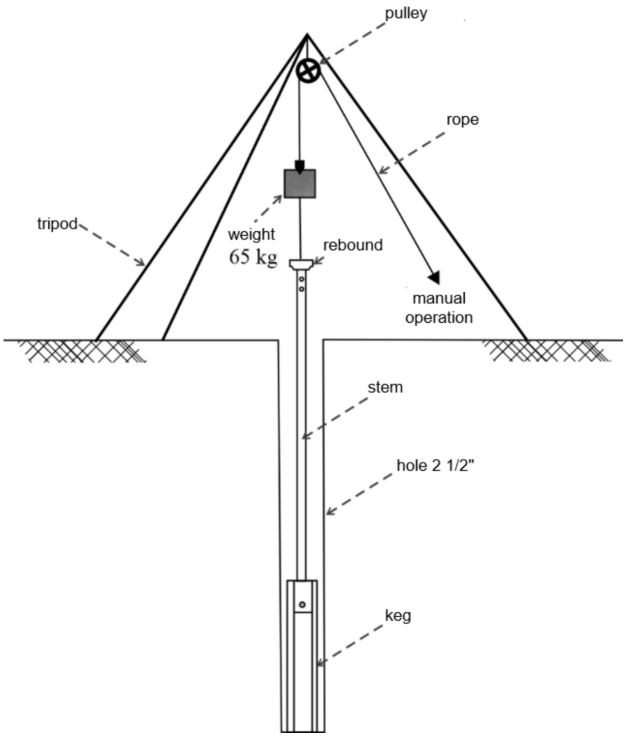

Figure 1. Schematic drawing of manual SPT sounding [17].

Figure 2. Photographic record of the manual SPT drilling process in the field.

2.2 Ground penetrating radar

Ground Penetrating Radar (GPR) is a geophysical method based on the propagation of high-frequency ElectroMagnetic (EM) waves. Practically speaking, EM energy waves are emitted from a transmitting antenna from 10 MHz to 1 GHz. When the EM wave reaches the interface between geological materials with different physical properties, part of its energy is reflected toward the surface, where it is captured by the same antenna or a second receiving antenna [20]. The propagation of the subsurface radar signal depends on the frequency of the emitted signal and the electrical properties of the medium. In the case of geological materials, the electrical properties are mainly controlled by the mineralogy of the constituents, the presence of clays, the content of metallic minerals, and the water content. If there is a contrast in at least one of the physical properties (electrical conductivity σ, dielectric constant K, and magnetic permeability μ) of subsurface materials, part of the signal is reflected and received by the receiving antenna that directs the signal received from underground to the receiver [20,21].

The resulting section, the radargram, is formed by each trace (scan) representing the arrival time of the

reflected pulses, the pulse transmitted through the air, and the direct wave propagating through the ground. Early reflections appear later (or more significantly) in the scan. As the antenna is moved over the terrain, different scans are recorded at different points. The set of scans positioned side by side (**Figure 3**) in the sequence of their acquisitions forms an image, which is a display analogous to a magnetic resonance image performed in humans, changing the composition of the EM field from a magnetic field (Hx, Hy, and Hz) that GPR uses to image to mainly the electric field (Ex, Ey, and Ez) [22].

The depth of the reflection interfaces can be obtained from the radargram, thus facilitating the interpretation of the profile and providing an approximate location of the targets. For this, it is necessary to know two parameters: the transit time between the beginning of propagation and the arrival of the reflected wave and the propagation velocity of the wave; for more details [23]. The data collection procedure is straightforward, as illustrated in **Figure 4**, which shows a photographic record of surveys conducted in the city.

In the present study, the analysis and modeling were carried out in an area in the Reduto neighborhood (in this work, it will be treated as Report RE-001). The region was chosen because the neighborhood of Reduto has a high population density and areas with deep foundations [18,19]. The area has three boreholes that are not aligned laterally and a slightly uneven topography (a level similar to that of the street) (**Figure 5**).

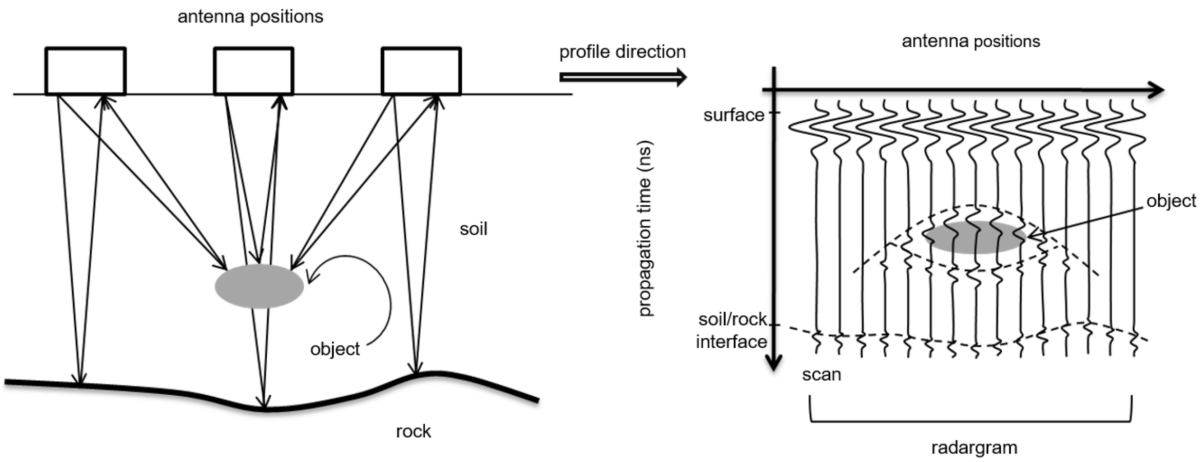

Figure 3. Exemplification of a GPR survey and a radargram [20].

Figure 4. Photographic record of the profile organization process and data acquisition with GPR.

The individual profiles of the holes show a good lateral correlation of the sedimentary layers with each other when placed side by side. Therefore, **Table 1** presents the primary information contained in drilling report RE-001.

Profile SP 01, in which excellent resistance to penetration is noted in a few meters of sampling (15.03 m) and that from 13.70 m down, the sampler was unable to descend the last 30 cm, leaving 8 cm for 46 blows, 5 cm for 49 strokes, and 3 cm for 55 strokes. The three asterisks (***) in the Nspt description indicate that the sampler could not exceed the initial 30 cm, as shown in **Figure 6**.

The sequence of sedimentary layers corresponds to the second hole, although the holes are not parallel. As in SP 01, borehole No. 02 ends at 15.05 m and has a resistant layer of thick white sand impenetrable to the standard sampler, descending only 5 cm in 58 strokes at the end of the borehole, as shown in **Figure 7**.

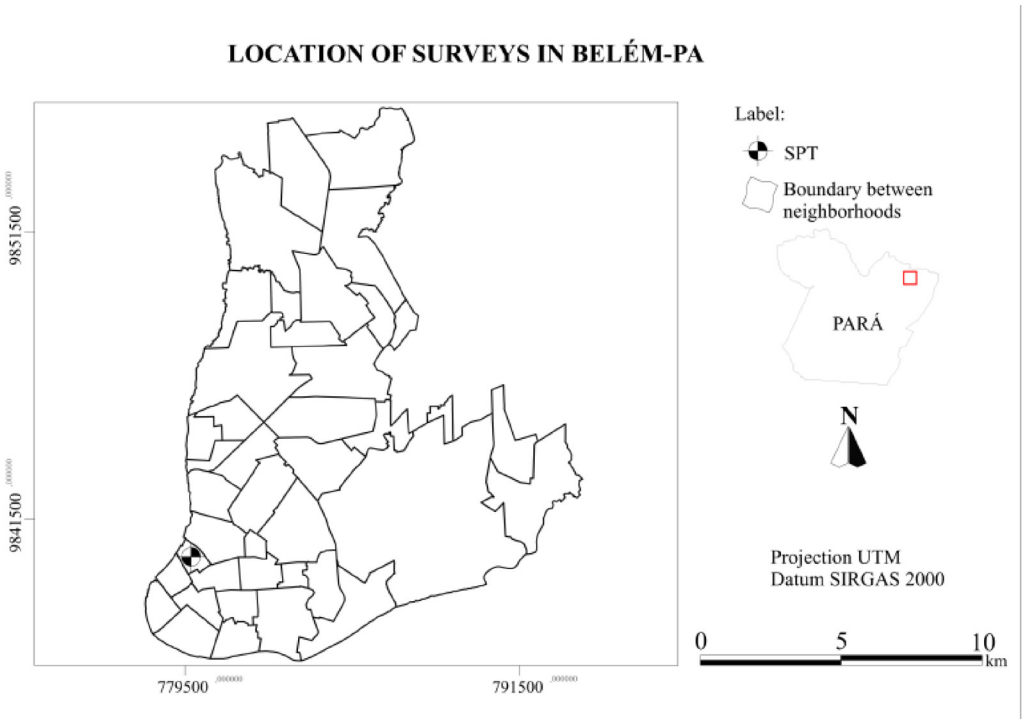

Figure 5. Location map of SPT Reduto reports in the city of Belém/PA.

Table 1. Organization of the information in the SPT RE-001 report.

SPT—REDUTO								
SP01	**prof**	**Nspt**	**SP02**	**prof**	**Nspt**	**SP03**	**prof**	**Nspt**
Variegated colored clayey silt	01,70	4	Variegated colored clayey silt	02,50	3	Variegated colored clayey silt	02,80	3
Light gray silty clay	02,80	6	Light gray silty clay	04,70	6	Light gray silty clay	03,90	14
Medium light gray sand	05,40	8	Medium light gray sand	06,30	8	Medium light gray sand	05,60	10
Variegated colored silty clay	13,70	7	Variegated colored silty clay	13,80	8	Variegated colored silty clay	13,50	7
Coarse white sand	15,03	55***	Coarse white sand	15,05	58***	Coarse white sand	15,08	55***

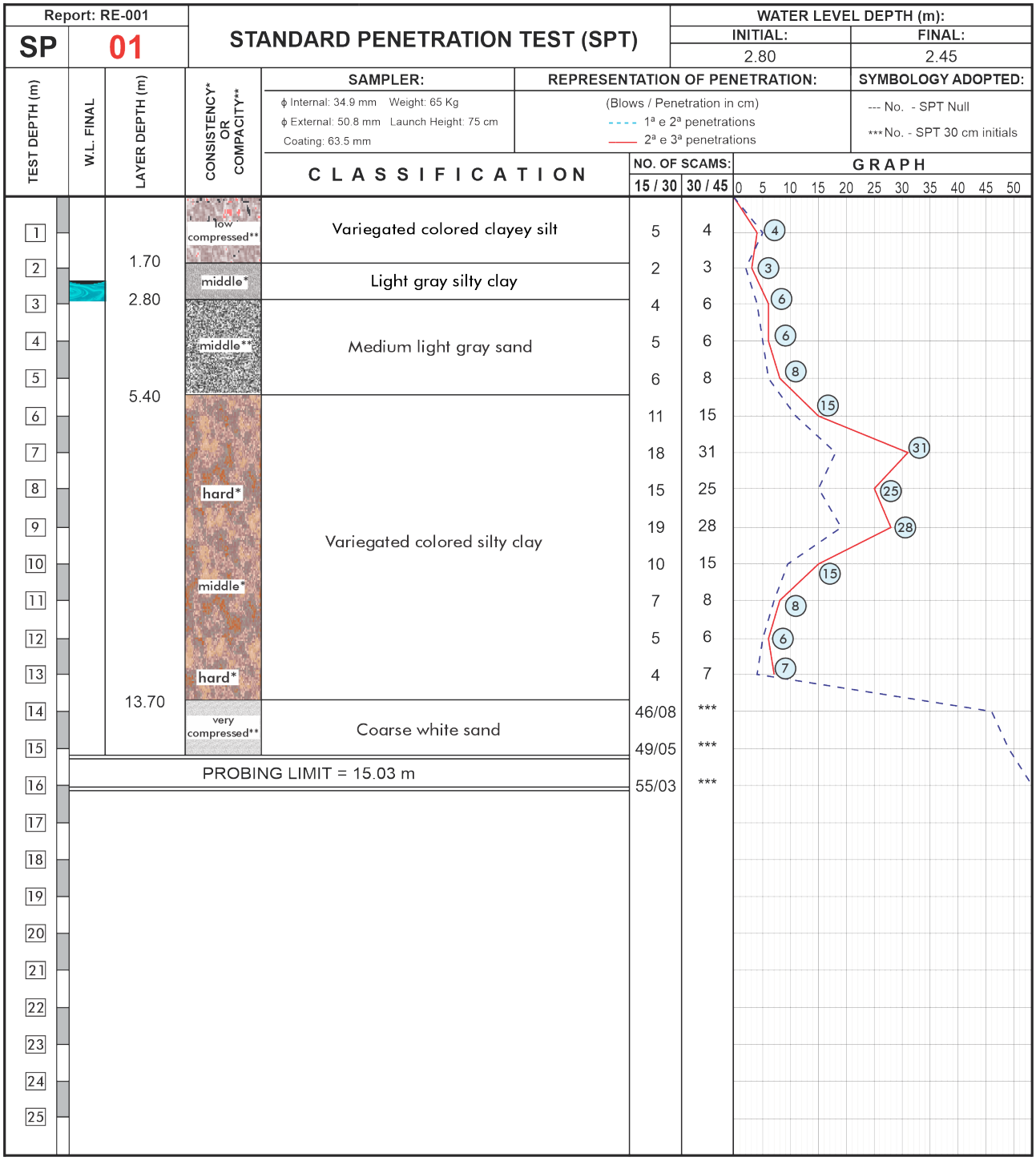

Figure 6. SP-01 of the RE-001 report.

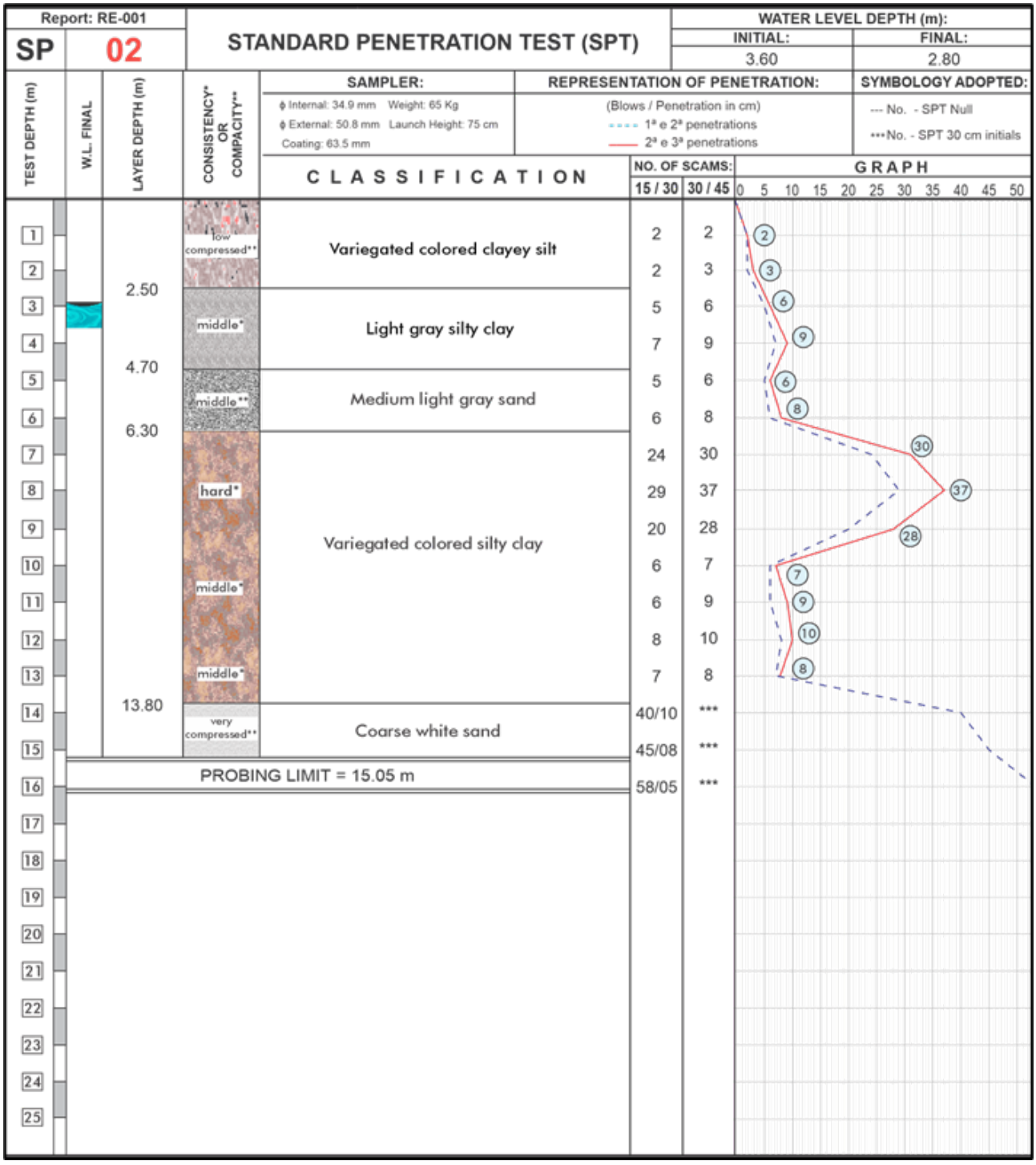

Figure 7. SP-02 of the RE-001 report.

Next, in the third hole SP 03, the lateralization of the layers is maintained, as shown in **Figure 8**.

The correlation between the layers can be seen more clearly in **Figure 9**, which illustrates the aforementioned lateral continuity by observing the description of the sequence of the layered sediments.

With the framework of information obtained from the SPT drillings, the modeling stage began, in which both geotechnical and physical information was inserted into the modeling software. The models used here were made in Reflex software to analyze the behavior of the electromagnetic field and the electrical properties that simulate a GPR survey. Modeling begins with the insertion of information about layer thickness (top and bottom depth), physical properties (σ, k[ε], and μ), and sediment type to form a data matrix in which each element (i, j) corresponds to information. Completing the modeling stage, correlating the information between the geotechnical soundings and the responses of the GPR profiles, which combine geological information with the inserted physical properties, began.

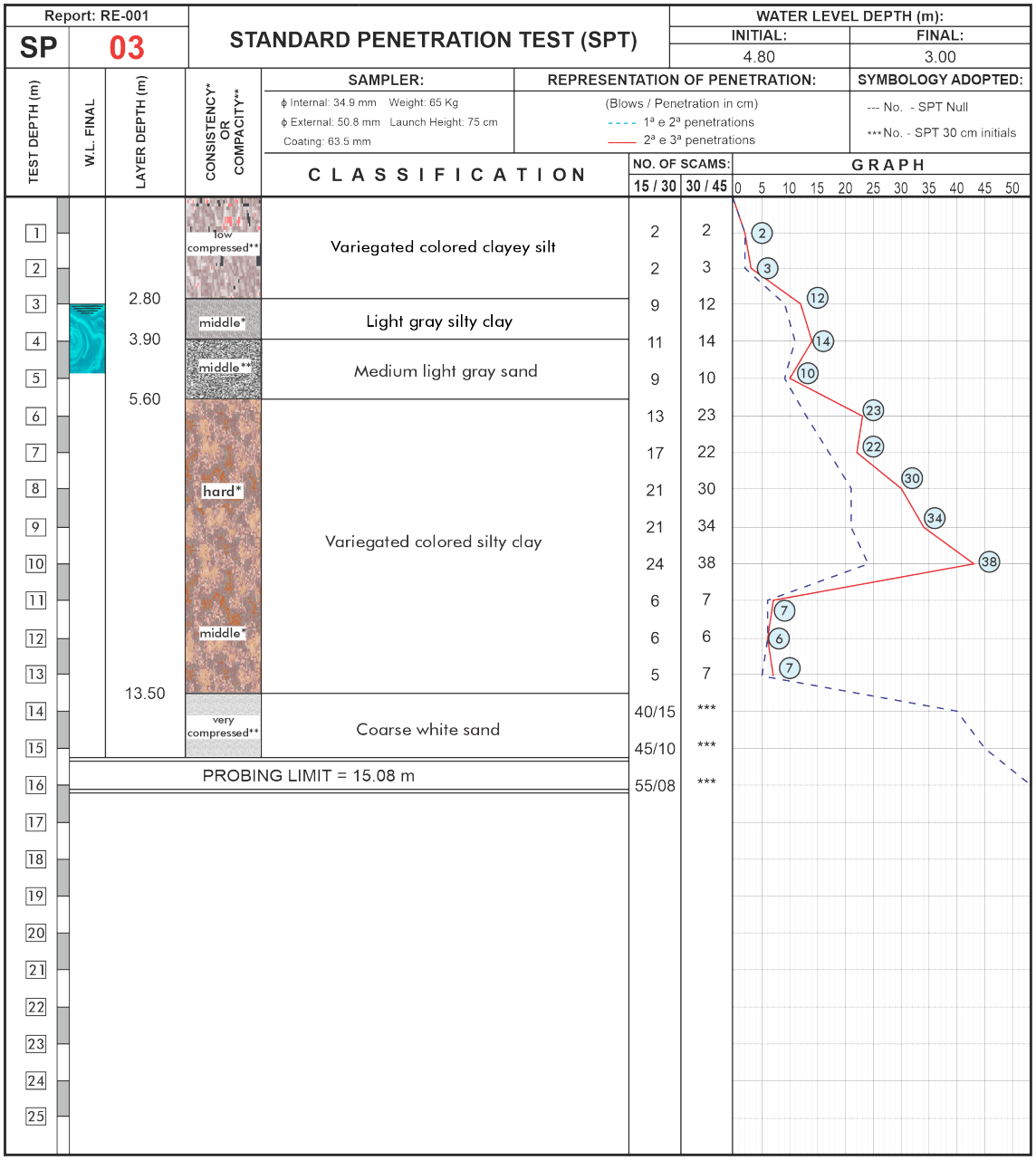

Figure 8. SP 03 of the RE-001 report.

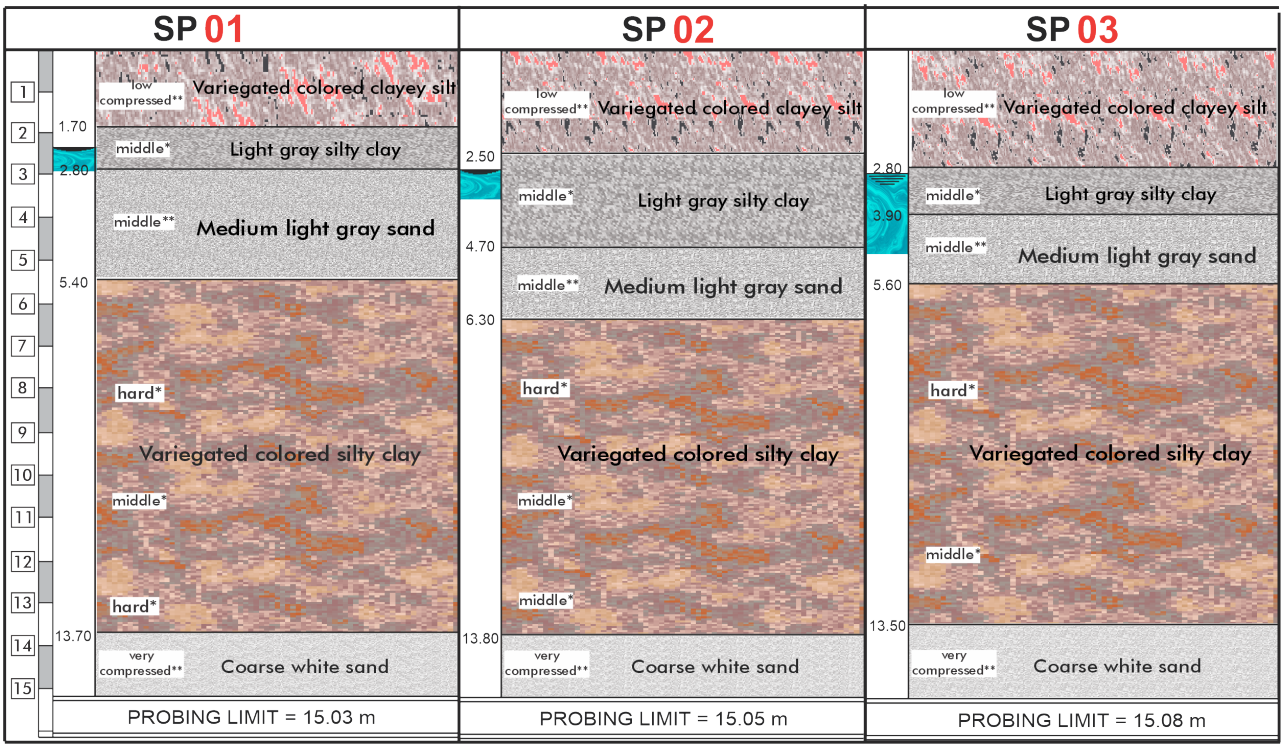

Figure 9. SPT profiles No. 01, No. 02, and No. 03—RE-001.

3. Results and discussion

Aiming to minimize errors in the dimensioning of foundations due to erroneous information about the subsurface region, the present work uses numerical modeling resources to simulate the behavior of different types of sediments and degrees of water saturation through electromagnetic stimulation, similar to a conventional GPR campaign.

Figure 10 shows the graphical interface of the Reflex software by Sandmeier [24] with physical parameters enabled. Entering layer information is simple to carry out. It defines the initial and final depth data in the "layer" field and the respective values of electrical conductivity, dielectric constant/electrical permittivity, magnetic permeability, and lateral extension.

The right part of **Figure 10** shows the configurations of the boundary conditions (absorbing edges), which prevent the energy emitted by the antenna from reverberating at the edges and contaminating the model. The source type (plane wave) establishes that the electromagnetic wavefront will arrive in each layer as a plane, thus disregarding its spherical aspect (simplification). The Kuepper signal simulates GPR equipment, and the wave propagation direction (Ey component) is from the transmitting antenna to the geological environment.

With the completion of the setting and configuration of the electromagnetic characteristics of the simulation, tomography (generation of multiple scans, called a "radargram") is generated and can be seen in **Figure 11**.

The scale on the left in **Figure 11** represents the propagation velocity window of the EM wave in the geological medium (m/ns); the scale in the upper center represents the distance (m) or length from SP 01 to SP 03, which is 10 m; and the correct scale represents the depth (m) of the layers, which can reach 15.08 m. Using interpolation, a three-dimensional model (**Figure 12**) was created with the information obtained from modeling the GPR response.

Analyzing the radargram, it is clear that the presence of saturated clay (clayey sediment with the presence of water in its pores) attenuated the propagation of the electromagnetic wave in an accelerated way, causing a fading of it in the deeper layers, even though these are composed of sand. More studies on the effects of clay presence on the attenuation of

GPR data [25-28]. This behavior is consistent with what is observed in the literature and real-world surveys carried out in other studies. This is because clay has high electrical conductivity and causes a large part of the energy sent to the medium to be absorbed and dissipated along the top of the layer.

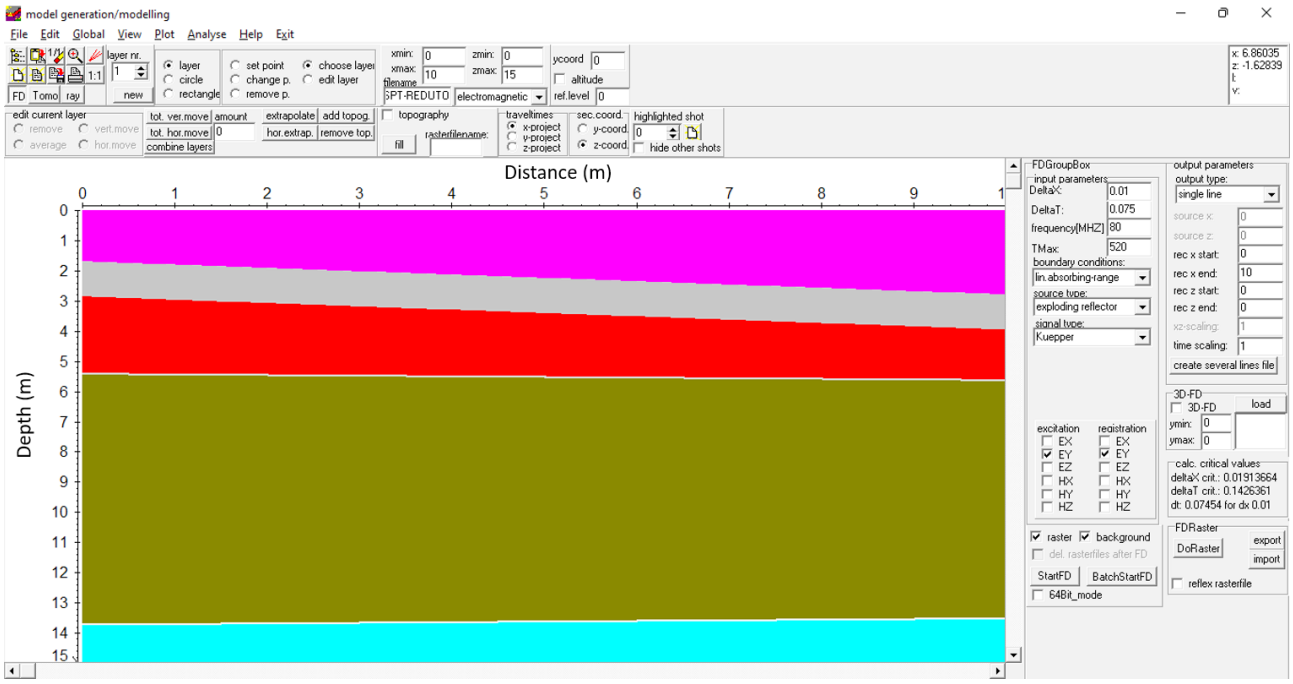

Figure 10. Information from the geological model of SPT RE-001 is being inserted into Reflex.

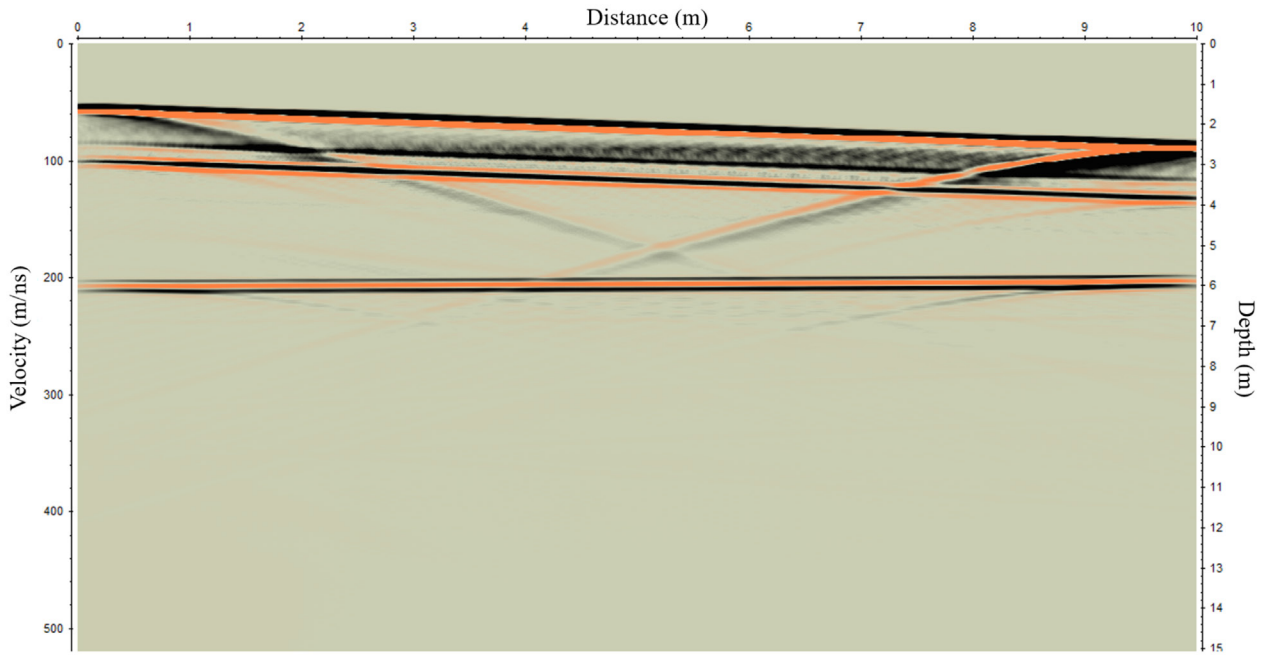

Figure 11. GPR response for the geological model of SPT RE-001.

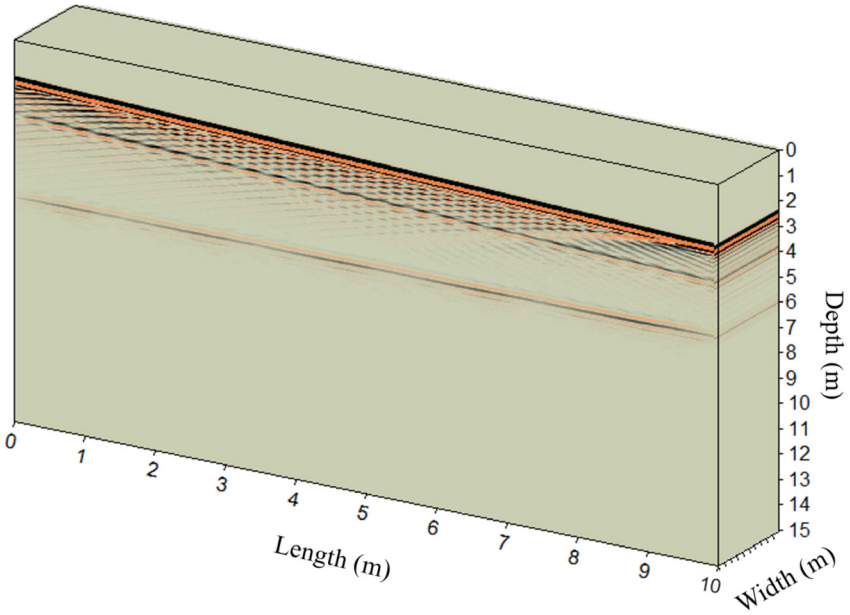

Figure 12. Data cube with the GPR response for the SPT RE-001 geological model.

4. Conclusions

By analyzing the results obtained with numerical modeling of the ground penetrating radar (GPR) geophysical method and correlating them with profiles of SPT soundings carried out in the city of Belém-PA, it was possible to create a correspondence between the geophysical responses and the geological environment in the subsurface. In short, it was possible to delimit the layers and obtain information about the beginning and end of different lithologies and soil strata by responding to electromagnetic stimuli.

Based on the boreholes, which even showed excellent lateral correlation with layers practically parallel and Nspt relatively equal, the response of the GPR modeling proved to be very effective since it recovered with good vertical and horizontal resolution at the beginning and end of layers. However, the presence of clay slowed the wave's arrival in deeper regions.

Although GPR modeling has fulfilled the role for which it was designed very well, it should be noted that it does not provide direct information on the mechanical strength of the layers and, therefore, should not be the only means for verifying the sedimentary package. The soil layers must be confirmed with SPT soundings, which will tie the information together.

Another essential aspect observed during this study is that the lithological description present in the geotechnical drilling bulletins refers to the sediments recovered by the sampler as sand, silt, and clay, as well as their variations: Silty sand and clayey sand, sandy silt and silt clayey, sandy clay and silty clay, not including the presence of other fragments such as pebbles and various materials buried in the soil. Such a description in the eyes of the GPR only refers to the size of the grains found and not their mineralogical composition per se, which generates extreme ambiguity in situations where different types of materials, as well as their proportions and water content, can produce electromagnetic anomalies that are very similar. The realization of the more practical survey in the study area is intended shortly, with the use of 250 MHz, 400 MHz, and 700 MHz antennas to verify the underground response to different operating frequencies.

Author Contributions

The first author acquired GPR data, accompanied the SPT survey in the field, built the numerical mod-

el, and wrote the manuscript. The coauthor supervised the data and revised the text of the manuscript.

Conflict of Interest

The authors declare not to have any conflict of interest.

Funding

This research received no external funding.

Acknowledgment

The authors are thankful to the CPGf/UFPA, Cosmopolita College, and his fellow professors of the Civil Engineering course, Glauciane Santos da Silva and Clementino José dos Santos Netto.

References

[1] Mello, F., 2007. A Verticalização em Belém do Pará: Um Estudo das Transformações Urbanas e Arquitetônicas em Edifícios Residenciais Multifamiliares (Portuguese) [Verticalization in Belém of Pará: A study of urban and architectural transformations in multifamily residential buildings] [Master's thesis]. Brazil: Universidade Federal do Rio de Janeiro.

[2] Carvalho, L.M.D., 2019. Fundações superficiais: controle de concepção e execução para evitar manifestações patológicas nas edificações (Portuguese) [Surface foundations: Design and execution control to avoid pathological manifestations in buildings][Bachelor's thesis]. Brazil: Universidade Federal Rural do Semi-Árido.

[3] Rahnema, H., Mirassi, S., Dal Moro, G., 2021. Cavity effect on Rayleigh wave dispersion and P-wave refraction. Earthquake Engineering and Engineering Vibration. 20, 79-88.

[4] Mirassi, S., Rahnema, H., 2020. Deep cavity detection using propagation of seismic waves in homogenous half-space and layered soil media. Asian Journal of Civil Engineering. 21(8), 1431-1441.

[5] Rahnema, H., Mirasi, S., 2012. Seismic and geotechnical study of land subsidence and vulnerability of rural buildings. International Journal of Geosciences. 3(04), 878.

[6] Bahia, V., Luiz, J.G., Fenzl, N., et al., 2009. A subsuperfície rasa na área do Parque Ambiental de Belém: Estudo a partir de dados geofísicos e de poços (Portuguese) [The shallow subsurface in the Parque Ambiental de Belém area: Study based on geophysical and well data]. Brazil: Contribuições À Geologia da Amazônia. 1ed Belém-PA. 6, 183-192.

[7] do Nascimento, C.T.C. (editor), 2011. Determinação da estrutura vertical de latossolos usando sondagens elétricas verticais (Portuguese) [Determination of the vertical structure of latosols using vertical electrical soundings]. 12th International Congress of the Brazilian Geophysical Society; 2011 Aug; the Netherlands: European Association of Geoscientists & Engineers. p. 264.

[8] ABNT NBR 8036, 1983. Programação de sondagens de simples reconhecimento dos solos para fundações de edifícios (Portuguese) [Programming of simple soil recognition probes for building foundations]. Brazil: Brazilian Association of Technical Standards.

[9] Marcelli, M., 2007. Sinistros na Construção Civil—Causas e soluções para danos e prejuízos em obras (Portuguese) [Claims in civil construction—Causes and solutions for damages and losses in works]. PINI: Brazil. pp. 270.

[10] Sena, G., Nascimento, M., Nabut Neto, A., 2020. Patologia das Construções (Portuguese) [Construction pathology]. Ekoa Educação: Brazil.

[11] Guizzi, F.T., Leucci, G., 2018. Global research patterns on ground penetrating radar (GPR). Surveys in Geophysics. 39, 1039-1068.

[12] Moradi, M., Rahnema, H., Mirassi, S., 2022. Detecting the depth and thickness of weak layer in soil media using phase velocity spectrum and theoretical dispersion curve of Rayleigh wave. Iranian Journal of Geophysics. 16(3), 57-77.

[13] Rahnema, H., Mirassi, S., 2014. Crisis man-

agement concerning underground water falling and land subsidence occurrence in the plains of Iran. Advances in Environmental Biology. 1453-1466.

[14] ABNT NBR 6122, 2019. Projeto e execução de fundações (Portuguese) [Design and execution of foundations]. Brazil: Brazilian Association of Technical Standards. Available from: https://docente.ifrn.edu.br/valtencirgomes/disciplinas/construcao-de-edificios/nbr-06122-1996-projeto-e-execucao-de-fundacoes

[15] ABNT NBR 6484, 2020. Solo—Sondagem de simples reconhecimento com SPT—Método de ensaio (Portuguese) [Soil—Single reconnaissance sounding with SPT—Test method]. Brazil: Brazilian Association of Technical Standards. Available from: https://engenhariacivilfsp.files.wordpress.com/2014/11/spt-metodo_de_ensaio_nbr_6484.pdf

[16] ABNT NBR 6502, 1995. Solos e Rochas (Portuguese) [Soils and rocks]. Brazil: Brazilian Association of Technical Standards. Available from: https://engenhariacivilfsp.files.wordpress.com/2015/02/abnt_nbr_06502_-_1995_-_rochas_e_solos_-_terminologia.pdf

[17] Wanderley, G.S.M., 2017. Desenvolvimento de Aplicativo para Relatório de Sondagem SPT na Plataforma Android (Portuguese) [Application development for SPT survey report on the android platform] [Bachelor's thesis]. Brazil: Universidade Federal da Paraíba.

[18] Salame, A.M., 2003. Mapeamento das Fundações mais usadas na Cidade de Belém—PA (Portuguese) [Mapping of the most used Foundations in the City of Belém—PA] [Master's thesis]. Brazil: Universidade Federal do Pará.

[19] Vieira, M., Alves, C., Ferreira, V., et al., 2021. Modelagem de propriedades geológico-geotécnicas em solos de Belém do Pará (Portuguese) [Modeling of geological-geotechnical properties in soils of Belém do Pará]. Research, Society and Development. 10(2), 1-15.

[20] Utsi, E.C., 2017. Ground penetrating radar: Theory and practice. Elsevier: Oxford. pp. 224.

[21] Daniels, D., 2004. Ground penetrating radar. The Institution of Engineering and Technology: London. pp. 752.

[22] Jol, H., 2009. Ground penetrating radar: Theory and applications. Elsevier: Amsterdam. pp. 544.

[23] Ida, N., 2015. Engineering electromagnetics. Springer: New York. pp. 1062.

[24] Sandmeier, K.J., 2016. ReflexW Version 8.1. program for processing of seismic, acoustic or electromagnetic reflection, refraction and transmission data. Software Manual, Karlsruhe, Germany. p. 628.

[25] Ryazantsev, P.A., Hartemink, A.E., Bakhmet, O.N., 2022. Delineation and description of soil horizons using ground-penetrating radar for soils under boreal forest in Central Karelia (Russia). CATENA. 214, 106285.

[26] Sestras, P., Bilașco, Ș., Roșca, S., et al., 2022. Multi-instrumental approach to slope failure monitoring in a landslide susceptible newly built-up area: Topo-Geodetic survey, UAV 3D modelling and ground-penetrating radar. Remote Sensing. 14(22), 5822.

[27] Carrive, P., Saintenoy, A., Léger, E., et al., 2022. Exploiting ground-penetrating radar signal enhancements by water-saturated bulb surrounding defective waterpipes for leak detection. Geosciences. 12(10), 368.

[28] Elshaboury, N., Mohammed Abdelkader, E., Al-Sakkaf, A., et al., 2023. A critical review and bibliometric analysis on applications of ground penetrating radar in science based on web of science database. Engineering. 4(1), 984-1008.

BILINGUAL PUBLISHING GROUP

Advances in Geological and Geotechnical Engineering Research

https://journals.bilpubgroup.com/index.php/agger

ARTICLE

Radio Direction Finding Method to Mitigate Tsunami Risk in Sierra Leone

***Valentino Straser*[1*], *Daniele Cataldi*[2], *Gabriele Cataldi*[2]**

[1] *Faculty of Agriculture, University of Makeni, Fatima Campus, Makeni, 00232, Sierra Leone*

[2] *Group Radio Emission Project, Lariano, Rome, 00076, Italy*

ABSTRACT

In this study, the Radio Direction Finding method is proposed for the detection of electromagnetic signals, in the VLF band, to try to anticipate the occurrence of potentially destructive geophysical events. The experimentation concerns the interception of electromagnetic anomalies in Sierra Leone, in the five-day time window, associated with seismic events that could potentially generate tsunamis. The area of investigation is Sierra Leone, whose coastline is subjected to tidal wave hazards triggered by earthquakes generated in the Mid-Atlantic Ridge. Although Sierra Leone is not affected by recurrent earthquakes, there is nevertheless a low probability, estimated at 2 percent, of the occurrence of destructive earthquakes in the next 50 years. Also in estimates, the risk of rogue and potentially damaging waves is estimated to strike the Sierra Leone coast at least once in the next 10 years. The Radio Direction Finding experiment carried out continuously 24/7, has shown a close relationship between increased radio-anomalies, in the frequencies of 6,000 Hz, a time window between electromagnetic anomaly detection and the imminence of an earthquake, and higher frequency times for the risk of earthquake occurrence in the Mid-Atlantic Ridge.

Keywords: Tsunami; Radio direction finding; Destructive earthquakes; Mid-Atlantic ridge; Sierra Leone

1. Introduction

The problem of safety and loss of life, due to large geophysical events, has been a subject of study by international research centers and universities around the world for a number of years. Potentially destructive earthquakes and catastrophic tsunamis

*CORRESPONDING AUTHOR:

Valentino Straser, Faculty of Agriculture, University of Makeni, Fatima Campus, Makeni, 00232, Sierra Leone; Email: valentino.straser@gmail.com.

ARTICLE INFO

Received: 9 March 2023 | Revised: 25 April 2023 | Accepted: 28 April 2023 | Published Online: 12 May 2023

DOI: https://doi.org/10.30564/agger.v5i2.5617

CITATION

Straser, V., Cataldi, D., Cataldi, G., 2023. Radio Direction Finding Method to Mitigate Tsunami Risk in Sierra Leone. Advances in Geological and Geotechnical Engineering Research. 5(2): 64-75. DOI: https://doi.org/10.30564/agger.v5i2.5617

have prompted the scientific community and technology to experiment with methods and make devices to intercept preseismic signals. Research that has multiplied in recent decades has shown that we are confronted with a technological limitation that hopefully can be overcome as early as the next few years. In this study, a method, Radio Direction Finding (RDF), is proposed based on intercepting electromagnetic frequencies, identifying their propagation direction and potential source. The RDF method, still undergoing experimentation and technological evolution, was devised in 2017 in Rome, Italy, by physicists Daniele Cataldi and Gabriele Cataldi. Its application has been tested on both seismic events, including potentially destructive ones, and volcanic activity monitoring. The experimentation has recently started in Sierra Leone, a geologically ancient land that is rarely affected by strong earthquakes. Precisely for this reason, Sierra Leone represents an open-air laboratory for the study of potential catastrophic scenarios, induced by geophysical events, which could affect, especially, stretches of Atlantic Ocean coastline and the capital Freetown.

1.1 The electromagnetic seismic precursors (ESPs)

The study of electromagnetic emissions associated with earthquakes is based on mechanisms for the production of radio emissions generated by mechanical deformation, and the following fracturing of rocks present in the earthquake preparation zone in the preseismic phase. Electromagnetic anomalies were observed, for example, on March 11, 2011 before the earthquake that occurred in Japan [1], or those of the Peruvian earthquake of September 25, 2013 [2], or even those recorded on August 24, 2016 in Italy [3]. These cases are just some of the earthquakes preceded by electromagnetic emissions or electromagnetic anomalies recorded on a global scale [4-8]. It was 1890 when the British geologist John Milne, inventor of the eponymous horizontal seismograph, a professor at the Imperial College of Engineering in Tokyo and founder of the Seismological Society of Japan (SSJ), in his work entitled "Earthquakes in Connection with Electric and Magnetic Phenomena" [9], described some electrical phenomena magnetic and related to seismic activity. It was the first scientific publication ever in which they described a series of electromagnetic phenomena, about one hundred years later, the international scientific community renamed as "electromagnetic seismic precursors" or ESP [10]. In 2007, Gabriele Cataldi and Daniel Cataldi founded a scientific research project (Radio Emissions Project) dedicated to monitoring and study of Electromagnetic Seismic Precursors (ESPs) and, in a few years, they have developed an innovative electromagnetic tracking method, who was able to provide valuable data on the pre-seismic electromagnetic anomalies, meaning by this term also electromagnetic phenomena of solar origin and those of geomagnetic nature [11].

1.2 Theoretical basis on pre-seismic radio emissions

The pre-seismic radio signals are generated by a series of mechanisms that occur at the level of the lithosphere (Earth's crust) which have been well known and studied for years. They are mainly emitted by the micro-fractures that are generated on the seismic fault plane when the level of mechanical stress reaches such levels as to start breaking up the rocks. Studies confirming the production of radio frequency emitted by rocks placed under mechanical stress have also been conducted in recent years thanks to the funds allocated NASA (National Aeronautics and Space Administration) [3,4].

Microfractures are small cracks in the rock which, from a geological point of view, generally have a length of a few millimeters (or less) and a width of less than 0.1mm and are formed in the phases preceding the macrofractures. Since the size of a microfracture substantially depends on the homogeneity of the rock subjected to tectonic stress, it is evident that fractures of much more varied dimensions have also been observed. The first microfractures were observed in 1850 through transmitted light microscopy (TL), while only in 1960 it was possible to observe them through scanning electron microscopy (SEM) [11]. The creation of experimentally induced

microfractures was demonstrated for the first time through triaxial compression tests [12] and currently, the study of microfractures produced in the laboratory has allowed us to provide important information on rock breaking processes and a better understanding of faults and formation of microfractures in nature [13]. Since the faults do not have a planar morphology but are irregular, they can be described graphically as a fractal [14]. This condition means that when tectonic stress accumulates, the geometric irregularities of the fault influence each other, leading to the formation of additional microfractures in the surrounding rock that has a different orientation than the main ones [15-17]. It is therefore evident that the volume of the Earth's crust involved in the creation of microfractures is larger than the area defined as the "earthquake preparation zone": According to some estimates, this volume could be between 24 and 520 times larger than the earthquake preparation area. The locally generated pre-seismic radiofrequency is an electromagnetic phenomenon caused by the tectonic stress that deforms and creates microfractures and macrofractures in the rocks present in the earthquake preparation area through the phenomenon of piezoelectricity [18]. The amplitude of the electromagnetic signals caused by the formation of microfractures of the rocks subjected to tectonic stress in the earthquake preparation area mainly depends on the density of the microfractures and their size; The morphology of the electromagnetic field depends on the orientation of the microfractures; on the other hand, the period of oscillation of the electromagnetic field (temporal modulation) depends on the geological characteristics of the fault and on the characteristics of the tectonic stress that determine a growth of the microfractures that does not proceed linearly. According to a study carried out in 2007 [19], the volume of the Earth's crust concerned issues pre-seismic electromagnetic due to the accumulation of tectonic stress, it has a much larger size than the volume of the affected Earth's crust solely on the production of micro-fractures (focal area of the earthquake). Taking as reference an earthquake of magnitude 6 and considering the volumes involved, this ratio is > 200:1. Subtracting the energy released by the seismic waves by the energy that theoretically is accumulated as a result of tectonic stress within the earthquake preparation zones, the result is that only a small part of the energy contained in the earthquake focal zone is converted into seismic waves. According to T. Lay and T. C. Wallace [20], only 1-10% of the energy and seismic moment contained in earthquake zone preparation is converted into seismic waves. It is therefore conceivable that 90% (or more) of this energy, or part of it, can be converted to radiofrequency. Taking as a reference an earthquake of magnitude 5, this has an energy and a seismic moment between 1012 Nm and 1018 Nm [20].

Over the decades, since the 1980s, the international scientific community has been concerned with the study of pre-seismic radio emissions by creating ad-hoc research projects. Some of them are listed below:

- EMSEV (Electromagnetic Studies of Earthquakes and Volcanoes). A project of the "Earthquake Prediction Research Center" of Tokai University (Japan) to promote cooperation among researchers in scientific research on earthquake prediction (2009).

http://www.emsev-iugg.org/emsev/

- EMV (Electromagnetic Variations). Greek project for monitoring electromagnetic seismic precursors active since 1987.

http://users.teiath.gr/gregkoul/

- SEMEP (Search for Electro-Magnetic Earthquake Precursors). A project established as a collaboration between the European Community and Russia in 2010 after a meeting at the Seventh Framework Programme (FP7).

https://cordis.europa.eu/project/rcn/96924/reporting/en; https://cordis.europa.eu/project/id/262005/reporting

- Pre-Earthquakes Project - The project was born out of an agreement between Italy (University of Basilicata), Germany, Turkey and Russia that dealt with the study of pre-earthquake radio emissions (2011-2012).

- iSTEP Project (integrated Search for Taiwan

Earthquake Precursor) Chinese scientific research project to study earthquake precursors (2002-2012).

T52D.08T/abstract

- Integrated Earthquake Frontier Project. Scientific project for the study of earthquake precursors created by the former Japanese Government Technology and Science Agency (JST) after the disastrous M7.3 earthquake that was recorded on January 17, 1995, in Kobe. Under this project, two agencies were sent to conduct 5 years of studies (1996-2001) on the feasibility of using electromagnetic seismic precursors: The RIKEN (Physical and Chemical Institute) and the NASDA (National Space Development Agency of Japan). This study project was named the "Earthquake Remote Sensing Frontier Project." https://ieeexplore.ieee.org/document/1177344

- SSTL (Small Satellite for Earthquake Prediction). Active between 2001 and 2003, it was the research project of the Surrey Space Center of the University of Surrey (England), dedicated to the study of ionospheric seismic precursors and carried out through electromagnetic background monitoring and space meteorology [21].

- Berkeley Seismological Lab. Scientific research laboratory at the University of California, Berkeley, under which electromagnetic seismic precursors are monitored and studied.

http://seismo.berkeley.edu

- Quake Finder Project. Scientific research project dedicated to elettromagnetic seismic precursors active since 2000 and subsidized by N.A.S.A.

https://www.quakefinder.com

- DEMETER (Detection of Electro-Magnetic Emissions Transmitted from Earthquake Regions) Satellite. First project of the French National Center for Space Studies (CNES) to study ionospheric and environmental electromagnetic anomalies preceding earthquakes. Active between 2004 and 2010.

https://demeter.cnes.fr/en/DEMETER/lien4_science.htm

- CSES (China Seismo-Electromagnetic Satellite). Project operational since 2018, established in collaboration between China and Italy to study ionospheric electromagnetic anomalies associated with destructive earthquakes. The Chinese-Italian agreement involves the launch into orbit of an artificial satellite capable of making measurements of the Earth's geomagnetic field and solar wind ionic parameters.

http://cses.roma2.infn.it

- Stanford University, Department of Geophysics. Stanford University's Department of Geophysics has created an inter-graduate course dedicated to monitoring electromagnetic seismic precursors.

- MEMFIS (Multiple Electromagnetic Field and Infrasound Monitoring Network), complex geophysical monitoring project produced by the University of Bucharest, Romania, active since 2004 [22].

- QuakeSat. Stanford University nanosatellite, launched into space in 2003 (mission ended in 2005). It was equipped with a triaxial magnetometer and an electric field sensor. Instruments specifically designed to study electromagnetic seismic precursors.

https://www.quakefinder.com/

- INFREP (International Network for Frontier Research on Earthquake Precursors). European electromagnetic monitoring network for the study of earthquake-induced ionospheric disturbances [22].

1.3 Correlation between electromagnetic waves and earthquakes

Analysis of ambient radio frequency conducted since 1890 has led to the understanding that there are natural radio emissions, with wide bandwidth, that can be observed with greater intensity in the immediate vicinity of potentially destructive earthquake epicenters [23,24]. Laboratory experiments have shown that this pre-earthquake radio frequency is generated through direct piezoelectric effect when crystalline materials in the earthquake preparation zone polarize due to tectonic stress, generating a potential difference. Electromagnetic emission starts during deformation of crystalline materials and not only during their rupture (microfractures and macrofractures).

In this context, the greater the volume of the Earth's crust included in the earthquake preparation zone, the greater will be the intensity of radio emission generated through the direct piezoelectric effect

(Epicentral Ionic Emissions or EIE—Term coined by the Radio Emissions Project in 2012) [25,26]. When these radio emissions emerge from the Earth's surface, they propagate within the Earth-ionosphere cavity and can be detected through electromagnetic monitoring stations that can identify their geographical area of origin using Radio Direction Finding (RDF) technology. This scientific approach enables crustal diagnosis by identifying areas of the Earth's surface from which broadband pre-seismic radiofrequency is emitted, making it possible to identify areas of the Earth's surface within which a seismic event may occur. Since a pre-seismic electromagnetic source cannot be considered an isotropic electromagnetic source due to the characteristics of the Earth's crust and tectonic stress, it is evident that it is more convenient to study this pre-seismic electromagnetic phenomenon through a dense network of electromagnetic monitoring stations rather than through a few stations.

1.4 The risk of geophysical and catastrophic events in Sierra Leone

Sierra Leone is a West African state located on the coast of the Atlantic Ocean bordering Guinea to the north and east and Liberia to the southeast. It has a population of about 8,421,000 as of 2021 census. Sierra Leone has a low seismic hazard but, nevertheless, there is a 2 percent probability of potentially destructive seismic tremors occurring within the next 50 years. Probabilistic assessment has indicated very long return times of major seismic events, on the order of 475, 2475, and 9975 years [27]. The risk of coastal flooding, on the other hand, is classified as high, i.e., that potentially damaging waves may inundate the Sierra Leone coast at least once in the next 10 years. In fact, the Mid-Atlantic Ridge can generate major earthquakes with magnitudes that can reach and exceed M7.1, as in the case of the strong 1982 earthquake (https://earthquakes.zone/sierra-leone). The potential damage induced by geophysical events, is an element of concern for Sierra Leone, especially in terms of coastal effects, and the consequences on society, with economic losses, damage to structures, and loss of life [28]. The long lapse of time from the occurrence of disastrous tsunamis until now induces caution and consideration of potential pitfalls for the coastal population, and the capital Freetown, in the coming years. At least from a statistical point of view.

1.5 Seismotectonics and tsunamis

Sierra Leone is included in the fourth of the six seismotectonic provinces of the West African Craton [29], formed by three Archaic and Paleoproterozoic metamorphic and magmatic shields that include the Central African fault systems of Angola, DR Congo, Cameroon, and Chad, determined by the tectonic regime [30-32]. The Mid-Atlantic Ridge earthquakes are essentially related to an extensional tectonic regime, which, however, do not rule out an interaction with magmatic activity in the Ridge [33]. Recent studies have shown that the crust of the equatorial Atlantic Ocean, with a thickness of about 5.5 km, is predominantly magmatic, ranging in age from 8 to 70 Ma. The semi-diffusion of the ridge is about 16 mm/year, fed by three mega-transform faults running east-west, St. Paul, Romanche and Chain. The St. Paul transform fault system, which is related to tectonic activities of fracture systems and earthquakes that could potentially generate tsunamis on the Sierra Leone coast, includes four minor faults that collectively extend a total of about 600 km [34]. Seismic studies of the mid-Atlantic ridge have made it possible to interpret the structure of the oceanic crust and catalog historical earthquakes to draw up a map of seismic and potentially destructive tsunami risk [35-37]. The Atlantic Ocean, except for the Lisbon tsunami of 1755, does not generate transoceanic tsunamis due to the geodynamic conditions of the Mid-Atlantic Ridge, unlike the Pacific and Indian Oceans. Instead, Atlantic Ocean tsunamis have local significance and of their impact on cities and human activities, requiring an effective warning system for high risk on the coasts [38,39].

Looking at Sierra Leone's population density data for 2000, the majority of the population is concentrated on the coast, which faces the Atlantic Ocean

where strong earthquakes and tsunamis can be produced [40].

2. Materials and methods

This study is based on electromagnetic monitoring of Sierra Leone through Italy's 24/7 Radio Direction Finding (RDF) network. The monitoring data were analyzed, modeled, and compared with the occurrence of earthquakes published on the network in real time.

The monitoring stations used for signal detection are in Italy at an average distance of about 4,900 km in the SSW direction,

1) RDF station in Pontedera, Pisa, Italy.

2) RDF station in Lariano, Rome, Italy.

The radio direction finding system

The detection system used by the research team is based on an electromagnetic monitoring system developed by the Italian Radio Emissions Project, starting in 2017. It consists of a series of electromagnetic sensors capable of detecting and recording the occurrence of electromagnetic signals of natural origin, and indicating their intensity, time duration and azimuth of origin, with respect to the geographical position of the detection station itself.

Such a network of sensors, deployed on Italian soil can triangulate radio signals emitted by a natural source, thanks to the technique of "radio triangulation", a technology from the 1920s of the last centuries, the technology of which was employed in this very project and is called Radio Direction Finding (RDF).

The RDF station, it is basically based on a series of loop antennas, positioned in orthogonal pattern, by a radio amplifier developed by Daniele Cataldi and Gabriele Cataldi, whose amplified signals are sent to the sound card of a PC, and processed there (**Figure 1**). Such a sensing system can generate an archive of dynamic and graphical spectrograms based on the electromagnetic signals detected by the antennas and of natural origin. At present, an RDF station can constantly document electromagnetic emissions from the Earth's crust (radio-nature), in the band between 0,000 Hz and 96 kHz; in this study, the electromagnetic signals monitored are those between the SELF band and the VLF band (0,000 Hz - 30 kHz). The range detected in the electromagnetic spectrum, where electromagnetic signals appear most frequently, potentially indicates a pre-earthquake signal that can anticipate strong earthquakes that can generate tsunamis [41].

Precursor signals (SEPs—Seismic Electromagnetic Precursors) are those of crustal, and local, origin, that is, generated by the Earth's lithosphere (crust), which due to the tectonic stress to which the rocks are subjected, generate electrical (ions) and electromagnetic (electromagnetic field—moving ions) emissions, which can then be picked up at a distance [7,42-44].

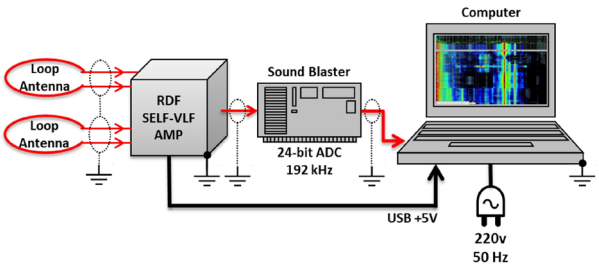

Figure 1. Schematization of the operation of an Italian RDF station, developed by the Radio Emissions Project. Credits: Radio Emissions Project.

3. Results

The electromagnetic monitoring, indicated by the RDF spectrograms with the yellow-green interference, covers the coast of Sierra Leone and, the capital Freetown, the area most exposed to tsunami risk. There were 55 spectrograms analyzed to compile the present study, in which electromagnetic signals having the monitored area as the direction of arrival were considered. The spectrogram shows an example of the data recorded by the Italian RDF network, and the azimuth of the electromagnetic signals. In this case it is an obvious signal recorded at 06:15 UTC on January 28, 2023, then terminated at 09:40 UTC on January 28, 2023. The RDF stations used for electromagnetic monitoring, carried out continuously 24/7, are those of Lariano (Rome) and Pont-

edera (Pisa), both located in Italy. The earthquakes considered in this study, with magnitude between 4.7 and 5.0, occurred in the Central Mid-Rigde of the Atlantic Ocean, in the period between January 28, 2023 and February 18, 2023 detected by the Italian RDF network (**Table 1**):

Table 1. Earthquakes list (http://earthquake.usgs.gov/).

N.	Date time (UTC)	Magnitude	Depth	Location	Region
1	2023-01-29 17:04:15.3	mb 4.9	10 km	8.63°N; 39.50°W	Central Mid-Atlantic Ridge
2	2023-02-01 03:14:25.1	mb 4.7	60 km	2.61°N; 30.85°W	Central Mid-Atlantic Ridge
3	2023-02-10 13:34:11.4	mb 4.9	10 km	7.57°N; 36.86°W	Central Mid-Atlantic Ridge
4	2023-02-12 07:08:23.6	mb 5.0	10 km	17.55°N; 46.56°W	Central Mid-Atlantic Ridge
5	2023-02-15 02:13:12	mb 5.3	10 km	8.016°N; 37.066°O	Central Mid-Atlantic Ridge
6	2023-02-15 02:14:32	mb 5.1	10 km	7.883°N; 36.988°O	Central Mid-Atlantic Ridge
7	2023-02-16 18:35:50	mb 4.6	10 km	7.576°N; 36.782°O	Central Mid-Atlantic Ridge
8	2023-02-17 02:11:31	mb 5.3	10 km	1.079°N 28.081°O	Central Mid-Atlantic Ridge
9	2023-02-18 14:07:43	mb 4.7	10 km	7.365°N 36.037°O	Central Mid-Atlantic Ridge

4. Discussion

Analysis of the electromagnetic data, in the SELF-VLF band, indicate that fluctuations in the duration (in hours) of the radio-anomalies in the RDF spectrograms can be associated with earthquakes in the monitored area, in a time window ranging from a few minutes to a little more than two hours. The RDF spectrograms show that earthquakes occur at a decrease and then by an increase in radio-anomalies, lasting several minutes. The increase in the duration of radio-anomalies is accompanied by an increase in the number of earthquakes, especially when we consider those radio signals that possess an extremely low frequency (0.001 to 3 Hz band). Data indicate that increases in the electromagnetic frequency of signals are always close (temporally) to earthquake events, in this case M4.5+ that occurred off Sierra Leone (Atlantic Ocean). The largest number of M4.5+ earthquakes occurred within a time frame in which the radio-anomalies recorded at very low frequencies presented peaks that raised these values on the order of tens of times. This is a condition that can be considered normal precisely because in this case changes in electromagnetic frequency are associated with an increase in energy accumulated at the crustal level and capable of generating more earthquakes as well as higher magnitudes. Earthquakes are associated with electromagnetic frequency of radio-anomalies, which occurs at 6,000 Hz (**Figure 2**).

The duration of radio-anomalies recorded by Italian RDF stations (**Figure 3**), expressed in minutes, shows that most electromagnetic emissions of crustal origin have a duration ranging from a few minutes to 125 minutes (average). It can be hypothesized that the variation in the duration in minutes of these electromagnetic emissions may be associated with the extent and amount of energy stored in the fault.

Another important data point is the UTC time within which radio-anomalies are emitted. **Figure 4** shows that the time at which signals are most frequently recorded is between about 04:48 UTC and about 12:24 UTC, as in the case of 3 out of 4 earthquakes that occurred in that time range.

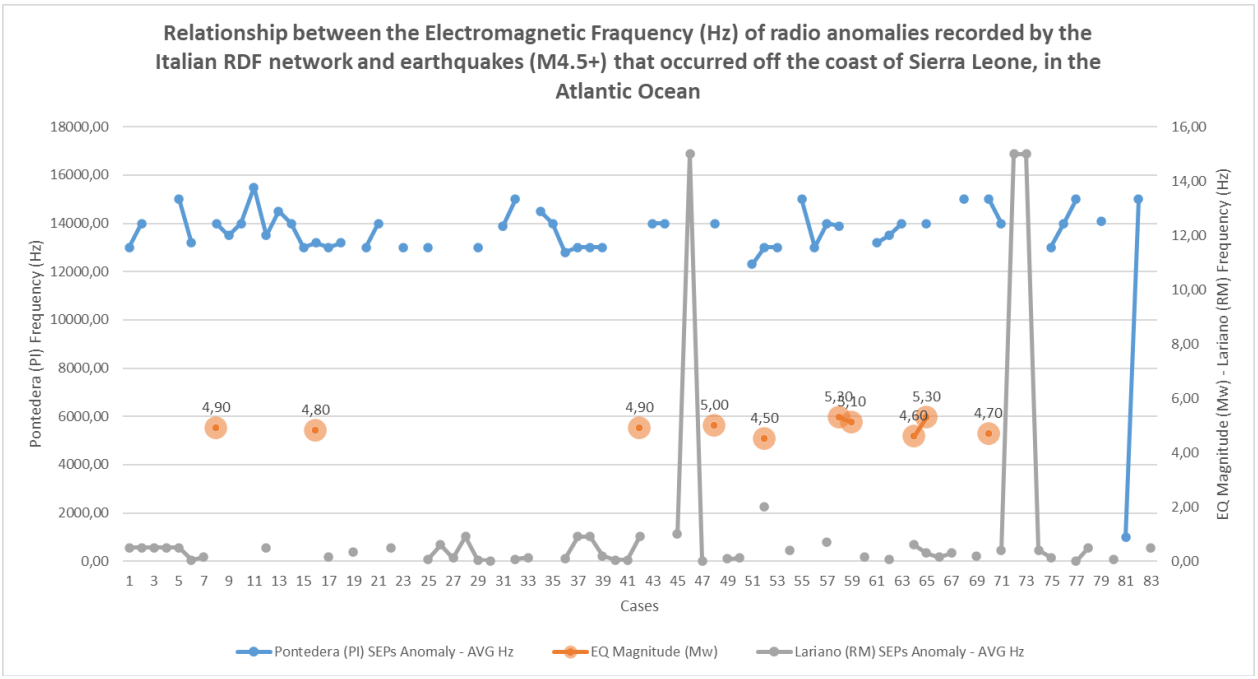

Figure 2. The graph shows the electromagnetic frequency of radio-anomalies recorded by Italian RDF stations, which appeared in the Atlantic area facing Sierra Leone, and the number of earthquakes that always occurred in the same area monitored by the Italian RDF network. Credits: Radio Emissions Project.

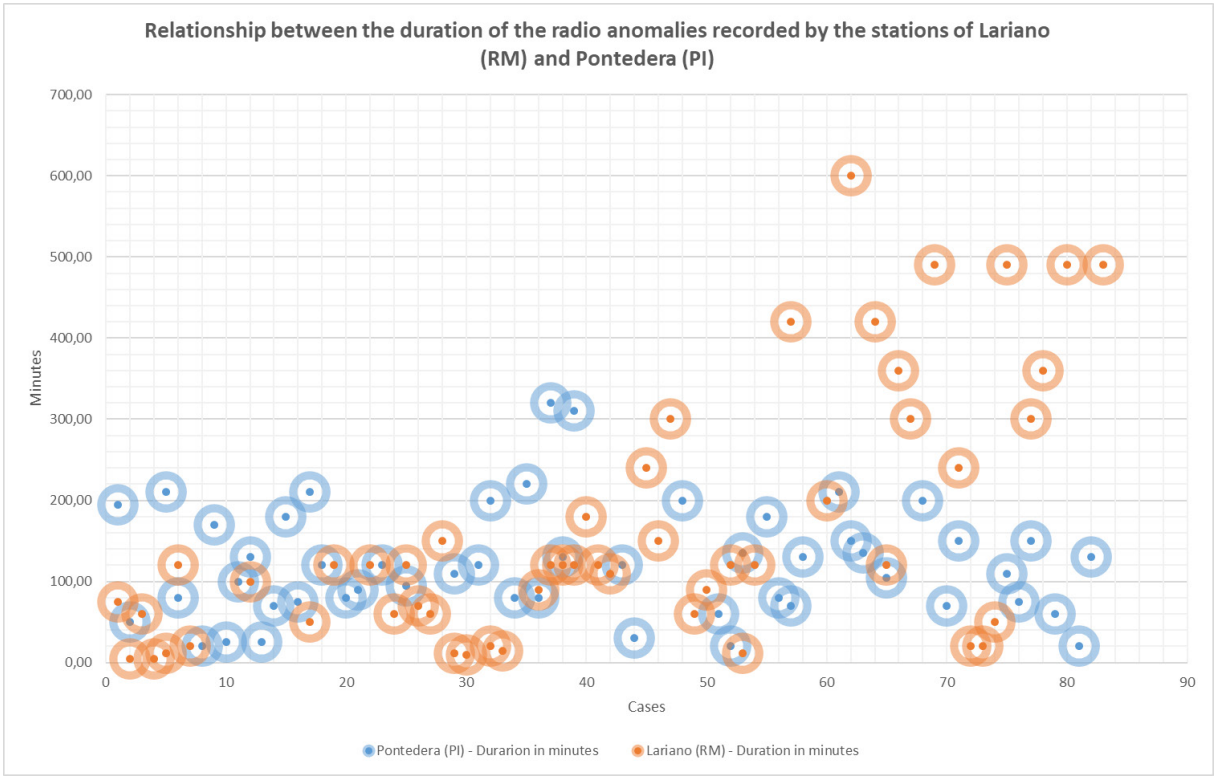

Figure 3. The graph shows the distribution of the duration in minutes of radio-anomalies recorded by Italian RDF stations. Credits: Radio Emissions Project.

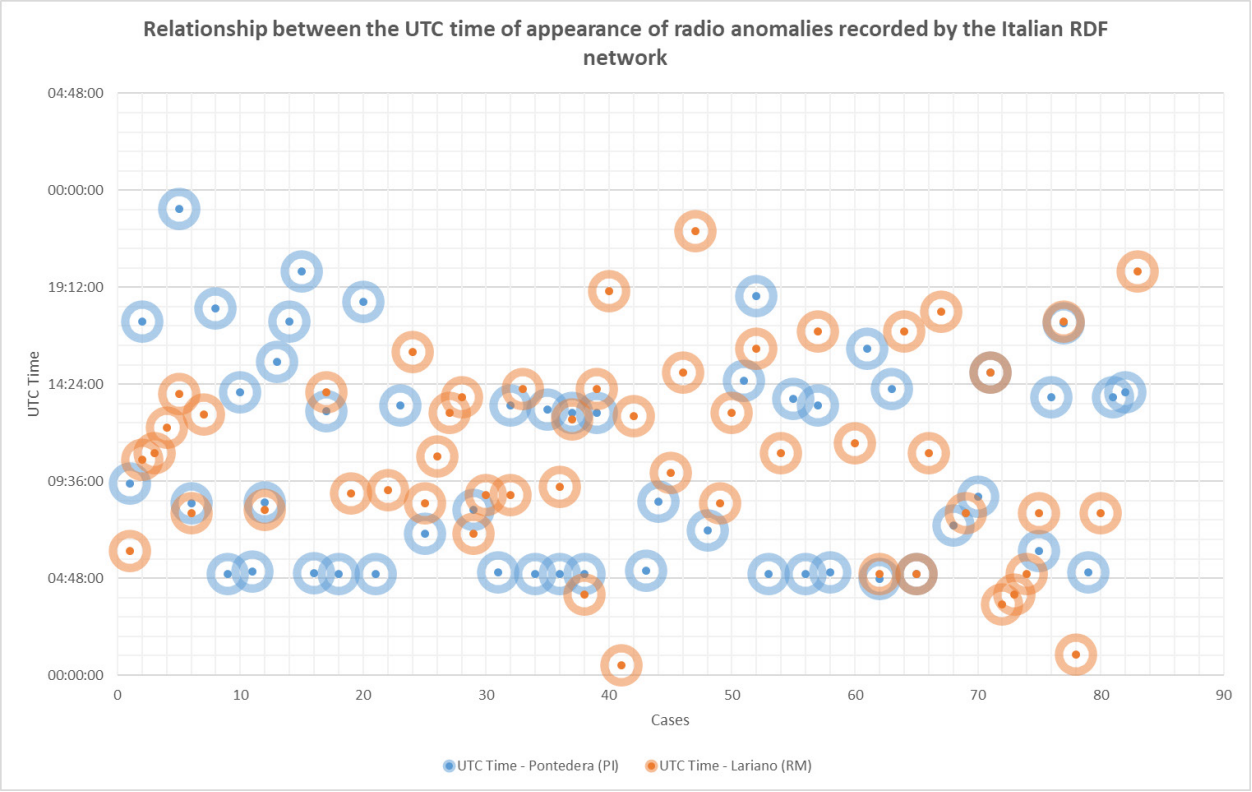

Figure 4. The graph shows the distribution of UTC time at which radio-anomalies recorded by Italian RDF stations occurred. Credits: Radio Emissions Project.

5. Conclusions

The study provided significant indications of the emission of electromagnetic signals with an azimuth of arrival located in the Atlantic area facing Sierra Leone, converging in the frequency of 6,000 Hz, the time (UTC) of occurrence of such signals, and their duration.

Analysis of the evolution of these radio emissions related the variation in the duration in minutes of these signals to the occurrence of earthquakes, as well as the average temporal location of these signals throughout the day. Knowing the time of emission of electromagnetic signals, the mechanism of which is still to be interpreted, is particularly useful in activating warning signals for the potential risk of an earthquake occurrence, especially in the area of the capital Freetown.

The present study, which is still partial due to the paucity of data to be modelled, can be enhanced in the future with the expansion of the Radio Direction Finding network by placing monitoring stations in Sierra Leone as well, supporting the Italian and Malaysian to develop warning system for the risk of strong earthquakes and tsunamis that may endanger the safety of people, especially in the centres that populate the coastal area of Sierra Leone.

Author Contributions

Valentino Straser has the main responsibility, and initiative based on several years of study of seismic precursors, especially in the electromagnetic field. The co-authors supported the present study with data collection and providing the essential devices for real-time monitoring signals Radio Direction Finding.

Conflict of Interest

The author and co-authors declare that they have no conflicts of interest.

Funding

This research received no external funding.

Acknowledgment

We express sincere thanks to Carlo Magretti for technical support in acquiring data for the preparation of this study and anonymous reviewers who enabled us to improve this paper.

References

[1] Straser, V., 2011. Radio wave anomalies, ULF geomagnetic changes and variations in the interplanetary magnetic field preceding the Japanese M9.0 earthquake. New Concepts in Global Tectonics Newsletter. (59), 78-88.

[2] Cataldi, D., Cataldi, G., Straser, V., 2014. Variations of the electromagnetic field that preceded the Peruvian M7.0 earthquake occurred on September 25, 2013. EGU General Assembly 2014; 2014 Apr 27 - May 2; Vienna.

[3] Straser, V., Cataldi, G., Cataldi, D., 2016. SELF and VLF electromagnetic signal variations that preceded the Central Italy earthquake on August 24, 2016. New Concepts in Global Tectonics Journal. 4(3), 473-477.

[4] Ohta, K., Izutsu, J., Schekotov, A., et al., 2013. The ULF/ELF electromagnetic radiation before the 11 March 2011 Japanese earthquake. Radio Science. 48(5), 589-596.
DOI: https://doi.org/10.1002/rds.20064

[5] Bernard, P., 1992. Plausibility of long distance electrotelluric precursors to earthquakes. Journal of Geophysical Research: Solid Earth. 97(B12), 17531-17546.

[6] Pulinets, S., Boyarchuk, K., 2004. Ionospheric precursor of earthquakes. Springer: Berlin. pp. 315.

[7] Straser, V., Cataldi, D., Cataldi, G., 2019. Registration of pre-seismic signals related to the mediterranean area with the RDF system developed by the radio emissions project. International Journal of Engineering Science Invention (IJESI). 8(03), 26-35.

[8] Straser, V., Cataldi, D., Cataldi, G., 2019. Radio Direction Finding (RDF)-Geomagnetic monitoring study of the Himalaya Area in search of pre-seismic electromagnetic signals. Asian Review of Environmental and Earth Sciences. 6(1), 16-27.

[9] Milne, J., 1890. Earthquakes in connection with electric and magnetic phenomena. Transactions of the Seismological Society of Japan. 15, 135-162.

[10] Straser, V., Giuliani, G.G., Cataldi, D., et al., 2020. Multi-parametric investigation of pre-seismic origin phenomena through the use of RDF technology (Radio Direction Finding) and the monitoring of Radon gas stream (RN222). An International Journal for New Concepts in Geoplasma Tectonics. 8(1), 11-27.

[11] Anders, M.H., Laubach, S.E., Scholz, C.H., 2014. Microfractures: A review. Journal of Structural Geology. 69, 377-394.

[12] Brace, W.F., Paulding Jr, B.W., Scholz, C.H., 1966. Dilatancy in the fracture of crystalline rocks. Journal of Geophysical Research. 71(16), 3939-3953.

[13] Scholz, C.H., 2002. The mechanics of earthquakes and faulting. Cambridge University Press: Cambridge. pp. 471.

[14] Power, W.L., Tullis, T.E., Brown, S.R., et al., 1987. Roughness of natural fault surfaces. Geophysical Research Letters. 14(1), 29-32.

[15] Chester, F.M., Chester, J.S., 2000. Stress and deformation along wavy frictional faults. Journal of Geophysical Research: Solid Earth. 105(B10), 23421-23430.

[16] Wilson, J.E., Chester, J.S., Chester, F.M., 2003. Microfracture analysis of fault growth and wear processes, Punchbowl Fault, San Andreas system, California. Journal of Structural Geology. 25(11), 1855-1873.

[17] Faulkner, D.R., Mitchell, T.M., Jensen, E., et al., 2011. Scaling of fault damage zones with displacement and the implications for fault growth processes. Journal of Geophysical Research: Solid Earth. 116(B5).

[18] Wang, J.H., 2020. Piezoelectricity as a mechanism on generation of electromagnetic precursors before earthquakes. Geophysical Journal

International. 224(1), 682-700.
DOI: https://doi.org/10.1093/gji/ggaa429

[19] Sgrigna, V., Buzzi, A., Conti, L., et al., 2007. Seismo-induced effects in the near-earth space: Combined ground and space investigations as a contribution to earthquake prediction. Tectonophysics. 431(1-4), 153-171.

[20] Lay, T., Wallace, T.C., 1995. Modern global seismology. Academic Press: Cambridge. pp. 521.

[21] Pulinets, S., Boyarchuk, K., 2005. Ionospheric precursors of earthquakes. Springer: Berlin.
DOI: https://doi.org/10.1007/b137616

[22] Moldovan, I.A., Moldovan, A., Biagi, P.F., et al., 2012. The INFREP European Vlf/Lf Radio monitoring network—Present status and preliminary results of the Romanian Motinoring System. Romanian Reports in Physics. 64(1), 263-274.

[23] Cataldi, G., 2020. Precursori Sismici – Monitoraggio Elettromagnetico. Kindle-Amazon.

[24] Cataldi, G., 2021. Radio Emissions Project – A new approach to seismic prediction. Kindle-Amazon.

[25] Cataldi, D., Cataldi, G., Straser, V., 2019. Radio Direction Finding (RDF)-Pre-seismic signals recorded before the earthquake in central Italy on 1/1/2019 west of Collelongo (AQ). Geophysical Research Abstracts. (21), 1-1.

[26] Neishtadt, N.M., Eppelbaum, L.V., Levitski, A.G., 2006. Application of piezoelectric and seismoelectrokinetic phenomena in exploration geophysics: Review of Russian and Israeli experiences. Geophysics. 71(2), B41-B53.

[27] Irinyemi, S.A., Lombardi, D., Ahmad, S.M., 2022. Seismic hazard assessment for Guinea, West Africa. Scientific Reports. 12(1), 1-12.
DOI: https://doi.org/10.1038/s41598-022-06222-7

[28] Sierra Leone's pliability to crisis and disaster: A shock resistance model [Internet]. SSRN Electronic Journal. Available from: https://ssrn.com/abstract=3864467

[29] Meghraoui, M., IGCP-601 Working Group. 2016. The seismotectonic map of Africa. Episodes Journal of International Geoscience. 39(1), 9-18.

[30] Abouchami, W., Boher, M., Michard, A., et al., 1990. A major 2.1 Ga event of mafic magmatism in West Africa: an early stage of crustal accretion. Journal of Geophysical Research: Solid Earth. 95(B11), 17605-17629.

[31] Black, R., Caby, R., Moussine-Pouchkine, A., et al., 1979. Evidence for late Precambrian plate tectonics in West Africa. Nature. 278(5701), 223-227.

[32] Caby, R., Andreopoulos-Renaud, U., Pin, C., 1989. Late Proterozoic arc—continent and continent—continent collision in the Pan-African Trans-Saharan Belt of Mali. Canadian Journal of Earth Sciences. 26(6), 1136-1146.

[33] Bergman, E.A., Solomon, S.C., 1990. Earthquake swarms on the Mid-Atlantic Ridge: Products of magmatism or extensional tectonics?. Journal of Geophysical Research: Solid Earth. 95(B4), 4943-4965.
DOI: https://doi.org/10.1029/JB095iB04p04943

[34] Wang, Z., Singh, S.C., 2022. Seismic evidence for uniform crustal accretion along slow-spreading ridges in the equatorial Atlantic Ocean. Nature Communications. 13(1), 7809.
DOI: https://doi.org/10.1038/s41467-022-35459-z

[35] Teza, E., Scordilis, E.M., Papazachos, C.B., et al., 2016. An earthquake catalog of mid-Atlantic Ridge. Bulletin of the Geological Society of Greece. 50(3), 1258-1269.

[36] Craig, T.J., Jackson, J.A., Priestley, K., et al., 2011. Earthquake distribution patterns in Africa: Their relationship to variations in lithospheric and geological structure, and their rheological implications. Geophysical Journal International. 185(1), 403-434.
DOI: https://doi.org/10.1111/j.1365-246X.2011.04950.x

[37] Francis, T.J.G., Porter, I.T., 1971. A statistical study of Mid-Atlantic Ridge earthquakes. Geophysical Journal International. 24(1), 31-50.

[38] Murty, T.S., Nirupama, N., Nistor, I., et al., 2005. Why the Atlantic generally cannot gener-

ate transoceanic tsunamis. SET Journal of Earthquake Technology, Technical Note. 42(4), 227-236.

[39] Alaneme, K.K., Okotete, E.A., 2018. Critical evaluation of seismic activities in Africa and curtailment policies–a review. Geoenvironmental Disasters. 5, 1-17.
DOI: https://doi.org/10.1186/s40677-018-0116-2

[40] Socioeconomic Data and Applications Center (SEDAC)—A Data Center in NASA0s Earth Observing System Data and Information System (EOSDIS)—Hosted by CIESIN at Columbia University [Internet]. Available from: https://sedac.ciesin.columbia.edu/data/set/gpw-v3-population-density/maps/2?facets=region:africa

[41] Straser, V., Cataldi, G., Cataldi, D., 2015. Radio-anomalies: Tool for earthquakes and tsunami forecasts. EGU General Assembly Conference Abstracts. 17, 2508.

[42] Straser, V., Cataldi, D., Cataldi, G., 2018. Radio direction finding system, a new perspective for global crust diagnosis. New Concepts in Global Tectonics Journal. 6(2), 203-211.

[43] Rabeh, T., Cataldi, D., Adibin, Z.Z., et al., 2020. International study Italy-Malaysia pre-seismic signals recorded by RDF—Radio Direction Finding monitoring network, before earthquakes: Mw 6.3, occurred at 111 km SW of Puerto Madero in Mexico and Mw 6.3, occurred at 267 km NW of Ozernovskiy in Russia, November 20, 2019. New Concept in Geoplasma Tectonics. 8(2), 105-118.

[44] Cataldi, D., Straser, V., Cataldi, G., 2021. Crustal relaxing—a new seismogenesis phenomenon associated with seismic trigger on a global scale. International Journal of Social Relevance & Concern (IJSRC). 9(7), 137-163.
DOI: https://doi.org/10.26821/IJSRC.9.7.2021.9711

BILINGUAL PUBLISHING GROUP

Advances in Geological and Geotechnical Engineering Research

https://journals.bilpubgroup.com/index.php/agger

EDITORIAL

Editorial for *Advances in Geological and Geotechnical Engineering Research*: Vol. 5 Issue 2 (2023)

Amin Beiranvand Pour

Institute of Oceanography and Environment (INOS), Universiti Malaysia Terengganu (UMT), Kuala Nerus, Terengganu, 21030, Malaysia

1. Introduction

Earth scientists aid to guarantee a supply of clean water, explore for oil, gas, and coal, map the oceans, track severe weather, and discover the Earth materials we need to build our homes and roads, and the minerals and nutrients we need to farm the land. Environmental geologists help prevent and repair damage to our nation's wetlands, streams, rivers, and shorelines. Environmental geologists similarly support building new wetlands and stream channels to replace those lost to development. Healthy streams and rivers support endangered salmon and other wildlife. By studying geological issues, geologists, along with other scientists, can anticipate Earth's future and examine any changes that may need to be made. A key example of this is the study of climate change and how society needs to change to improve the earth's future. The scope of *Advances in Geological and Geotechnical Engineering Research* journal covers a variety of geology and environmental earth sciences. This journal is preparing to rivet a diversity of research and support the Earth in the imminent future. A total of 5 papers finally were revised, accepted, and published in Vol. 5, Issue 2, which are characteristically dedicated to geology and environmental earth sciences. The achievements of articles presented in this volume are summarized in the following section.

2. Summary of paper presented in Vol. 5, Issue 2 (2023)

Olusola A. OlaOlorun et al. [1] investigated the petrology and geochemical characteristics of crystalline basement rocks in Ora-Ekiti, Southwestern

*CORRESPONDING AUTHOR:
Amin Beiranvand Pour, Institute of Oceanography and Environment (INOS), Universiti Malaysia Terengganu (UMT), Kuala Nerus, Terengganu, 21030, Malaysia; Email: beiranvand.amin80@gmail.com

ARTICLE INFO
Received: 28 April 2023 | Accepted: 12 May 2023 | Published Online: 15 May 2023
DOI: https://doi.org/10.30564/agger.v5i2.5688

CITATION
Pour, A.B., 2023. Editorial for Advances in Geological and Geotechnical Engineering Research: Vol. 5 Issue 2 (2023). Advances in Geological and Geotechnical Engineering Research. 5(2): 76-78. DOI: https://doi.org/10.30564/agger.v5i2.5688

Nigeria. Results of the investigation show that the study area is underlain by migmatite, banded gneiss, granite gneiss and biotite gneiss. Migmatite occupies western and northern parts, banded gneiss underlies Ora-Ekiti town and extends towards the northeast. Granite gneiss underlies the eastern and southwestern corners of the area while biotite gneiss occurs towards the south. Petrographic study shows the rocks are mainly dominated by quartz, plagioclase, biotite and opaque each contributing slightly varying percentages to the modal composition. The rocks have high alumina content with pronounced enrichment in Ba, Sr and Rb. The rocks are dominantly peralkaline in nature. The rocks experienced either crystal fractionation before metamorphic remobilization or partial melting in the precursor rocks. The chemical composition of the rocks depicts them are metaluminous granitoids of calc-alkaline affinity. The rocks consist of gneisses of no economic minerals, but the petrology reveals them as common rocks typical of metamorphic terrains and geochemical features of the rocks reveal they are felsic and of granitic composition.

U. Stanley Eze et al. [2] applied 2-D and 3-D Geo-Electrical Resistivity Tomography and Geotechnical soil *e*valuation for *e*ngineering site investigation in Okerenkoko Primary School, Warri-Southwest, Delta State, Nigeria. In this study, an integrated methodology employed DC resistivity tomography involving 2-D and 3-D techniques and geotechnical-soil analysis was used to evaluate subsoil conditions for engineering site investigation to adduce the phenomena responsible for the visible cracks/structural failure observed in the buildings. The results obtained brought to light the geological structure beneath the subsurface, which consists of four geoelectric layers identified as topsoil, dry/lithified upper sandy layer, wet sand (water-saturated) and peat/clay/sandy clayey soil (highly water-saturated). The results obtained brought to light the geological structure beneath the subsurface, which consists of four geoelectric layers identified as topsoil, dry/lithified upper sandy layer, wet sand (water-saturated) and peat/clay/sandy clayey soil (highly water-saturated). The deeply-seated peat/clay materials were delineated in the study area to the depths of 17.1 m and 19.8 m from 2-D and 3-D tomography, respectively. 3-D images presented as horizontal depth slices revealed the dominance of very low resistivity materials i.e. peat/clay/sandy clay within the fourth, fifth and sixth layers at depths ranging from 8.68-12.5 m, 12.5-16.9 m and 16.9-21.9 m respectively. The dominance of mechanically unstable peat/clay/sandy clay layers beneath the subsurface, which are highly mobile in response to volumetric changes, is responsible for the noticeable cracks/failure detected on structures within the study site. These observations were validated by a geotechnical test of soil samples in the study area.

Abubakar Saidu Bako et al. [3] investigated the radon content, its related toxicity, and its risk to human health in the groundwater of the Keana in Nasarawa, Nigeria. Several borehole and well samples were collected. The results showed that the average radon concentration in water samples from Keana was 2.25 Bq/L. The radon concentration is less than the benchmark of 11.1 Bq/L established in 1991 by the Nigerian Standard Organization and the US Environmental Protection Agency. Accordingly, this study designates that the level of radon is safe and people can continue farming and other activities. To reduce the risk of cancer, however, more research could be done in the area. The future investigation could be executed during the dry and wet seasons because radon concentrations in groundwater alter over time due to dilution by recharge from rainfall.

Valentino Straser et al. [4] proposed the Radio Direction Finding method for the detection of electromagnetic signals, in the VLF band, to anticipate the occurrence of potentially destructive geophysical events such tsunami. The area of investigation is Sierra Leone, whose coastline is subjected to tidal wave hazards triggered by earthquakes generated in the Mid-Atlantic Ridge. Although Sierra Leone is not affected by recurrent earthquakes, there is nevertheless a low probability, estimated at 2 percent, of the occurrence of destructive earthquakes in the next 50 years. The Radio Direction Finding experiment

has revealed a close relationship between increased radio-anomalies, in the frequencies of 6,000 Hz, a time window between electromagnetic anomaly detection and the imminence of an earthquake, and higher frequency times for the risk of earthquake occurrence in the Mid-Atlantic Ridge.

Danusa Mayara de Souza et al. [5] correlated the sedimentary strata imaged by the ground penetration radar (GPR) method through numerical modeling with the mapping of sedimentary strata acquired through geotechnical surveys in Reduto Case Study, Belém-PA, Brazil. Additionally, the study exposed how obtaining subsoil information through noninvasive/destructive electromagnetic waves is beneficial, as they are reliable and less costly than drilling holes. Subsequently, physical-geological modeling was applied. The information on the type of sediments is attained using simple recognition surveys executed in the city of Belém-PA, which is facilitated to create of a model of a sedimentary package with its respective intrinsic physical properties. The result demonstrates that the GPR recovered with good vertical and horizontal resolution at the beginning and end of the layers of the sedimentary units. The technique proved to be very effective for locating geotechnical sounding points and reducing costs.

3. Concluding remarks

The considerate and thoughtful comments conveyed by the reviewers enriched each of the papers published in this volume. We would like to express our appreciation to the Editorial Office, all authors and reviewers who contributed their time, research, and specialty for this volume. We hope to receive a variety of manuscripts from different fields in the coming future.

Conflict of Interest

There is no conflict of interest.

References

[1] OlaOlorun, O.A., Akinola, O.O., Oyinloye, A.O., 2023. Petrology and geochemical features of crystalline rocks in Ora-Ekiti, Southwestern Nigeria. Advances in Geological and Geotechnical Engineering Research. 5(2), 24-37.
DOI: https://doi.org/10.30564/agger.v5i2.5243

[2] Eze, S.U., Okiotor, M.E., Ighodalo, J.E., et al., 2023. Application of 2-D and 3-D geo-electrical resistivity tomography and geotechnical soil evaluation for engineering site investigation: A case study of Okerenkoko Primary School, Warri-Southwest, Delta State, Nigeria. Advances in Geological and Geotechnical Engineering Research. 5(2), 1-23.
DOI: https://doi.org/10.30564/agger.v5i2.5382

[3] Bako, A.S., Rilwan, U., Umar, I., et al., 2023. Toxicity of radon-222 in groundwater across Keana in Nasarawa, Nigeria. Advances in Geological and Geotechnical Engineering Research. 5(2), 38-49.
DOI: https://doi.org/10.30564/agger.v5i2.5632

[4] Straser, V., Cataldi, D., Cataldi, G., 2023. Radio direction finding method to mitigate tsunami risk in Sierra Leone. Advances in Geological and Geotechnical Engineering Research. 5(2), 64-75.
DOI: https://doi.org/10.30564/agger.v5i2.5617

[5] Mayara de Souza, D., Clávio de Alcântara Júnior, L.L.L., 2023. Correlation of ground penetrating radar data with geotechnical prospect profiles: Reduto case study, Belém-PA, Brazil. Advances in Geological and Geotechnical Engineering Research. 5(2), 50-63.
DOI: https://doi.org/10.30564/agger.v5i2.5579

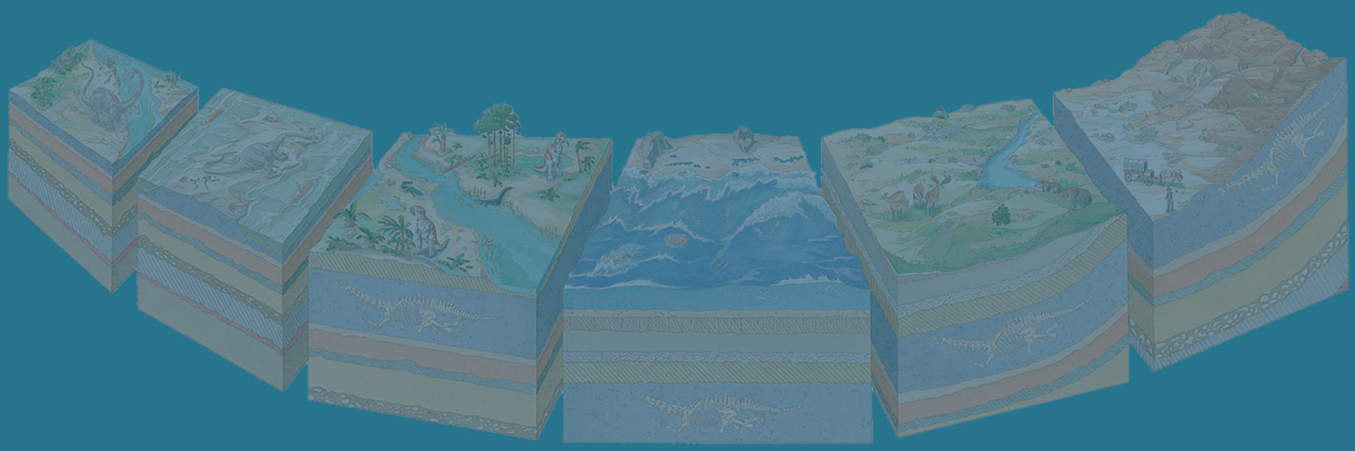

BILINGUAL PUBLISHING GROUP
Tel:+65 65881289
E-mail: contact@bilpublishing.com
Website:https://journals.bilpubgroup.com

2810-9384 02
9 772810 938231